Conformational Influence
on Quantum Transport
in Nanostructures

Zur Erlangung des akademischen Grades eines

DOKTORS DER NATURWISSENSCHAFTEN

von der Fakultät für Physik des
Karlsruher Institut für Technologie (KIT)

genehmigte

DISSERTATION

von

Dipl.-Phys. Robert Maul
aus Jena

Deutsche Zusammenfassung

Der elektronische Transport in nanoskaligen Strukturen wurde in den letzten zehn Jahren intensiv untersucht. Hierbei hat die Herstellung von Nanokontakten durch STM (scanning tunneling microscope), Bruchkontakten oder durch die elektrochemische Abscheidung zu neuen Einblicken in die Physik des Ladungstransports in Quantensystemen sowie zur Entwicklung vielversprechender Ansätze nanoelektronischer Bauelemente geführt. Eine wesentliche Herausforderung bei den Messungen der molekularen Elektronik besteht in der Kontrolle der Geometrie des Kontaktes und der Kopplung an mindestens zwei ebenfalls nanoskalige Elektroden. Da jedoch die genaue Molekülgeometrie im Experiment nicht kontrollierbar ist, hat auch die strukturelle Variabilität einen wesentlichen Einfluss auf die beobachteten Eigenschaften. Somit muss in theoretischen Beschreibungen des elektronischen Transports durch Nanostrukturen die strukturelle Variabilität mit effizienten Methoden berücksichtigt werden und in die quantenchemischen Berechnungen der elektronischen Eigenschaften einfließen.

In der vorliegenden Arbeit wurde das Zusammenspiel von Konformation und elektronischen Transporteigenschaften in metallischen und organischen Nanostrukturen untersucht. Die Charakterisierung von thermischen, elektrostatischen und durch Syntheseprozess induzierten strukturellen Einflüssen auf den Leitwert liefert ein tieferes physikalisches Verständnis des Ladungstransports in Nanostrukturen wie nicht-idealisierte Quantenpunktkontakte, Nanodrähte und Nanopartikel. Zusätzlich können dadurch zukünftige nanoelektronische Bauelement, wie z.B. schaltbare Moleküle, für Anwendungen gefunden und unter Berücksichtigung von Umgebungseinflüssen optimiert werden.

Um realistische Konformationen von Nanostrukturen zu simulieren, die experimentell durch elektrochemische Abscheidung entstehen, wurde ein effizientes Verfahren zur Simulation des Strukturaufbaus entwickelt und implementiert, das auf klassischen Wechselwirkungen basiert und Strukturen sowohl von metallischen Systemen als auch von ausgedehnten organischen Molekülen simulieren kann. Im Gegensatz zu molekulardynamischen Simulationen (MD) ist es mit dem hier verwendeten stochastischen Ansatz möglich, Wachstumsprozesse zu simulieren, die auf sehr langen Zeitskalen (Sekundenbereich) stattfinden. Um die elektrochemischen Transporteigenschaften der resultierenden ausgedehnten Nanostrukturen berechnen zu können, wurde darüber hinaus eine quantenmechanische Methode, basierend auf rekursiven Greenschen Funktionen (RGF) und Model-Hamilton-Operatoren, implementiert. Der Rechenaufwand dieser Methode skaliert lediglich linear mit der Länge des untersuchten Systems, so dass Moleküle mit einer großen Anzahl von Atomen und ausgedehnte Elektrodenfragmente in die Berechnung einbezogen werden können. Die entwickelten *Methoden* wurden auf die folgenden *Systeme und Fragestellungen* angewendet:

Statische Unordnung in Metallkontakten:

Als erstes wurde der ballistische Elektronentransport in ideal kristallinen Silbernano-
kontakten mit Hilfe der RGF-Methode untersucht. Bei Abwesenheit von Defekten
und Unordnung und im Grenzfall kleiner Kontaktquerschnittsflächen (wenige Atom-
durchmesser) ist der Leitwert ein ganzzahliges Vielfaches des Leitwertquants G_0, was
in erster Linie auf die chemische s-Konfiguration des Metalls zurückzuführen ist. Die
Untersuchungen werden anschließend durch Variation verschiedener geometrischer
Parameter auf ungeordnete Strukturen verallgemeinert und so der experimentellen
Situation einer nicht-idealisierten Nanostruktur angenähert: Ausgehend von einer
symmetrischen Anordnung der Silber-Punktkontakte ergibt sich für eine Verkippung
der Elektroden bis zu 60 Grad ein um 20% niedrigerer Leitwert, während gezeigt
werden konnte, dass eine Verdrehung (Torsion) der Elektroden nahezu keinen Einfluss
auf den Leitwert hat. Des weiteren wurde die Abschwächung der Leitfähigkeit her-
vorgerufen durch Oberflächenvakanzen statistisch untersucht und eine Verringerung der
Leitfähigkeit von bis zu 30% gefunden. Nicht nur eine Abweichung vom fcc-Kristall,
sondern eine qualitativ andere Atomanordnung tritt in metallischen Nanoclustern auf.
Während auch hier der Leitwert wesentlich von der minimalen Querschnittsfläche des
Systems abhängt wird die Fluktuationsstärke der Transmissionsfunktion vom Gesamt-
durchmesser des Nanoclusters bestimmt. Somit könnte man mit der Bestimmung der
Transmissionsfunktion in einer Drei-Punktmessung und deren Vergleich mit den hier
berechneten Resultaten auf Clusterdurchmesser und Atomstruktur schließen.

Atomarer Transistor:

Als zweite Anwendung der implementierten Methoden wurden mechanische, elektro-
statische und elektronische Eigenschaften von sogenannten Einzelatomtransistoren
untersucht. Beim Experiment zum Einzelatomtransistor werden Silber-Nanokontakte
elektrochemisch hergestellt und „trainiert", so dass der Leitwert der so erzeugten
Nanostruktur zwischen ganzzahligen Vielfachen des Leitwertquants schaltbar ist. Für
die theoretische Beschreibung dieses Systems wurde eine Multiskalenmethode entwick-
elt, die ein Kontinuum-Modell des Lösungsmittels, ein atomistisches (auf klassischen
Kraftfeldern basierend) und ein quantenmechanisches Modell miteinander kombiniert.
Dies ist nötig, da in den hier untersuchten Nanokontakten physikalische Prozessen auf
verschiedenen Zeit- und Längenskalen zusammenwirken. Mit dieser Methode konnte
der zu Grunde liegende Schaltmechanismus der atomaren Transistorkonformationen auf
die bistabile Spitzenrekonstruktion der Silberkontakte zurückgeführt, und das Schalten
zwischen immer wiederkehrenden Leitwertniveaus erklärt werden. Diese Niveaus werden
durch bestimmte, materialabhängige Kontaktkonformationen von besonders hoher
Bistabilität erreicht, analog zur hohen Stabilität von Metallclustern bei sogenannten
„magischen" Atomzahlen [1]. Speziell im Fall von Silber liegen diese Leitwertlevels
bei ganzzahligen Vielfachen des Leitwertquants G_0. Die Modellrechnungen bestätigen
ebenfalls die experimentelle Beobachtung, dass beim Schalten einer (Silber-) Kontakt-
geometrie mit nicht ganzzahliger Leitfähigkeit stets ein „Einrasten" in eine Struktur mit
ganzzahligem Leitwert oder eine Zerstörung des Kontaktes (also $G = 0$) zu beobachten

ist. Eine wichtige Eigenschaft der Einzelatomtransistoren ist ihre stabile Schaltbarkeit bei Zimmertemperatur über eine große Anzahl von Schaltzyklen (Größenordnung 1000). Diese Beobachtung kann mit dem „Trainingseffekt" erklärt werden, der in den durchgeführten Modellrechnungen bei wiederholtem Schalten des Nano-kontaktes sichtbar wird und zu einer Verbesserung der Bistabilität mit jedem Schaltzyklus führt. Des weiteren wurde in der vorliegenden Arbeit die Wirkung der dielektrischen Doppelschicht, welche durch den umgebenden Elektrolyten hervorgerufen wird, untersucht und ein zusätzlich stabilisierender Einfluß der elektrochemischen Umgebung auf den Schaltvorgang nachgewiesen. Außerdem konnte auch der Mechanismus des Schaltens zwischen Levels mit endlichem ganzzahligem Leitwert erklärt werden: Das Auftreten von metastabilen Konformationen bei ganzzahligem Leitwert erzeugt beim Auseinanderziehen der Kontakte Plateaus in der Leitwertkurve. Diese Plateaus können beim Inter-Level-Schalten wiederum angesteuert werden. Schwache Leitwertfluktuationen zu nichtganzzahligen Leitwerten können durch das verwendete multi-skalige Modell auf thermisch induzierte Hüpfprozesse von einzelnen Atomen zurückgeführt werden.

Strukturelle Unordnung in molekularen Drähten:

Im dritten Teil dieser Arbeit wird die Methode der rekursiven Greenschen Funktionen in Kombination mit Molekulardynamik und Dichtefunktional-Theorie (DFT) zur Untersuchung von organischen Nanodrähten angewendet. Die Transmissionsfunktion und der längenabhängige Leitwert von Molekülketten konnte in guter Übereinstimmung mit Ergebnissen genauerer (und deutlich aufwendigerer) quantenchemischer Methoden bestimmt werden. Dieses Resultat ist nicht selbstverständlich, da bei dem hier verwendeten Ansatz der zentrale Streubereich in Schichten mit Nächster-Nachbar-Kopplung zerlegt wird (oder mathematisch ausgedrückt, die Hamilton-Matrix wird beschnitten), so dass sich der Rechenaufwand deutlich reduziert. Die somit validierte Methode wurde nun eingesetzt, um den Einfluss thermisch induzierter Strukturfluktuationen auf die Leitfähigkeit molekularer Drähte, zunächst Oligo-Phenylen, zu untersuchen. Die Trajektorie der Molekülgeometrie wurde dabei mit klassischer Molekulardynamik berechnet und an das beschriebene Elektronentransportmodell gekoppelt, mit dem in jedem Zeitschritt der Leitwert berechnet wird. Die Simulation zeigt temporäre Leitwertfluktuationen um eine Größenordnung (in Einheiten von G_0) und das Auftreten von Molekülkonformationen deutlich erhöhter Leitfähigkeit, die allerdings bei $T = 0$ durch sterische Abstoßung von Molekülgruppen unterdrückt werden. Der mittlere Leitwert dieser Konformationen erklärt den experimentell beobachteten Wert sehr gut, da in nahezu allen Messanordnungen für den Transport durch Einzelmoleküle die Strukturfluktuationen des kontaktierten Systems einen starken Einfluss haben. Motiviert durch intensive experimentelle Untersuchungen organischer Nanodrähte und der zahlreichen offenen Fragen auf diesem Gebiet, wurde anschließend die Korrelation von Struktur, elektronischen Eigenschaften und des Ladungstransports in Oligo-Phenyleimine-Molekülen analysiert. Mit Hilfe von Dichtefunktional-Theorie wurden die verschiedenen energetischen Barrieren, die bei der Torsion der Ringeinheiten des molekularen Drahtes auftreten, berechnet. Es zeigt sich, dass die Energie, die für eine vollständige Torsion zweier Ringeinheiten benötigt wird stets niedriger als 16 meV ist, woraus folgt, dass bereits bei Zimmertemperatur

derartige Konformation energetisch erlaubt sind und somit die Konjugationslänge der Moleküle reduziert wird. Des weiteren zeigen die quantenchemischen Berechnungen, dass die Ausdehnung der Molekülorbitale, die hauptsächlich zum Ladungstransport beitragen, auf drei bis vier Ringeinheiten beschränkt ist. Dies erklärt insbesondere auch die experimentell beobachtete Änderung in der Längenabhängigkeit des elektrischen Widerstandes beim Übergang von kürzeren (1-4 Ringeinheiten) zu längeren (5-10 Ringeinheiten) molekularen Drähten. Der berechnete Dämpfungsparameter, der die Längenabhängigkeit des Leitwertes im Fall kurzer Molekülketten charakterisiert, konnte in guter Übereinstimmung mit dem experimentellen Wert zu $\beta = 3.29$ nm^{-1} ermittelt werden. Wegen dem Zusammenhang von Molekülgeomtrie und Leitwert, bestätigt dies insbesondere die mit DFT bestimmten Gleichgewichtstorsionswinkel der Molekülkette.

Wachstumsprozess von Palladium-Nanopartikeln in Proteintemplates:

Der letzte Teil dieser Arbeit beschreibt die theoretische Untersuchung von hybridartigen Protein-Palladium-Nanopartikeln, welche vielversprechende Anwendungsmöglichkeiten, sowohl in neuartigen, auf Nanotechnologie basierenden Speichern als auch in der Krebstherapie, besitzen. Nachdem die experimentelle Herstellung von Palladium-Nano-partikeln unter Verwendung von Proteintemplates gelang, ergaben sich zahlreiche Fragen zum Ablauf der Strukturbildung, deren Klärung für die weitere Verwendbarkeit der Nanopartikel von großer Bedeutung ist. In Hinblick auf zukünftige Anwendungen ist es wichtig herauszufinden, ob das Nanopartikel, hervorgerufen durch die Gegenwart des Proteins, als poröse Struktur wächst, sich eventuell im äußeren Ringbereich des Proteins bildet oder zu einem kompakten Cluster wächst. Des weiteren ist auch der strukturelle Einfluss des Metallclusters auf das Protein von großer Bedeutung, da dieser über die anschließende Anwendbarkeit des Hybridsystems entscheidet. Mit der Kombination von Molekulardynamik und Monte-Carlo-Simulationen wurde die Proteinstruktur vor und nach der Deposition der Palladiumionen berechnet. Die MD-Simulation der Proteinstruktur unter expliziter Berücksichtigung der Wassermoleküle der Lösung (insgesamt ca. 100.000 Atome) lieferte ein ringförmiges Makromolekül mit einem äußeren Durchmesser von 10 nm aufgebaut aus zahlreichen helikalen Molekülketten. Die Abscheidesimulation der Palladiumionen zeigt, dass das Nanopartikel als kompakter polykristalliener Metallcluster wächst und über die Histidin-Endgruppen an das Protein bindet. Darauf aufbauend ermöglichen weitere Simulationen die Interpretation der gemessenen Circulardichroismus-Spektren und es zeigt sich, dass auch nach dem Metall-clusterwachstum die Proteinstruktur intakt bleibt und somit zusätzlich funktionalisiert werden und in biologischen Organismen oder neuartigen Speichern eingesetzt werden kann.

In der vorliegenden Arbeit wurde gezeigt, dass strukturelle Eigenschaften einen wesentlichen Einfluss auf den kohärenten Elektronentransport in nanoskaligen Syste-men haben. Um Messungen des elektronischen Transports zu erklären und funktional-isierte Nanostrukturen zu optimieren erweist es sich in Modellrechnungen als unerlässlich, eine hinreichend große Region des zentralen Streubereiches und eine nicht-idealisierte (Molekül-)Konformation zu berücksichtigen. Untersucht wurde der Einfluss struktureller

Unordnung, welche in realen Systemen stets vorhanden ist und die elektronischen Transporteigenschaften dominieren kann. Dabei liefert das hier entwickelte multi-skalige Model eine leistungsfähige Methode, um die auftretenden physikalischen Effekte, die sich auf verschiedenen Zeit und Längenskalen abspielen, mit vertretbarem Rechenaufwand zu kombinieren. Somit besitzt die implementierte Methode großes Anwendungspotential auf zahlreiche weitere Fragestellungen der Nanophysik.

Contents

1 Introduction

1.1 Motivation and overview

The invention of the computer has affected all areas of our life's at work as well as private life. The key device permitting a computers functionality is the central processing unit (CPU). When the first CPU's were built up from three terminal devices based on vacuum tubes computation machines needed a large amount of space and had very limited applicability only usable by highly specialized computer scientists. A revolutionary development, the semiconductor transistor, enabled a tremendous miniaturization scaling from „bus-sized" computers to current PC's with an intuitive user interface. However, even metal-oxide transistor based CPU's, fabricated by lithography, have technical limitations regarding device density and speed. If Moore's „law" [2] is correct this physical limit is reached in the next 10 years, which means that a completely new technology will be required to continue this trend, calling for a jump similar to that from vacuum tubes to semi-conductor transistors.

Promising ideas for such a new technology are developed in the field of *nano-electronics*, where electronic devices comprised of individual molecules or metallic nano-wires and clusters have been proposed [3]. Nanoelectronics has the potential to play an enormous role in enhancing a range of products, including sensors, photovoltaics and consumer electronics. In this interdisciplinary research computer-scientists and physicists have to deal with five key issues [4]: basic understanding of the transport mechanisms; scalability to near molecular dimensions; tolerance of manufacturing defects; introduction of non-traditional fabrication methods, such as chemically directed assembly; bridging between device densities potentially achievable at the molecular scale and those associated with standard lithography; and fabrication simplicity.

One of the most promising nano-scale circuits that have been investigated is the cross-bar, shown in Fig. 1.1a, which is formed from orthogonal nano-wires having individual molecular or molecular-scale devices sandwiched within the junctions. This approach permits intrinsic versatility and is tolerant of manufacturing defects [5], thus both mem-ory and logic circuits have been demonstrated from molecular electronics and nano-wire crossbars [6, 7].
For the central molecular-scale bridge (see Fig. 1.1b) of the crossed nano-wires various molecular switches and molecular transistors have been proposed in past 20 years, but a comprehensive theoretical description that accounts for their electronic structure in a realistic structural assembly remains difficult. To date it has remained a big challenge to engineer orientation and placement of the building blocks into the desired
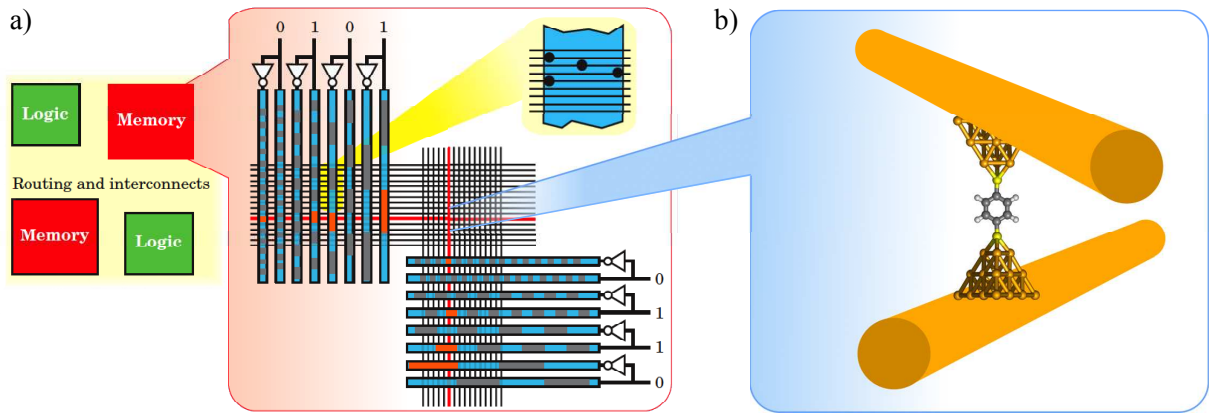
Figure 1.1: *Crossbar architecture of a nanoelectronics molecular memory for novel future integrated circuits permitting orders of magnitude higher storage density. The left part of the schematic illustrates the crossbar architecture of nano-wires in combination with demultiplexers bridging the micron length scale of lithography to nanometer length scale of molecular electronics. The right part shows the operating molecule (as memory or diode) in between the crossed nano-wires (The left part of this figure was taken from Ref. [4]).*

device architecture in reproducible high yields and at low costs. Recently a pioneer in nanoelectronics, James R. Heath, claimed that at least three experimental items have to be improved: „Robustness, robustness and robustness" [8].

In a conventional semiconductor or metal wire the charge transport is ohmic. The use of nano-scale device systems is based on fundamentally new physics, which deviates completely from what is observed in traditional conductors. The simplest molecular wire structure comprises a molecule bonded through a single atom to electrodes at the two molecular termini. Depending on the strength of the electrode coupling we distinguish between two different transport mechanisms. If the electronic wavelength becomes comparable to the size of the junction, novel quantization effects become important:

In the case of strong electrode-molecule coupling, preferably created by a covalent bond between electrode and molecule, the electrons move through such a structure by *elastic scattering*. In this limit „conductance is scattering", as was stressed by Rolf Landauer [4]. For such systems the total conductance is given as a sum over individual transmission channels, that arise from the orbitals of the scattering molecule. One channel carries a maximal conductance quantum $G_0 = 2e^2/h = 12.8$ kΩ^{-1} (e is the electron charge, h is Planck's constant). The relative transmission of each channel, which varies between zero and unity, is a complicated function depending on the energy of the incoming electrons, the electrode's density of states and the molecular orbitals. Its value in such a complex scatterer is significantly affected by structural disorder and thermally induced fluctuations of the conformation.

If the molecule is weakly bonded to the electrodes, the electrons are not able to flow from the left electrode to the right coherently, because the energetic barriers of the contacts are too high. Induced by either thermal or electrical excitation the electrons can only jump diffusively from the one electrode onto the molecule and to the other

electrode. This *hopping mechanism* proceeds on a longer time scale than the previously described elastic scattering process, thus the electrons spend more time on the molecule, similar to charging a capacitor. Therefore electron-electron and electron-phonon effects play an important role in this regime. This transport mechanism can be described using Marcus-theory developed by Rudolph A. Marcus who was awarded the Nobel Price in 1992 for this work.

Extending previous theoretical studies of charge transport in nanostructures, which considered idealised electrode/molecule configurations at zero Kelvin surrounded by vacuum [9–11] in the present work we will study the correlation between structural variety and conductance properties of different molecular or nano-scale systems of high relevance for applications in future nanoelectronic devices. Using a multi-scale model, which includes environmental effects, we will focus on the conductance switching mechanisms on the nanometer scale under the influence of a surrounding thermal bath and ionic solvent.

1.2 Outline

This thesis is organized as follows: We first give a brief introduction to the variety of the underlying methodological concepts required for the specific investigations presented in this work. Modeling the interplay of morphologies at the atomic level with the electronic structure is a central issue of the present work. Therefore, we begin with a short description of the basic ideas of the simulation techniques describing structural changes, such as the molecular dynamics and the Monte-Carlo method. Both methods are based on classical force fields and thus permit simulation of systems containing a high number of atoms, but cannot describe quantum effects. Next we describe how we couple such methods to the quantum mechanical level using tight-binding like model Hamiltonians and density functional theory. On the basis of these descriptions of atomistic morphology and electronic structure calculations we turn to the study of electronic charge transport in the coherent limit. We briefly recapitulate the Landauer-Büttiker scattering formalism [12] and the related concept of treating the semi-infinite electrodes via self-energies [13]. In the investigations presented in the following we need to treat extended nano-junctions, containing a large number of atoms, which change their conformation. Treatment of dynamic processes on the quantum mechanics level requires an very efficient approach to calculate the conductance. In the final section of this chapter we derive the recursive Green's function formalism, which allows treatment of extended nano-junctions during dynamic processes at the quantum level.

In the third chapter we apply these methods to calculate the coherent conductance of crystalline silver nano-junctions and examine the dependence of the conductance on the minimal cross-section. We systematically vary the geometry of the nano-junction to reflect more complex and more realistic situations by briefly introducing different kinds of disorder. We investigate the influence of structural displacement and the occurrence of vacancies, which has been neglected in most previous theoretical studies, but is always present in experiments. Furthermore we investigate the transmission functions

of silver nano-clusters of varying size in a scanning tunneling microscope setup and propose an approach to determine the cluster's diameter and conformation from the transmission function. Our results demonstrate the accuracy of the recursive Green's function formalism and give first insights into the influence of different types of disorder on the electronic transport.

In chapter four we investigate a promising experimental approach to realize an active nano-electronic building block, the atomic transistor developed by the group of Prof. Schimmel (KIT, IAP and INT), which present a challenging case study for the conformational influence on quantum transport. The experiment is based on a silver quantum point contact fabricated by electrochemical deposition and allows for bistable switching between integer levels of quantum conductance. We develop a multi-scale modelling approach for electrochemical three-terminal devices and develop a theory for the underlying switching mechanism of the atomic transistor that integrates atomistic dynamics with quantum transport effects. An important feature of the atomic transistor experiment is the tremendous stability of repeated switching between different quantized conduction states in particular at room temperature. The results of our model give new insights into the reasons for this stability. Furthermore we discuss the mechanism that permits switching between conducting states with integer quantum conductance, although the details of the levels are material specific. Measurements at high time resolution yield additional substructures when the conductance is measured as a function of time. Using our model we explain this observation and trace it back to fluctuations of single atoms in meta-stable positions. We also discuss the influence of the electrolyte on electrode deposition and switching of the device. The results of this chapter lead to better understanding of the atomic transistor experiment, but also give new insights into the physics of charge transport in non-idealized nano-junctions during conformational change.

Motivated by recent experimental investigations of charge transport mechanisms in organic wires, we present in chapter five the results of extensive investigations of oligo-phenylene and oligo-phenyleneimine molecular wires. We demonstrate that the recursive Green's function method yields the correct length dependence of the conductance and investigate the energetic torsional barriers affecting the total transmission of the nano-wire. In addition we combine a molecular dynamics simulation of the wire at room temperature and evaluate the conductance for many snapshots of the conformation. We find strong thermally induced fluctuations of the conductance, which are neglected in almost all present-day descriptions of ballistic conductance using density functional theory. We conclude the chapter with an analysis of transport through oligo-phenyleneimine molecular wires. Calculating structural, electronic and transport properties of oligo-phenyleneimines we obtain new insights into the charge transport mechanisms in organic nano-wires with respect to their strong conformational variability.

In chapter six we assist interpretation of a hybrid protein/palladium nano-particle system, with promising applications in future flash-memory devices or in cancer therapy, by a structural analysis. This study was motivated by a collaboration with the experi-

mental groups of Prof. O. Shoseyov (University of Rehovot, Isreal) and Dr. S. Behrens (KIT, ITC). Using molecular dynamics simulations we optimize the structure of the protein and evaluate its stability at room temperature in the presence and absence of the nanoparticle in the system. To explain the experiment we have developed a method for the electrochemical palladium nano-particle deposition simulation. The comparison of structural fluctuations of the protein itself and protein functionalized with the nanoparticle rationalizes the interpretation of the circular dichroism spectra and gives new insights into the fabrication of metal nano particles by protein templates.

Chapter seven summarizes this thesis and presents the main conclusions of this study.

2 Numerical methods

In the simulations of nanoscale systems one major goal of the present thesis is to take a broad variety of effects into account which result from physical processes on different time and length scales. In this section we will briefly describe the main ideas of the atomic structure simulation methods, based on classical forcefield, and quantum chemistry methods employed in this work. Special emphasis is put on the description of the coherent transport theory, Landauer-Büttiker formalism, and on the recursive Green's function method, in particular, since this algorithm was implemented here for efficient material specific transport calculations of nano-junctions containing a high number of atoms.

2.1 Atomic structure calculation

2.1.1 Molecular dynamics

Molecular dynamics (MD) simulation is a technique to compute the equilibrium and dynamic properties of a classical many-body system, meaning that the basis of the approach are Newton's equations of motion and quantum mechanical effects are not taken into account explicitly. The atom dynamics is treated within the Born-Oppenheimer approximation [14, 15], where the electrons are assumed to follow the classical nucleus instantaneously. Here the influence of the electrons is not treated explicitly, but one accounts for their average effect by analytical interaction potentials among the nuclei. Molecular dynamics simulations generate information on the microscopic level, in particular atomic positions and velocities as a function of time, which has to be translated into macroscopic observable like pressure, heat capacity, diffusion coefficient, etc. by means of statistical mechanics.

The MD method, which is today exploited in a wide range of applications in fundamental and applied science, was introduced by Alder and Wainwright in the late 1950's [16, 17] to study the interaction of hard spheres. The next major advance was in 1964, when Rahman carried out the first simulation using a realistic potential for liquid argon [18] followed by the first protein simulations which appeared in 1977 with the simulation of the bovine pancreatic trypsin inhibitor (BPTI) performed by McCammon *et al.* [19]. Today there is a broad literature of molecular dynamics simulation results ranging from atomic and solid state physics to soft matter applications [20, 21] and specialized techniques for particular problems, including mixed quantum mechanical - classical simulations, have been developed [22, 23] covering also the length- and time-scale gap of complex fluids with hybrid simulation techniques, where MD simulations are one of the components.

Newton's equations of motion are the basic dynamical equations in molecular dynamics.

Assuming a system of N point particles of mass m_i $(i = 1, ..., N)$ at positions $\mathbf{r}_i$ and velocity $\dot{\mathbf{r}}_i$ they are given by

$$m_i \frac{d^2}{dt^2} \mathbf{r}_i = \mathbf{F}_i. \tag{2.1}$$

The occurring forces $\mathbf{F}_i$ on particle i are obtained from the potential energy $U(\mathbf{r}_1, ..., \mathbf{r}_N)$ with $\mathbf{F}_i = -\nabla_{\mathbf{r}_i} U$. These equations provide a solution containing the complete information of a system for particular initial conditions, i.e. at $t = 0$, $\mathbf{r}_i(0)$ and $\dot{\mathbf{r}}_i(0)$. An alternative formulation is given by Hamiltonian equations of motion for the generalized momenta $\mathbf{p}_i$ and positions $\mathbf{r}_i$ following from the Hamiltonian

$$H = \sum_{i=1}^{N} \frac{\mathbf{p}_i^2}{2m_i} + U(\mathbf{r}_1, ..., \mathbf{r}_N) \tag{2.2}$$

leading to the canonical equations

$$\dot{\mathbf{r}}_i = \nabla_{\mathbf{p}_i} H, \quad \dot{\mathbf{p}}_i = -\nabla_{\mathbf{r}_i} H \tag{2.3}$$

$$\implies \dot{\mathbf{r}}_i = \frac{\mathbf{p}_i}{m_i}, \quad \dot{\mathbf{p}}_i = -\nabla_{\mathbf{r}_i} U(\mathbf{r}_1, ..., \mathbf{r}_N). \tag{2.4}$$

An important advantage of this approach is, that the validity of the numerical solution can be checked by certain conservation laws. I.e. in conservative systems, where the external potential is time independent, the total energy H is conserved. Moreover, the systems under consideration are invariant with respect to translation, i.e. $\sum_i m_i \ddot{\mathbf{r}}_i = 0$ and the equations of motion (2.1) are reversible in time as well and canonical, i.e. conserving phase space volume. If the equations of motion are solved correctly, the computer-generated trajectories will also exhibit these properties.

The broad spectrum of macroscopic properties of materials is tightly related to the forces among their elementary building blocks. Since their properties range from spatial structure of solids to the secondary and tertiary structure of biological supramolecular systems, it is desirable to achieve a representation of the actual interactions in terms of the classical potential energy $U(\mathbf{r}_1, ..., \mathbf{r}_N)$ as accurate as possible. The potential energy of N interacting atoms can be divided into terms depending on the coordinates of individual atoms, pairs, triplets etc.:

$$U(\mathbf{r}_1, ..., \mathbf{r}_N) = \sum_i u_1(\mathbf{r}_i) + \sum_i \sum_{j>i} u_2(\mathbf{r}_i, \mathbf{r}_i) + \sum_i \sum_{j>i} \sum_{k>j>i} u_3(\mathbf{r}_i, \mathbf{r}_j, \mathbf{r}_k) + ... \ . \tag{2.5}$$

The first term (u_1) represents the effect of an external field on the system, e.g., gravitational force, electric fields, box walls, etc.. Particle interactions are represented by the remaining terms, where the pair interaction u_2 is the most important. In many cases the computational costs to evaluate the higher order terms like u_3 are to high, thus the pair potential is chosen such that it includes triplet and higher order interactions. Typical atomic pair potentials are the Hard-sphere potential, the Coulomb potential and the

Lennard-Jones potential

$$U^{LJ}(r) = 4\epsilon \left[\left(\frac{\sigma}{r} \right)^{12} - \left(\frac{\sigma}{r} \right)^{6} \right] \tag{2.6}$$

with r denoting the distance between two atoms. The potential consists of a steep rising repulsive wall at short distances ($\sim r^{-12}$) capturing the non-bonded overlap between the electron clouds and an attractive tail at large seperations ($\sim r^{-6}$), essentially due to correlations between the electron clouds surrounding the atoms („van der Waals" or „London" dispersion).
However, to account for all aspects of chemical bonding, particularly in the case of molecules, including the reactions which form and break bonds would require a quantum mechanical description. In MD simulations for non-reacting molecules the problem is solved by accounting for the internal molecular degrees of freedom, i.e. bond length, bond bending and torsion, in terms of appropriate potential functions. A simple MD force field for a molecule reads as

$$U(\mathbf{r}_1, ..., \mathbf{r}_N) = \sum_{bonds} \frac{k_i^b}{2}(r_i - l_i)^2 + \sum_{angles} \frac{k_i^a}{2}(\theta_i - \theta_{eq,i})^2 + \sum_{torsion} \frac{k_i^t}{2}[1 + \cos(n_i \phi_i - \gamma_i)] + U^{LJ} + U^C. \tag{2.7}$$

The covalent bonds are described by the first term with the equilibrium bond length l_i. The second term accounts for restrictions in the bond angle banding due to overlapping electronic clouds of bond atoms. Similarly, the third term describes the interactions of the electronic clouds of atoms separated by three bonds (torsion potential). Further apart atoms in a molecule interact via the non-bonded Lennard-Jones and Coulomb potentials, similar to unbounded atoms. A number of algorithms have been suggested to integrate
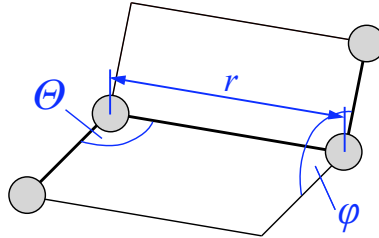
Figure 2.1: *Internal coordinates occuring in MD force files of molecular systems: atomic distance r, bond angle θ and torsion angle ϕ.*

Newton's equations of motion. Some of them are more suitable than others. A simple but very efficient algorithm, which satisfies the important conservation laws is called velocity Verlet algorithm. It can be derived by Taylor expansion of the coordinates of a particle at time t and reads as:

1. Initial conditions: positions $\{\mathbf{r}(0)\}$, velocities $\{\dot{\mathbf{r}}(0)\}$, forces $\{\mathbf{F}(0)\}$

2. Calculation of new positions according to

$$\mathbf{r}_i(t + h) = \mathbf{r}_i(0) + (t + h)\dot{\mathbf{r}}_i(0) + \frac{(t + h)^2}{2m_i}\mathbf{F}_i(0) \tag{2.8}$$

Calculation of velocities

$$\dot{\mathbf{r}}_i(t + h/2) = \dot{\mathbf{r}}_i(t) + \frac{h}{2m_i}\mathbf{F}_i(t) \tag{2.9}$$

3. Calculation of forces using positions $\mathbf{r}(t + h)$

$$\mathbf{F}_i(t + h) = \mathbf{F}_i(\{\mathbf{r}(t + h)\}) \tag{2.10}$$

4. Calculation of velocities

$$\dot{\mathbf{r}}_i(t + h) = \dot{\mathbf{r}}_i(t + h/2) + \frac{h}{2m_i}\mathbf{F}_i(t + h) \tag{2.11}$$

5. Go to the next time step $(t + 2h)$ and continue with (2.).

The simulations described so far apply to a closed system with a given number of particles N in a fixed Volume V at constant energy E. If we assume that time averages are equivalent to ensemble averages, then the averages obtained in such a simulation are equivalent to ensemble averages in the microcanonical ensemble (NVE-ensemble). However, various physical situations require simulation of other ensembles by inclusion of the environment into simulation, e.g. via special boundary conditions, thermostat implementations and solvent descriptions at different levels. For these and other technical details of molecular dynamics the reader is referred to the literature [24–30].

2.1.2 Monte Carlo methods

Monte Carlo methods (MC) tend to be used when it is unfeasible or impossible to compute an exact result with a deterministic algorithm, which happens typically if the classical or quantum mechanical problem incorporates a vast number coupled degrees of freedom. Therefore, an observable of a large number of particles or spins is calculated, e.g. the free energy, which is defined as multidimensional integral (over positions, velocities or spin states) and an estimate of the integral is obtained by averaging the value of the observable for a finite number of configurations. In Monte Carlo simulations this sequence of configurations is stochastic, rather than the deterministic time evolution of configurations realized in a molecular dynamics simulation. This strategy has been successfully employed to many different kinds of problems on physics including thermodynamics, structure and dynamics calculations, since the first simulations were employed by Metropolis et al. in the early 1950's [31] and due to a constant increasing capacity and availability of computer power as well as continuing development of specialized algorithms the Monte Carlo methods have become a major tool for physicists and chemists. As the 'quality' of the random sampling is a key to an accurate solution provided by a MC algorithm Metropolis *et al.* introduced the so called importance sampling, whereas configurations are generated proportional to their Boltzmann weight. In the following we will denote the states of a system of N particles or spins, which transitions are examined, as $\mathbf{r}^N = o$ ($o = old$) and $\mathbf{r}'^N = n$ ($n = new$) and thus for generating a sequence

of states obeying the Boltzmann distribution. State o has a Boltzmann factor given by $\exp\left[-\beta U(o)\right]/Q(N,V,T)$, where $U(o)$ is the potential energy of this configuration, $\beta = 1/k_B T$ the prescribed thermal energy and $Q(N,V,T)$ being the classical limit of the probability density function. In equilibrium there is no net flow between the states o and n, meaning that in equilibrium the number of accepted trial moves from state o to a particular state n should be exactly balanced by the number of accepted trial moves from a particular state n to o. This condition is called *detailed balance* and can be written as

$$p(o)T(o \to n) = p(n)T(n \to o), \tag{2.12}$$

where $p(\alpha)$ is the probability to be in state α and $T(\alpha \to o)$ denotes the transition probability to go from a state α to a state β. The transition probability itself is a product of two processes, the creation of a trial move $C(o \to n)$ and the acceptance of this trial move $A(o \to n)$,

$$T(\alpha \to \beta) = C(\alpha \to \beta)A(\alpha \to \beta). \tag{2.13}$$

In many Monte Carlo applications the creation of the trial moves is a symmetric process, i.e. the creation of the forward and backward moves have the same probability and thus $C(\alpha \to \beta) = C(\beta \to \alpha)$. Using this form, inserting eq. (2.13) in (2.12) and using Boltzmann weight $p(\alpha) = \exp[-\beta U(\alpha)]$ gives,

$$\frac{p(n)}{p(o)} = \frac{A(o \to n)}{A(n \to o)} = \exp\left\{-\beta[U(n) - U(o)]\right\} \tag{2.14}$$

The choice for $A(o \to n)$ to fulfill this condition is not unique, but one of the most efficient and most commonly used is the Metropolis rule,

$$A(o \to n) = \min(1, \exp\left\{-\beta[U(n) - U(o)]\right\}) \tag{2.15}$$

In practice a Monte Carlo translational move is performed as follows [23]:

1. select a particle i at random

2. calculate the present energy $U_i(o)$ of particle i

3. move particle i randomly

$$\mathbf{r}_i(n) = \mathbf{r}_i(o) + \gamma_{RND} \cdot \Delta\mathbf{r} \tag{2.16}$$

4. calculate new energy $U_i(n)$ of particle i

5. accept/reinject the move according to the Metropolis rule

In the scheme above γ_{RND} denotes a random number in the interval $[-1, 1]$ and Δ is the maximum displacement step, which is typically a tunable parameter of the implementation. The magnitude of $\Delta\mathbf{r}$ determines the efficiency of the Monte Carlo procedure. If the parameter is to large, many of the trial steps are rejected, but if the parameter is to

small phase space is sampled very slowly. A useful choice for $\Delta\mathbf{r}$ is a value such that half of the trial moves are accepted [23]. For the acceptance decision an additional random number θ_{RND} in interval $[0, 1]$ is generated and if $\theta_{RND} < p(o)/p(n)$ the move is realized. More details on the foundations of MC-algorithms can be found in literature [32–36].

An important extension to the standard MC approach is the so called *kinetic Monte Carlo method* (KMC) taking the time scale of the dynamic process into account. If the parametrized potential gives an accurate description of the atomic forces for the material being and assuming both that quantum mechanically effects are not important and that electron-phonon-coupling effects are negligible, then the dynamical evolution within molecular dynamics would be a very accurate representation of the real physical system. However, a serious limitation of MD is that accurate integration requires time steps short enough ($\sim 10^{-15}s$) to achieve a converged solution. Consequently, the total simulation time is typically limited to less than one microsecond, while processes we wish to study (e.g., diffusion and annihilation of defects after a cascade event) often take place on much longer time scales. This so called *time-scale problem* is partially solved by the KMC approach, which attempts to overcome this limitation by exploiting the fact that the long-time dynamics of this kind of systems typically consists of diffusive jumps from state to state rather than following a trajectory. This pathway of diffusive jumps is indicated in fig. 2.2. We imagine that for each M escape pathways we have an object with a length equal to the rate constant k_{ij} for the pathway. We assume these objects put end to end giving a total length k_{tot}. One has to choose now a single random position along the length of this stack of objects, thus the procedure gives a algorithm of choosing a particular pathway, that is proportional to the rate constant for that pathway. The average time for the system to escape from a state i into a state j is denoted as τ. It is related with the total escape rate

$$k_{tot} = \sum_j k_{ij} \tag{2.17}$$

with k_{ij} being the transition rate form state i into state j. Assuming an exponential time dependence for the transition probability $p_{ij}(t) = k_{ij} \exp(-k_{ij}t)$ leads straight forward to exponentially distributed random numbers for the escape time t. Therefore, we first choose a random number r on the interval $[0, 1]$, calculate its negative logarithm and multiply it with the inverse escape rate $1/k$:

$$t = -\frac{1}{k} \ln(r). \tag{2.18}$$

This strategy permits a rejection free „residence-time" procedure (visualized in fig. 2.2), which is often referred to as BKL algorithm, due to the work by Bortz, Kalos and Lebowitz occurring in 1975 for the simulation of an Ising spin system. It is import to note, that the transition rates k_{ij} can not be obtained by KMC itself, rather have to be calculated by other models, e.g. in the case of quantum systems the transition rates can be obtained from Fokker-Plancks equation. Additional informations on this approach can be found in [37,38].
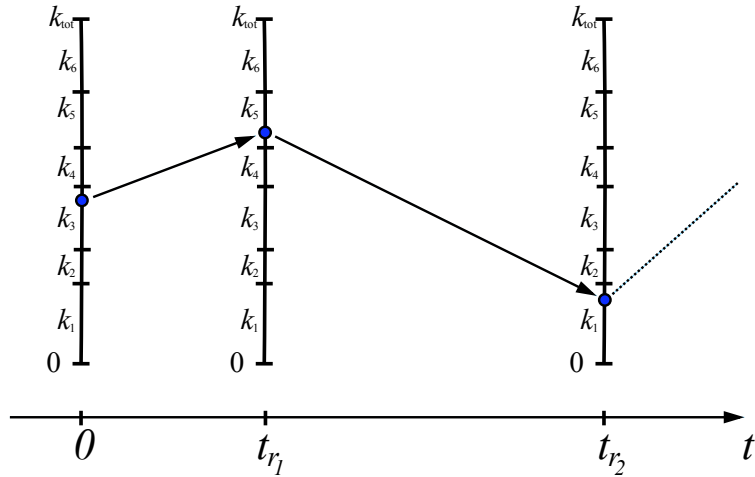
Figure 2.2: *Schematic describion of the kinetic Monte Carlo method. Every state transition occurs with a certain rate k_i, thus the total escape rate from a state is the sum k_{tot}, which is equal to the length of the vertical lines.*

2.2 Electronic structure calculation

In the previous section we discussed two methods for the calculation of atomic structures using classical, material specific forcefields. Their main advantage is the description of systems containing large numbers of atoms at long time-scales (range of seconds), which would be prohibitively costly for quantum chemistry methods. However, since we are interested into the correlation between structure and electronic/transport properties, we will solve the quantum mechanical problem for atomic structures given by our forcefield methods. In this section we briefly discuss the quantum mechanical methods used here – semi-empirical model Hamiltonians and density functional theory.

2.2.1 Extended Hückel Hamiltonian

In the present study we need to develope a model for the electronic structure of nano-junctions containing more than 800 atoms. In principle this would be also possible with density functional theory, but due to the fact that the electronic Hamiltonian has to be inverted for several snapshots of a system during a dynamic process DFT or *ab initio* methods would be prohibitively costly. Therefore, we decided to use semi-empirical approximations which where successfully applied to a large variety of nanostructures, e.g. organic molecules [13], nanotubes [39] and metallic nanowires [40, 41], and give at least qualitative predictions of the electronic properties.

One method is based on the so called *extended Hückel approximation* [42, 43], which is one of the first quantum chemistry methods and was developed in 1963 by Roland Hoffmann. He generalized the original *Hückel method* (which considers only π-orbitals) and takes also the σ-orbitals into account. As usual in quantum chemistry calculations we decouple the electronic and atomic nuclei Hamiltonian, which is also known as *Born-Oppenheimer approximation* [14, 15], based on the ratio of mass $m_{nuc}/m_{elec} \approx 1860$, so

the electrons follow the nuclear movement quasi adiabatically. In the extended Hückel method only valence electrons are considered and the inner shell electrons are assimilated in an effective nuclear core potential. The non-interacting valence electrons are treated via the single particle Hamiltonian

$$H_0 = -\sum_{i=1}^{M} \varepsilon_i c_i^\dagger c_i - \sum_{i,j=1}^{M}{}' t_{ij} c_i^\dagger c_j \qquad (2.19)$$

Here the index i enumerates all appearing atomic orbitals. If we have N atoms in the system and n_k denotes the number of orbitals in atom k then $i = 1 + \sum_{k=1}^{l-1} n_k, ..., \sum_{k=1}^{l} n_k$ enumerates all orbitals of atom l. The diagonal elements of the Hamiltonian ε_i are taken as the negative of the first ionization energies of the atom corrected by spectroscopic terms to deal with the situation where the ionization is not removing the orbital in question. The operator $c_i^\dagger$ (c_i) follows the notation of second quantization and creates (removes) an electron in orbital i. The off-diagonal matrix elements of the Hamiltonian are calculated according to the modified Wolfsberg-Helmholtz formula [43] and relates the diagonal elements $\varepsilon_i, \varepsilon_j$ and the overlap matrix element S_{ij} as follows:

$$t_{ij} = -\frac{c}{2}(\varepsilon_i + \varepsilon_j) S_{ij}. \qquad (2.20)$$

The constant c is also part of the Wolfsberg-Helmholtz approximation and set to an average value of 1.75 [43], but in general c is a function of the contributing orbitals i and j. As usual the overlap matrix element is given by

$$S_{ij} = \int d^3\bar{r} \; \chi_i^*(\bar{\mathbf{r}} - \mathbf{r}_i) \chi_j(\bar{\mathbf{r}} - \mathbf{r}_j), \qquad (2.21)$$

which is equal to δ_{ij} in the case of orthogonal basis functions $\chi_i(\bar{\mathbf{r}})$. In the present study we use so called *Slater type orbitals* (STO) [44, 45]

$$\chi_{nlm}^{\text{STO}}(r, \vartheta, \varphi) = N r^{n-1} e^{-\zeta r} Y_{lm}(\vartheta, \varphi) \qquad (2.22)$$

in all calculations combined with the extended Hückel method. Here N is a normalization constant and the parameter ζ occurring in (2.22) is related to the effective charge of the nucleus, which is partially screened by inner shell electrons, and the quantum numbers n, l, m. In the following application of this model to the atomic transistor conformers (see chapter 4) and molecular wires (see chapter 5), we include the outer $s-$, $p-$ and $d-$orbitals (i.e. 9 orbitals per silver-atom).

Widely used in quantum chemistry calculations are also Gaussian type orbitals (GTO) [46] defined by:

$$\chi_{nlm}^{\text{GTO}}(\mathbf{r}) = N_{ijk}^{\alpha}(x - R_1)^i (y - R_2)^2 (z - R_3)^k e^{-\alpha(\mathbf{r} - \mathbf{R})^2}, \qquad (2.23)$$

with a Gaussian type radial part. In general STO's should be preferred, because they exhibit the correct behavior of the molecular orbital close to the nuclei (where the wave
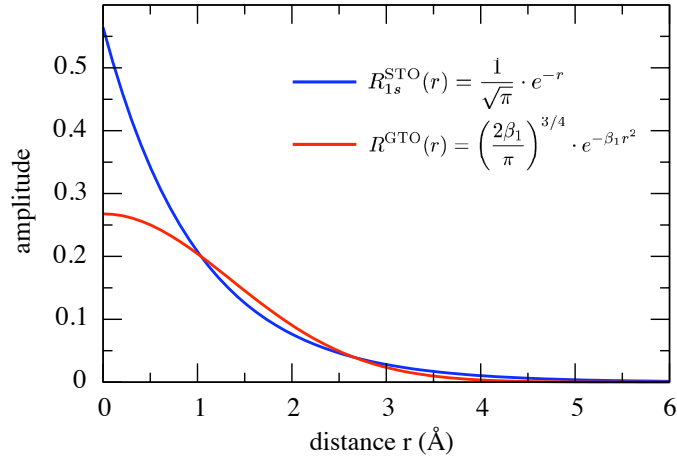
Figure 2.3: *Comparison between a normalized 1s-Slater function (radial part) of a hydrogen atom with the first normalized Gaussian function (radial part). The coefficient $\beta_1 \approx 0.271$ of the Gaussian function is obtained by maximizing the overlap $\int d^3 r R^{STO} R^{GTO} = max$. The 1s-STO equals the exact 1s wave function of the hydrogen atom, nevertheless the first Gaussian function shows strong deviations, in particular at $r = 0$ and in the decay for larger distances.*

function has to have a cusp) and for large distances from the nuclei (where the wave function has to exponentially decay to zero), at least if a so called „double zeta"[1] basis is used. The disadvantage of Slater functions is, that multi-center electron integrals lead to very complicate mathematical expressions which are difficult to implement and particularly expensive to evaluate. The disadvantage of the wrong behavior at $r = 0$ and for large distances of GTO's can be compensated by increasing the number of basis functions to a sufficient large basis set, e.g. with three GTO's per STO the computational effort for the integral calculations is still less than using a STO basis set [47]. Additionally one has to note, that the missing cusp of GTO's at $r = 0$ changes the total energy of an atom or a molecule, but leads to correct energy differences or excitation energies. Also the intermolecular interactions over large distances are rather conveyed by induction and dispersion than by electronic overlap. Such processes are described correctly with GTO's which is a reason for the success of GTO's in quantum chemistry. However, if we are interested in coherent electronic transport in dynamic systems, a high accuracy of overlap integrals in particular also at larger distances then at equilibrium is desirable.

It is known that in several cases the extended Hückel methode performs rather poorly at predicting energy differences between isomers or even correct molecular geomtries [48,49]. Charge differences particularly between atoms of very different electronegativity, can be grossly exaggerated. The strength of the extended Hückel model is that it gives a good qualitative picture of the molecular orbitals, e.g. it was shown that for the occupied molecular orbitals the corresponding eigenvalues agree reasonably well with experimentally determined ionization energies from photoelectron spectroscopy. In addition it was

---

[1]A double zeta function consists of two basis functions per atomic orbital, leading to two parameters ζ_1, ζ_2 for every atomic orbital.
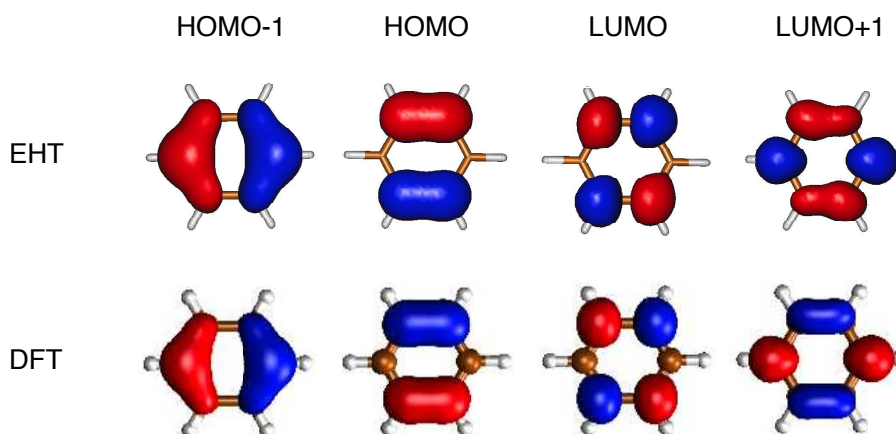
Figure 2.4: *Comparison between the frontier orbitals of benzene. The upper row shows the extended Hückel theory (EHT) results using a STO basis set. The row below shows DFT results obtained with Gaussian orbitals and the BP86 functional for the exchange-correlation energy, taken from ref [51]. The qualitative shape of the orbitals HOMO-1, HOMO and LUMO is approximately identically at the different levels of theory, however in the case of LUMO+1 deformations of the EHT orbitals are visible*

shown in 1988 in ref. [50], that this approach is also useful in predicting the first unoccupied levels. The reason for the good performance of extended Hückel in calculating the first excitation energies was discussed in [50] and traced back to the fact, that the form of this model Hamiltonian is derivable from the non-empirical Hartree-Fock-Roothan method.

2.2.2 Mean field theory and neglect of differential overlap

The extended Hückel method is a pure single-particle model - no electron-electron interaction is taken into account. A first step towards the inclusion of electron-electron interaction is to treat the surrounding electron gas of an electron as mean field, which is the underlying idea of the Hartree-Fock and semi-empirical molecular orbital methods [23]. Semi-emirical approaches are normally formulated within the same conceptual framework as *ab initio* methods, but they neglect many smaller integrals to speed up the calculations. In order to compensate for the errors caused by these approximations, empirical parameters are introduced into the remaining integrals and calibrated against reliable experimental or theoretical reference date. In current practice semi-empirical methods serve as efficient computational tools which can yield fast quantitative estimates for a number of properties. Compared with *ab initio* or density functional methods, semi-empirical calculations are much faster, typically by several orders of magnitude [52], but they are also less accurate with errors that are less systematic and thus harder to correct. Since all semi-empirical models are based on the Hartree-Fock method we will give a short derivation of this type of mean field Hamiltonian.

Assuming a system of interacting particles described by the Hamiltonian

$$H = H_0 + V_{\text{int}} \tag{2.24}$$

$$H_0 = \sum_i \varepsilon_i c_i^\dagger c_i \qquad (2.25)$$

$$V_{\mathrm{int}} = \frac{1}{2} \sum_{i,i',k,k'} V_{ik} c_i^\dagger c_k^\dagger c_{i'} c_{k'} \qquad (2.26)$$

with the single electron part H_0 and the interaction potential V_{int}. Using Wick's theorem, that states that if the particles can be treated as being independent (which is precisely the mean-field assumption) then the four-term operator can be expressed by all possible pairings of operators while keeping track of sign changes if two fermions are interchanged:

$$
\begin{aligned}
c_i^\dagger c_k^\dagger c_{i'} c_{k'} \approx \quad & c_i^\dagger c_{i'} \langle c_k^\dagger c_{k'} \rangle_{\mathrm{MF}} + \langle c_i^\dagger c_{i'} \rangle_{\mathrm{MF}} c_k^\dagger c_{k'} \\
\pm \quad & c_i^\dagger c_{k'} \langle c_k^\dagger c_{i'} \rangle_{\mathrm{MF}} \pm \langle c_i^\dagger c_{k'} \rangle_{\mathrm{MF}} c_k^\dagger c_{i'} \\
- \quad & \langle c_i^\dagger c_{i'} \rangle_{\mathrm{MF}} \langle c_k^\dagger c_{k'} \rangle_{\mathrm{MF}} \mp \langle c_i^\dagger c_{k'} \rangle_{\mathrm{MF}} \langle c_k^\dagger c_{i'} \rangle_{\mathrm{MF}} \qquad (2.27)
\end{aligned}
$$

where the upper sign is for bosons and the lower sign is for fermions. The expectation value $\langle \cdot \rangle_{\mathrm{MF}}$ is defined as $\langle V_{\mathrm{int}} \rangle = Z_{\mathrm{MF}}^{-1} \mathrm{Tr}[e^{-\beta H_{\mathrm{MF}}} V_{\mathrm{int}}]$ and $Z_{\mathrm{MF}} = \mathrm{Tr}[e^{-\beta H_{\mathrm{MF}}}]$. In order to avoid double counting in (2.27) we have to subtract the averages at the end of (2.27). The first two terms represent the direct interaction because they give the classical expectation value between two densities, while the exchange terms represent a quantum mechanical correction to this. Applying this to the interaction potential (2.26), we obtain on one hand from the direct interaction term the so called Hartree approximation

$$V_{\mathrm{int}}^{\mathrm{Hartree}} = \frac{1}{2} \sum V_{ik,i'k'} \bar{n}_{kk'} c_i^\dagger c_{i'} + \frac{1}{2} \sum V_{ik,i'k'} \bar{n}_{ii'} c_k^\dagger c_{k'} - \frac{1}{2} \sum V_{ik,i'k'} \bar{n}_{ii'} \bar{n}_{kk'}, \qquad (2.28)$$

and on the other hand from the exchange term the so called Fock term

$$V_{\mathrm{int}}^{\mathrm{Fock}} = -\frac{1}{2} \sum V_{ik,i'k'} \bar{n}_{ik'} c_k^\dagger c_{i'} - \frac{1}{2} \sum V_{ik,i'k'} \bar{n}_{ki'} c_i^\dagger c_{k'} + \frac{1}{2} \sum V_{ik,i'k'} \bar{n}_{ik'} \bar{n}_{ki'}. \qquad (2.29)$$

with $\bar{n}_{ik} = \langle c_i^\dagger c_k \rangle_{\mathrm{MF}}$. Finally the mean-field operator of the Hartree-Fock method writes as

$$H^{\mathrm{HF}} = H_0 + V_{\mathrm{int}}^{\mathrm{Fock}} + V_{\mathrm{int}}^{\mathrm{Hartree}} \qquad (2.30)$$

Semi-empirical quantum chemistry methods use (2.30) as starting point and apply additional approximations to H^{HF}. Traditionally there are three levels of integral approximation [53, 54] - CNDO (complete neglect of differential overlap), INDO (intermediate neglect of differential overlap) and NDDO (neglect of diatomic differential overlap) which is the best (of these three) since it retains the higher multipoles of charge distributions in the two center interactions (unlike CNDO and INDO which truncate after the monopole). The NDDO Hamiltonian H^{NDDO} includes only one-center and two-center terms which accounts much for its computational efficiency. An additional approximation in NDDO occurs in its eigenvalue problem $\sum_i (H_{ik}^{\mathrm{NDDO}} - S_{ik} \varepsilon_j) c_{kj} = 0$, where the overlap matrix is set to $S_{ik} = \delta_{ik}$. Conceptually the one-center terms are taken from atomic spectroscopic data, with the refinement that slight adjustment are allowed in the optimization to account for possible differences between free atoms and atoms in a molecule. The one-

center two-electron integrals derived from atomic spectroscopy data are considerably smaller than their analytically calculated values, which is (at least partly) attributed to an average incorporation of electron correlation effects.

2.2.3 Density functional theory

In many cases the EHT or NDDO approach simplifies the considered quantum system too strongly, e.g. if atoms with considerably different electronegativity are involved or highly accurate atomic structures are needed. However, a direct solution of the many-body Schrödinger equation depending on $3N$ spatial variables, with N being the number of electrons, seems to be unfeasible since even for small molecules N is often larger than 100 or for solids $N \approx 10^{23}$. Obviously the solution can not be obtained without approximations and the many electron wave function is a much too complicated object to understand or predict material properties. Density functional theory formally reduces the many electron problem to a single electron problem and uses the electron density distribution $n(r)$ as the elementary quantity instead of many electron wave functions, an idea which goes back to Thomas [55] and Fermi [56] and was extended by Hohenberg and Kohn [57].

For simplification, we consider a non-relativistic, non-spin-polarized, time-independent many-electron system at zero temperature, which has a non-degenerated ground state ψ described by the Schrödinger equation

$$\left[-\frac{\hbar^2}{2m} \sum_i^N \nabla_i^2 + \sum_{ij}^N U(\mathbf{r}_i, \mathbf{r}_j) + \sum_i^N v_{ext}(\mathbf{r}_i) \right] \psi(\mathbf{r}) = E\psi(\mathbf{r}). \tag{2.31}$$

Here $U(\mathbf{r}_i, \mathbf{r}_j) = e^2 |\mathbf{r}_i - \mathbf{r}_j|^{-1}$ denotes the electron-electron interaction and $v_{ext}(\mathbf{r}_i)$ the static external potential due to interaction of electrons with the atomic nuclei. The kinetic energy operator and the interaction potential are universal in the sense that they are the same for any system, while v_{ext} is system dependent.

The known *Hohenberg-Kohn theorem* states that (i) there is a unique mapping from the external potential to the ground state density and (ii) that the ground-state density is a uniquely determined functional of the external potential $n_0[v_{ext}(\mathbf{r})]$. The consequence of the first statement is, that since every wavefunction ψ (not only the ground state wave function) is trivially a functional $\psi[v_{ext}((r)]$ of the external potential, the wavefunction $\psi[v_{ext}[n_0(\mathbf{r})]]$ is also a functional of the ground state density. Thus every quantum mechanical observable, i.e. every expectation value $\langle\psi|\hat{O}|\psi\rangle$ is a functional of the ground-state density. The second statement of the Hohenberg-Kohn theorem is that a unique functional $E[n(\mathbf{r})]$ of the electron density $n(\mathbf{r})$ exists, which under the condition $\int n(\mathbf{r}) \, d^3r = N$ obtains its minimum for the ground-state density $n_0(\mathbf{r})$ and gives the ground-state energy as $E_0 = E[n_0(\mathbf{r})]$. The proof of the Hohenberg-Kohen theorem for non-degenerate ground states is simple and proceeds by reductio ad absurdum. It is shown that a contradiction arises if one assumes that two different ground states $\psi_0 \neq \psi_0'$, arising from two different potentials $v \neq v' + const$, lead to the same ground-state density $n_0(\mathbf{r})$. The proof is based on Rayleigh-Ritz principle for the ground state energy, which

is given by $E_0 = \langle \psi_0 | \hat{H}_v | \psi_0 \rangle$ assuming a normalized wavefunction. The complete proof can be found e.g. in [23].

Unfortunately, for most physical properties it is not known how they can be calculated directly from the ground state density. Therefore, the second part of the Hohenberg-Kohen theorem, which is the minimum principle for the ground state energy E_0, is of particular importance. According to Levy [58] the unique energy functional $E[n(\mathbf{r})]$ can be defined as the minimum over all wavefunctions, which deliver the density $n(\mathbf{r})$,

$$E[n(\mathbf{r})] = \min_{\psi \to n} \langle \psi | \hat{T} + \hat{U} + \hat{V}_{ext} | \psi \rangle \tag{2.32}$$

and can be written as

$$E[n(\mathbf{r})] = F[n(\mathbf{r})] + \int d^3r \; n(\mathbf{r}) v_{ext}(\mathbf{r}). \tag{2.33}$$

Here the simple functional dependence on v_{ext} is explicitly displayed. The functional

$$F[n(\mathbf{r})] = \min_{\psi \to n} \langle \psi | \hat{T} + \hat{U} | \psi \rangle \tag{2.34}$$

is universal, which means that it does not depend on v_{ext} and is the same for all systems described by the Schrödinger equation (2.31). From (2.32) one obtains

$$E[n(\mathbf{r})] = \langle \psi_n^{min} | \hat{T} + \hat{U} + \hat{V}_{ext} | \psi_n^{min} \rangle \geq E_0, \tag{2.35}$$

where ψ_n^{min} is defined as the wavefunction, which delivers the minimum, and where the inequality follows from the Rayleigh-Ritz minimum principle for the ground state energy E_0. If the ground state wavefunction ψ_0 is used in (2.32) one obtains

$$E[n_0(\mathbf{r})] \leq \langle \psi_0 | \hat{T} + \hat{U} + \hat{V}_{ext} | \psi_0 \rangle = E_0 \tag{2.36}$$

where it has been used that the ground-state wavefunction delivers the ground-state energy and where the inequality follows from (2.32), because $E[n_0(\mathbf{r})]$ is defined as the minimum over all wavefunctions, which give the ground-state density $n_0(\mathbf{r})$, and one of these wavefunctions is the ground state wavefunction ψ_0. Since (2.35) is valid for any density, it is also valid for the ground state density. This leads to $E[n_0(\mathbf{r})] \geq E_0$, which together with (2.36) shows $E_0 = E[n_0(\mathbf{r})]$ and establishes the minimum principle

$$E_0 = \min_n E[n(\mathbf{r})]. \tag{2.37}$$

Here the minimization is over all densities which arise from antisymmetric wavefunctions for all N electrons. This variational principle can be used to determine the ground-state density of $n_0(\mathbf{r})$ and energy E_0 provided that the functional $F[n(\mathbf{r})]$ can be defined explicitly, which is, however, only possible approximately.

As important as the the Hohenberg-Kohn theorem is the idea of Kohn and Sham [59], to introduce a fictitious auxiliary non-interacting electron system with an effective external potential $v_{eff}(\mathbf{r})$. This effective potential is constructed in such a way that the density

of the auxiliary non-interactig system equals the density of the interacting system of interest. The Hohenberg-Kohn theorem (applied for $U \equiv 0$) guarantees the one-to-one correspondence between the densities and the effective potentials. While the functional $F[n(\mathbf{r})]$ in (2.33) and (2.34) is universal with respect to the external potential, it evidently depends on the interaction U. For $U \equiv 0$ the functional $F[n(\mathbf{r})]$ reduces the kinetic energy functional $T_s[n(\mathbf{r})]$ of non-interacting electrons and the total-energy functional can be written as

$$E_s[n(\mathbf{r})] = T_s[n(\mathbf{r})] + \int d^3r \ n(\mathbf{r})v_{eff}(\mathbf{r}). \tag{2.38}$$

The Hohenberg-Kohn variational principle (2.37) then lead to the Euler-Lagrange equation

$$\frac{\delta}{\delta n(\mathbf{r})} \left\{ E_s[n(\mathbf{r})] + \mu \left[N - \int d^3r \ n(\mathbf{r}) \right] \right\} = \frac{\delta T_s[n(\mathbf{r})]}{\delta n(\mathbf{r})} + v_{eff}(\mathbf{r}) - \mu = 0 \tag{2.39}$$

where a Lagrange parameter μ is used to guarantee the charge conservation $N = \int d^3r \ n(\mathbf{r})$. Equation 2.39 provides an exact way to calculate the ground-state density $n(\mathbf{r})$ provided that the potential $v_{eff}(\mathbf{r})$ is known, since the functional $T_s n(\mathbf{r})$ for the kinetic energy of the non-interacting electrons can be implicitly constructed by using the single-particle wave-functions (orbitals) $\phi_i(\mathbf{r})$, which allow to represent $n(\mathbf{r})$ and T_s in the form

$$n(\mathbf{r}) = \sum_i^{occ} |\phi_i(\mathbf{r})|^2 \ \ \text{and} \ \ T_s[n(\mathbf{r})] = \sum_i^{occ} \int d^3r \ \phi_i^*(\mathbf{r}) \left(-\frac{\hbar^2}{2m}\nabla_{\mathbf{r}}^2 \right) \phi_i(\mathbf{r}) \tag{2.40}$$

where i denotes both the spatial as well as the spin quantum numbers and where the sum is over the lowest N (occupied) eigenstates to respect the Pauli principle. The variation of $E[n(\mathbf{r})]$ with respect to the orbitals leads to the Kohn-Sham equations

$$\left[-\frac{\hbar^2}{2m}\nabla_r^2 + v_{eff}(\mathbf{r}) - \mu \right] \phi_i(\mathbf{r}) = \varepsilon_i \phi_i(\mathbf{r}), \tag{2.41}$$

where the ε_i represent Lagrange parameters, which guarantee that the orbitals are normalized as $\langle \phi_i | \phi_i \rangle = 1$. To apply this scheme, a useful expansion of the effective potential v_{eff} must be found. The important achievement of Kohn and Sham was the suggestion to write equation (2.33) as

$$E[n(\mathbf{r})] = T_s[n(\mathbf{r})] + \int d^3r \ n(\mathbf{r})v_{ext}(\mathbf{r}) + \frac{e^2}{2} \int d^3r d^3r' \ \frac{n(\mathbf{r})n(\mathbf{r}')}{|\mathbf{r} - \mathbf{r}'|} + E_{xc}[n(\mathbf{r})]. \tag{2.42}$$

Here the last term is the so called exchange-correlation energy functional defined as

$$E_{xc}[n(\mathbf{r})] = F[n(\mathbf{r})] - T_s[n(\mathbf{r})] - \frac{e^2}{2} \int d^3r d^3r' \ \frac{n(\mathbf{r})n(\mathbf{r}')}{|\mathbf{r} - \mathbf{r}'|} \tag{2.43}$$

As before, $T_s[n(\mathbf{r})]$ is the kinetic energy functional (2.40) of non-interacting electrons.

The variational principle applied to (2.42) gives

$$\frac{\delta T_s[n(\mathbf{r})]}{\delta n(\mathbf{r})} + v_{ext}(\mathbf{r}) + e^2 \int d^3r' \, \frac{n(\mathbf{r}')}{|\mathbf{r} - \mathbf{r}'|} + \frac{\delta E_{xc}[n(\mathbf{r})]}{\delta n(\mathbf{r})} - \mu = 0. \qquad (2.44)$$

This equation is formally identical with the Euler-Lagrange equation (2.39) of the non-interacting electron system with the effective potential

$$v_{eff}(\mathbf{r}) = v_{ext}(\mathbf{r}) + e^2 \int d^3r' \, \frac{n(\mathbf{r}')}{|\mathbf{r} - \mathbf{r}'|} + v_{xc}[n(\mathbf{r})](\mathbf{r}) \qquad (2.45)$$

where the exchange correlation potential is defined as

$$v_{xc}[n(\mathbf{r})](\mathbf{r}) = \frac{\delta E_{xc}[n(\mathbf{r})]}{\delta n(\mathbf{r})}. \qquad (2.46)$$

Equations (2.40) and (2.41) are the most famous Kohn-Sham equations, which are probably the most important equations in density-functional theory. Since the effective potential depends on the density via (2.45) and the density on the effective potential via (2.40) and (2.41), these equations must be solved self-consistently: starting from a trial density the effective potential is determined by (2.45), for which (2.40) and (2.41) are solved to determine the new density. This process is repeated until the new density equals the previous one.

The density-functional theory presented above is exactly in principle, however the density functionals $E_{xc}[n(\mathbf{r})]$ and $v_{xc}[n(\mathbf{r})]$, in which all complications of the many-particle problem are hidden, are not exactly known and must be approximated. The widespread use of density-functional theory in calculating physical and chemical properties arises from the fact, that approximations for E_{xc} and v_{xc} have been found, which are both simple and accurate enough for practical applications. A simple but remarkably good approximation is the so called local density approximation (LDA), which approximates the $E_{xc}[n(\mathbf{r})]$ at every point $\mathbf{r}$ with the local exchange-correlation energy of a homogeneous electron gas (for details see e.g. [60,61]) and thus yields good results for systems with slowly varying electron densities. An even better approximation for calculating cohesive energies and lattice constants (i.e. of 3d transition metals) permits the so called generalized gradient approximation (GGA), which takes the dependence of the gradient of the density into account [62–64]. A possibility to improve these exchange-correlation functionals has been suggested by Becke [65], who constructed a non-local hybrid functional by using a fraction of exact exchange. Additional improvements in the description on exchange and correlation where achieved by coupling-constant integration and constrained DFT, but since this section should give only an overview of the methods we refer the reader to specialized literature [66–70].

# 2.3 Landauer-Büttiker theory of coherent transport

2.3.1 Introduction

In the limit of strong coupling between electrodes and central device region the so called „Landauer-Büttiker-approach" [12], which expresses the current through a conductor in terms of the probability that an electron can transmit through it, has proven to be very successful [12, 71, 72]. It allows for the investigation of the current-voltage characteristics of many promising systems of molecular electronics like metallic point contacts, nano-wires, nano-tubes as well as covalently coupled complex molecules (e.g. DNA). The main idea behind this approach is to describe the source-drain electrodes as ballistic conductors and to treat the device region of interest as scattering center for the charge carriers. This scattering process can be described by the scattering matrix of the device, which contains the transmission and reflection coefficients of the scattering-channels. Computing these scattering channels makes it necessary to use an appropriate method to describe the electronic structure (semi-empirical model Hamiltonian like tight-binding or density functional theory) for the molecular orbital calculations, that allows for an accurate electronic structure treatment at a reasonable level of computational costs.

In the present section we will briefly introduce the Landauer-Büttiker formalism of coherent electron transport, which is required for the interpretation of the results obtained from simulations. Firstly we will demonstrate the close correlation of transmission and the experimentally accessible conductance. For reasons of practical calculations we will show how to express the transmission function in terms of Green's functions. This concept is also required for introducing the Recursive Green's function method in the next section, which was implemented for material specific transport calculations and extensively used in the present work.

2.3.2 Transmission and conductance

In order to observe coherent conductance quantization at least two conditions on the sample size have to be fulfilled: To preserve coherent scattering the device length should be smaller than the quantum mechanical coherence length of the electrons and the device width has to be small enough permitting only a few number of charge carrying modes. The first experimental validation of conductance quantization in a two dimensional ballistic waveguide was reported independently by two different groups in 1988 [73, 74]. Figure 2.5 shows a schematic of the experimental setup where a semiconductor (GaAs-AlGaAs heterostructure) connected to source/drain electrodes on the left and right and to two gate electrodes (split-gate configuration) of negative potential forming a bottleneck for the electron propagation. The gate electrodes generate fixed boundary conditions in y-direction leading to quantized transversal modes similar to a 1D-potential pot, where the number of occupied modes N_C in the central device in dependence on the width W of the pot is given by:

$$N_C = \text{Int}\left[\frac{W}{\lambda_F/2}\right] \tag{2.47}$$
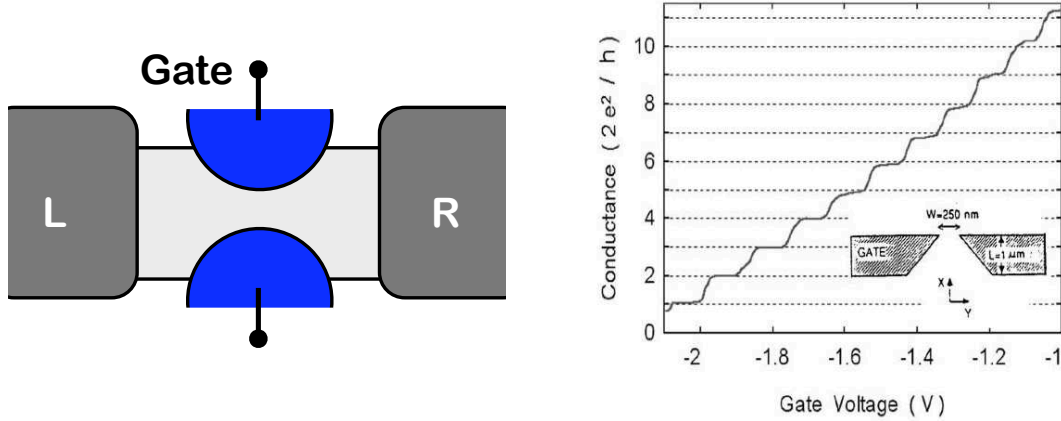
Figure 2.5: *Experimental verification of conductance quantization in a quantum point contact. (left) Experimental setup showing the semi-conductor in the middle connected to source/drain (L/R) and constricting gate electrodes. (right) Observed conductance steps as function of the gate voltage proving the varring number of perfectly transmitting channels (Original data by van Wees et al. [73])*

Here λ_F denotes the Fermi-wave length of the system. Measuring the conductance in dependence on the gate voltage yields the characteristic shape in the curve shown in figure 2.5: As the width W of the constriction decreases continuously the number of occupied modes in the conductor decreases and the conductance goes down in discrete steps in units of $2e^2/h$, as the channels are perfectly transmitting. In the following, we will understand the effect of coherent conductance quantization in a quantitative way based on the Landauer formalism.

To derive the relation between conductance and transmission for the multi-channel, noninteracting case, first of all it has to clarified to which systems the Landauer formalism is restricted: (i) We consider only systems without inelastic scattering in the contact/device region - the transport is assumed to be coherent. (ii) The electrodes are assumed to be ideal Fermi liquids, i. e. the electrons entering the device region from the left or right have a distribution according to the Fermi distribution function and the chemical potentials μ_L, μ_R of the corresponding left or right lead, respectively. (iii) Electrons leaving the device region into the reservoirs are completely absorbed, i. e. the electrodes are assumed to be reflectionless.

According to the division of the system into three parts - left electrode, the central device region and right electrode we divide also the corresponding Hamiltonian matrix into the block Hamiltonians H_L/H_R for the left/right lead and H_C describing the central device, respectively. We assume, that there is no direct coupling between the left and the right contact:

$$H = \begin{pmatrix} H_L & H_{LC} & 0 \\ H_{CL} & H_C & H_{CR} \\ 0 & H_{RC} & H_R \end{pmatrix}, \quad \text{with} \quad H_L = H_R = \begin{cases} \frac{1}{2m}\mathbf{p}^2, & \mathbf{r}_\perp \in [0,W] \times [0,W] \\ \infty, & \text{otherwise} \end{cases}$$

(2.48)

Here H_{XX} with $X = L, R$ denotes the coupling between electrode and central system and W is the width of the electrodes. H_L and H_R describe non-interacting electrons in a perfectly ballistic conductor.

Restricting to the incoming and outgoing waves in the leads we now define the so-called scattering states, which have an incoming part in one particular lead state in x-direction, a transmitted part and a reflected part. Due to the finite width of the leads, the incoming wave has a discrete mode number index n and, as we treat an open system, a continuos varying wave number index k in direction of the charge flux. A wave function, representing a right moving scattering state ($k, k' > 0$) takes the for:

$$\psi_{nk}(x, \mathbf{r}_\perp) = \begin{cases} e^{ikx}\chi_n(\mathbf{r}_\perp) + \sum_{n'} \hat{r}_{n'n} e^{-ik'x}\chi_{n'}(\mathbf{r}_\perp), & (x, \mathbf{r}_\perp) \in L \\ \sum_{n'} \hat{t}_{n'n} e^{-ik'x}\chi_{n'}(\mathbf{r}_\perp), & (x, \mathbf{r}_\perp) \in R \end{cases}.$$

(2.49)

The matrix element $\hat{t}_{n'n}$ represents the transmission amplitude for an incoming wave from the left in state n to be transmitted into state n' on the right hand side, whereas $\hat{r}_{n'n}$ is the respective reflection amplitude. $\chi(\mathbf{r}_\perp)$ is the wave function component in transverse direction $\mathbf{r}_\perp$. As long as we can neglect inelastic scattering, the wavenumbers are fixed by energy conservation, so for the mode energies holds $\varepsilon_{nk} = \varepsilon_{n'k'}$. If we denote $\hat{t}'_{n'n}$ and $\hat{r}'_{n'n}$ as respective amplitudes in opposition direction, we can define the energy dependent scattering matrix, which comprises all occurring amplitudes

$$\mathbf{S}(E) = \begin{pmatrix} \hat{\mathbf{r}}(E) & \hat{\mathbf{t}}'(E) \\ \hat{\mathbf{t}}(E) & \hat{\mathbf{r}}'(E) \end{pmatrix} \quad \text{with} \quad \hat{\mathbf{r}}(E) = \{\hat{r}_{n'n}(E)\}$$

(2.50)

and maps (if the wave functions are e. g. expanded in plane waves) the incoming wave coefficients to the outgoing wave coefficients. As the current is proportional to the velocity v_{nk} times the square of the wave function, $|\psi_{nk}|^2$, we have to rescale the transmission amplitudes,

$$t_{n'n} = \sqrt{\frac{v_n}{v_{n'}}}\, \hat{t}_{n'n}$$

(2.51)

in order to retrieve the commonly used formulation of the Landauer formula. Now $|t_{n'n}|$ constitutes the fraction of the inflowing current in the left lead which is transmitted into the right lead. To derive an expression for the total current, we consider a single transverse mode whose $+k$ states are occupied according to the Fermi distribution function $f_L(E)$. A uniform electron gas with N electrons per unit length moving with a velocity v carries a current equal to eNv. Since the electron density associated with a single k-state in a conductor of length L is $(1/L)$, we can write the current I_L carried by the $+k$ states

in mode n as

$$I_{nL} = \frac{e}{L} \sum_{k,n'} v \; f_L(E) \; |t_{n'n}|^2 = \frac{e}{L} \sum_{k,n'} \frac{1}{\hbar} \frac{\partial E}{\partial k} \; f_L(E) \; |t_{n'n}|^2 \tag{2.52}$$

Converting the sum over k into an integral according to the usual prescription

$$\sum_k \quad \longrightarrow \quad 2(\text{for spin}) \times \frac{L}{2\pi} \int dk \tag{2.53}$$

one obtains

$$I_{nL} = \frac{2e}{h} \int dE \; f_L(E) \sum_{n'} |t_{n'n}|^2 \tag{2.54}$$

$$\text{with} \quad f_L(E) = f(E - \mu + eV_L) \tag{2.55}$$

Here V_L denotes the applied potential to the left electrode. Summing I_{nL} over all modes n carrying right moving waves yields

$$I_L = \sum_n I_{nL} = \frac{2e}{h} \int dE \; f_L(E) \text{Tr}(\mathbf{t}\mathbf{t}^\dagger). \tag{2.56}$$

with the energy dependent transmission function $T(E) = \text{Tr}\left[\mathbf{t}(E)\mathbf{t}^\dagger(E)\right]$. We can evaluate a similar expression for the current I_R carried by the $-k$ states. So the total current I is given by

$$I = I_L - I_R = \frac{2e}{h} \int dE \; \text{Tr}(\mathbf{t}\mathbf{t}^\dagger) \left[f_L(E) - f_R(E)\right] \tag{2.57}$$

which is called *Landauer-Büttiker-formula*. This equation shows, that the current of a coherent non-interacting quantum system can be expressed by an energy integral over the channel transmission $T(E)$ weighted by the difference of the left and right reservoir Fermi function which defines the energy interval of the electron flow. So the whole information about the coherent transport properties of the system is given by the transmission function, whereas f_L and f_R characterize the boundary conditions. However, the transmission $T(E)$ is revoking of experimental observation, but it is directly related to the zero bias conductance: At low bias voltages $(V_L - V_R)$ we can expand the expression (2.57) for the total current I around μ leading to

$$I = \frac{2e^2}{h} \int dE \; \text{Tr}(\mathbf{t}\mathbf{t}^\dagger) \left(-\frac{\partial f}{\partial E}\right) (V_L - V_R). \tag{2.58}$$

The conductances G is given by

$$G = \frac{I}{V_L - V_R} = \frac{2e^2}{h} \int dE \; \text{Tr}(\mathbf{t}\mathbf{t}^\dagger) \left(-\frac{\partial f}{\partial E}\right). \tag{2.59}$$

Further, we assume low temperatures simplifying the derivative of the Fermi function to

$$\frac{\partial f(E)}{\partial E} \approx \delta(E - E_F) \quad \Longrightarrow \quad G = G_0 \, T(E_F). \tag{2.60}$$

Equation (2.60) is called *Landauer Formula* and states the important result, that the conductance is equal to the transmission in units of the conductance quantum $G_0 = 2e^2/h$.

2.3.3 Green's functions in scattering theory

So far we discussed how the coherent transport properties, i. e. the zero bias conductance G and the total current I, follow from the transmission function $T(E)$. In principal we can evaluate the matrix elements of $(\mathbf{tt}^\dagger)$ by solving the four equations resulting from the continuity conditions of the single particle wavefunction and its derivative on the left an right interface, which is non trivial in general, because this procedure includes the calculation of an explicit expression for the wavefunction.

A more convenient method for calculating the transmission matrix, which is in principal not essential for coherent transport, is the Green's function approach. Unlike the transmission matrix, which correlates only points at the interfaces, the Green's function $G^R(r, r')$ describes the response at any point r due to an excitation at point r', particularly inside the conductor. So $G^R(r, r')$ can be interpreted as a generalized transmission matrix, which has several advantages compared to the transmission matrix:

1. The Green's function description permits a formal substitution of the infinite sized system by a finite central transport region incorporating the open boundary conditions via so called self-energies (see chapter 2.3.4) which provides a convenient method for evaluating the Green's function and i. e. the transmission of an open system numerically.

2. It allows for the relation of scattering theory to other formalisms, e.g. like Kubo formalism, transfer Hamiltonian method and Feynman's path-integral method.

3. Interaction effects like electron-phonon scattering and electron-electron interaction occurre inside the conductor and though are not accessible with the transmission matrix. However the Green's function can take such effects into account within the so called Keldish formalism.

Propagator of Schrödinger's equation

In quantum mechanics the Green's function can be interpreted as propagator of Schrödinger's equation [75], so one needs to find an operator $K(\mathbf{r}_2, t_2; \mathbf{r}_1, t_1)$ that maps all contributions of a wave function $\psi(\mathbf{r}_1, t_1)$ at points $\mathbf{r}_1$ at t_1 to the wave function
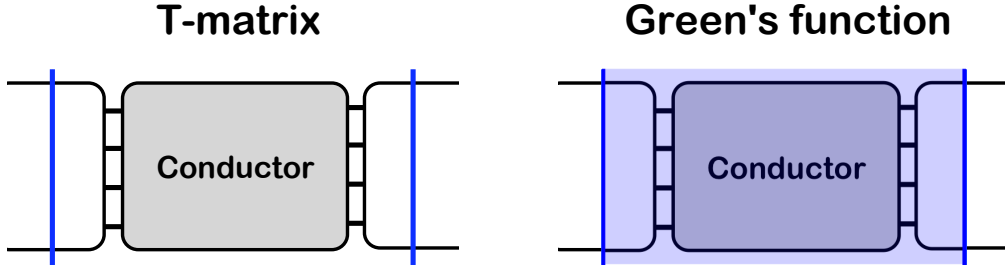
Figure 2.6: *Description of the scattering problem using two different approaches: (left) The transmission matrix correlates only inflowing wavefunctions with outflowing wavefunctions defined on the colored lines at the interfaces. However the Green's function, a generalized transmission matrix, correlates point lying also inside the conductor.*

$\psi(\mathbf{r}_2, t_2)$ in point $\mathbf{r_2}$ in the past t_2:

$$\psi(\mathbf{r}_2, t_2) = \int d^3 r_1 K(\mathbf{r}_2, t_2; \mathbf{r}_1, t_1) \psi(\mathbf{r_1}, \mathbf{t_1}) \tag{2.61}$$

Using the time evolution operator $U(t_2, t_1)$ with $|\psi(t_2)\rangle = U(t_2, t_1)|\psi(t_1)\rangle$, completeness $\int d^3 r_1 |\mathbf{r}_1\rangle\langle\mathbf{r}_1| = \mathbb{1}$ and the restriction $t_1 < t_2$ (introducing a theta-function), we can identify

$$K(\mathbf{r}_2, t_2; \mathbf{r}_1, t_1) = \theta(t_2 - t_1)\langle\mathbf{r}_2|U(t_2, t_1)|\mathbf{r}_1\rangle. \tag{2.62}$$

Assuming that the Hamiltonian H is not explicitly time dependent, and $H|\psi_n\rangle = E_n|\psi_n\rangle$, the time evolution operator U can be written as

$$U(t_2, t_1) = \sum_n e^{-iE_n(t_2 - t_1)/\hbar}|\psi_n\rangle\langle\psi_n| \tag{2.63}$$

Inserting (2.63) into (2.62) yields an explicit expression for the propagator

$$K(\mathbf{r}_2, t_2; \mathbf{r}_1, t_1) = \theta(t_2 - t_1)\sum_n \psi_n^*(\mathbf{r}_1)\psi_n(\mathbf{r}_1)e^{-iE_n(t_2 - t_1)/\hbar} \tag{2.64}$$

However, also formulation (2.64) requires the knowledge of the eigenfunctions. To determine the propagator without calculating the ψ_n we can derive a partial differential equation defining K. Therefore, we apply the operator $[i\hbar\partial_{t_2} - H(\mathbf{r}_2, \nabla_2)]$ corresponding to Schrödingers equation to (2.64) and obtain

$$[i\hbar\partial_{t_2} - H(\mathbf{r}_2, \nabla_2)] K(\mathbf{r}_2, t_2; \mathbf{r}_1, t_1) = i\hbar\delta(t_2 - t_1)\sum_n \psi_n^*(\mathbf{r}_1)\psi_n(\mathbf{r}_1)e^{-iE_n(t_2 - t_1)/\hbar} \tag{2.65}$$

The RHS of (2.65) is non-vanishing only if $t_1 = t_2$, so the exponential function can be neglected and with $\sum \psi_n^*(\mathbf{r}_1)\psi_n(\mathbf{r}_2) = \delta(\mathbf{r}_2 - \mathbf{r}_1)$ we obtain finally

$$[i\hbar\partial_{t_2} - H(\mathbf{r}_2, \nabla_2)] K(\mathbf{r}_2, t_2; \mathbf{r}_1, t_1) = i\hbar\delta(t_2 - t_1)\delta(\mathbf{r}_2 - \mathbf{r}_1). \tag{2.66}$$

For a unique solution it is necessary to add the condition $K(\mathbf{r}_2, t_2; \mathbf{r}_1, t_1) = 0$, if $t_1 > t_2$.

From a physical point of view, that means the waves propagating from the surface $t = t_1$ only „radiate" into the future, so (2.66) is called *retarded propagator*. Usually a solution of an equation with a 4-dimensional delta-function as inhomogenity is called *Green's function*, so we denote this special propagator as G in the next sections.

In the following we will show how the elements of the transmission matrix $\hat{t}_{n'n}$ can be expressed by the Green's function. The necessary formula is called *Fisher-Lee-relation* [76], which we derive for a one-dimensional single-mode wire and afterwards generalize it to a two-dimensional multi-mode wire.

We restrict the derived differential equation 2.66 to one dimension in space and assume a static situation (no time dependence). A constant one-dimensinal potential for the electrons is denoted as U_0. The resulting propagator is called Green's Operator:

$$G = \left[E - U_0 + \frac{\hbar^2}{2m} \frac{\partial^2}{\partial x^2} \right]^{-1} \tag{2.67}$$

According to the common concept of Green's function method, this operator is applied to a Green's function $G(x, x')$, resulting in a δ-function.

$$\left(E - U_0 + \frac{\hbar^2}{2m} \frac{\partial^2}{\partial x^2} \right) G(x, x') = \delta(x - x') \tag{2.68}$$

The function at the right hand side is often called source term, so we can view $G(x, x')$ as a wavefunction at x resulting from a unit excitation applied at x'. This local excitation gives rise to two plane waves traveling outwards from x' with the amplitudes a^- and a^+ for the left and right traveling part, respectively. Therefore, one solution of (2.68) is

$$G^R(x, x') = \begin{cases} a^+ e^{ik(x-x')}, & x > x' \\ a^- e^{-ik(x-x')}, & x < x' \end{cases} \quad \text{with} \quad k = \sqrt{\frac{2m(E - U_0)}{\hbar^2}}, \tag{2.69}$$

which is called *retarded Green's function*. Using the continuity condition for $G^R(x, x')$ and $\partial_x G^R(x, x')$ at $x = x'$ one finds $a^- = a^+ = -im/\hbar^2 k$, thus (2.69) can be simplified to

$$G^R(x, x') = -\frac{im}{\hbar^2 k} e^{ik|x-x'|}. \tag{2.70}$$

Since the defining equation of $G(x, x')$ is a second order differential equation, there is an additional solution $G^A(x, x')$ of (2.68), the *advaced Green's function*

$$G^A(x, x') = +\frac{im}{\hbar^2 k} e^{-ik|x-x'|} \tag{2.71}$$

which consists of incoming waves that disappear at point x' and thus satisfies a different boundary condition than $G^R(x, x')$ corresponding to outgoing waves. As the retarded Green's function represents the physically relevant solution one incorporates the boundary condition into (2.68) by adding an infinitesimal imaginary part to the energy, with

$\eta > 0$:

$$\left(E + i\eta - U_0 + \frac{\hbar^2}{2m} \frac{\partial^2}{\partial x^2} \right) G(x, x') = \delta(x - x'). \tag{2.72}$$

This introduces a positive imaginary part also in the wavenumber $k \to k(1 + i\delta)$. Inserting the transformed wavenumber into the expression for $G^R(x, x')$ and $G^A(x, x')$ shows that the advanced solution diverges for large distances $|x - x'|$, in contrast to the retarded solution. Therefore, in the following discussion of non-interacting transport we will focus on the physically reasonable retarded Green's function.

According to [12] we will now discuss, how to express the transmission matrix in terms of the Green's function. Therefore we consider a conductor connected to a set of leads. We use different coordinate systems in each lead, e.g. in lead p we have coordinates (x_p, y_p) and in lead q the coordinates (x_p, y_p), respectively (compare fig. 2.7). The interface of the conductor at lead p is defined by the line $x_p = 0$. As previously discussed, the transmission matrix relates only points at the interfaces, so we can restrict the Green's function to

$$G^R_{qp}(y_q; y_p) \equiv G^R(x_q = 0, y_q; x_p = 0, y_p). \tag{2.73}$$

If we neglect the transverse dimension y, we can easily write down the Green's function between interface p and interface q in terms of the transmission matrix. A local excitation at interface p would give rise to two plane waves into both directions: one into contact p with amplitude a^-_p and another one which is scattered at the conductor is split into a reflected component with amplitude $t^+_{pp} a^+_p$ and a transmitted component $t^+_{qp} a^+_p$, so the 2-point Green's function writes as

$$G^R_{qp} = \delta_{qp} a^-_p + t_{qp} a^+_p. \tag{2.74}$$

Since we know from the previous discussion that the amplitudes $a^{\pm}_p$ are equal to $-im/\hbar^2 k$ and $t_{qp} = \sqrt{v_p/v_q} \, \hat{t}_{qp}$ we obtain for the transmission matrix elements

$$\hat{t}_{qp} = -\delta_{qp} + i\hbar \sqrt{\nu_q \nu_p} \, G^R_{qp} \tag{2.75}$$

To generalize the formalism to a multi-mode wire we consider the Green's function of a two-dimensional region, which is infinite in the left and right direction ($-\infty \leq x \leq +\infty$,) and finite in transverse direction ($0 \leq y \leq y_L$). According to the definition of the Green's function (see equation (2.64)) $G(\mathbf{r}, \mathbf{r}') = \sum_m \psi_m(\mathbf{r}) \psi^*_m(\mathbf{r}')$ and the fact that we can separate the wavefunction in x- and y-direction, the Green's function takes the form [12]:

$$G^R(x, y, x', y') = \sum_m -\frac{i}{\hbar \nu_m} \chi_m(y) \chi_m(y') e^{ik_m |x - x'|}. \tag{2.76}$$

The prefactor $-i/\hbar \nu_m$, with $\nu_m = \hbar k_m/m$, is again a consequence of the continuity of G^R and $\partial_x G^R$ in $x = x'$. $\chi_m(y)$ denote the transverse mode wavefunctions which are real, orthogonal and satisfy the equation $\left[-(\hbar^2/2m)\partial^2_y + U(y) \right] \chi_m(y) = \varepsilon_{m,0} \chi_m(y)$. The ex-

ponential factor in (2.76) follows directly from the previous one-dimensional calculation. To find the relation between Green's function and transmission for a multi-mode wire we consider again a conductor connected to a set of leads, e.g. lead p and lead q. We restrict the Green's function to interfaces given by the lines $x_p = 0$ and $x_q = 0$ as in the previous example. Due to the existence of a scattering region (the conductor) we have to replace the unperturbed traveling plane waves in x-direction in (2.76) by their scattered transmission/reflection-amplitudes:

$$-\frac{i}{\hbar \nu_m}e^{ik_m|x_q - x_p|} \quad \mapsto \quad \sum_n -\frac{i}{\hbar\sqrt{\nu_n \nu_m}}(\delta_{nm} + \hat{t}_{nm})e^{-ik_n x_q}e^{+ik_m x_p} \tag{2.77}$$

Hence we obtain for the Green's function in the leads (no x-dependence) with scattering effects

$$G^R_{qp}(y_q, y_p) = \sum_{m \in p}\sum_{n \in q} \chi_n(y_q)\left[\delta_{nm} + \hat{t}_{nm}\right]\chi_m(y_p). \tag{2.78}$$

Solving this equation for $\hat{t}_{nm}$ by using the orthogonality of the transversal wave functions we find the generalized *Fisher-Lee-relation* for multi-mode wires

$$\hat{t}_{nm} = -\delta_{nm} + i\hbar\sqrt{\nu_n \nu_m}\int\int dy_q dy_p \ \ \chi_n(y_q)\ G^R_{qp}(y_q, y_p)\ \chi_m(y_p). \tag{2.79}$$

We can use the previous equation to derive an expression for the transmission function $T(E)$ giving less more physical insights, but is rather important for numerical applications. Therefore we discretize the two-dimensional space using the Finite Differences scheme with a lattice constant a. The indices i and j enumerate the interface contact points to lead p and q, respectively (compare figure 2.7b). As we assume scattering into different leads (so $n \neq m$) we obtain for the discretized version of (2.79)

$$\hat{t}_{nm} = i\hbar\frac{\sqrt{\nu_n \nu_m}}{a}\sum_{i,j}\chi(q_j)G^R_{qp}(j,i)\chi_m(p_i). \tag{2.80}$$

Finally the total transmission function follows from the summation $\sum_{n,m}|\hat{t}_{nm}|^2$ over all
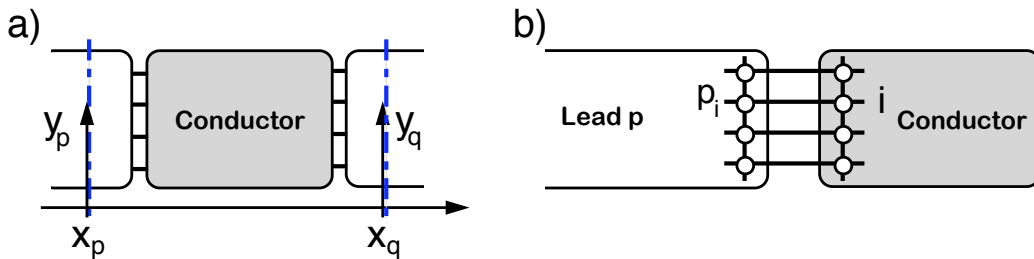
Figure 2.7: *Schematics to clarify the notation in the derivation of the Fisher-Lee relation. (a) Conductor between two leads p and q with longitudinal coordinate x and transversal coordinate y. (b) Discretized connection between lead p (transversal coordinate p_i) and a conductor (transversal coordinate i).*

transversal modes n and m

$$T_{qp} = \frac{\hbar^2 \nu_n \nu_m}{a^2} \sum_{i,j,i',j'} \chi_n(q_j)G^R(j,i)\chi_m(p_i) \; \chi_n(q_{j'})G^A(i',j')\chi_m(p_{i'}) \tag{2.81}$$

with the advanced Green's function $G^A(i',j') = \left[G^R(i',j')\right]^\dagger$. Furthermore we introduce the coupling matrices Γ_p describing the connection strength between electrode and conductor

$$\Gamma_p(i,i') = \sum_{m \in p} \chi_m(p_i)\frac{\hbar \nu_m}{a}\chi_m(p_{i'}). \tag{2.82}$$

We will discuss their physical meaning and an efficient way to calculate them in next subsection in relation with the so called self-energies. With coupling matrix we obtain finally a simple expression for the transmission function which is of high relevance for applications:

$$\begin{aligned}
T_{qp} &= \sum_{i,j,j',i'} \Gamma_q(j',j)G^R(j,i)\Gamma_p(i,i')G^A(i',j') \tag{2.83} \\
&= \mathrm{Tr}\left[\Gamma_q G^R \Gamma_p G^A\right] \tag{2.84}
\end{aligned}$$

2.3.4 Self-energy

So far we described how the total current carried by coherent, non-interacting electrons can be traced back to the transmission function and the electrode Fermi functions using the Landauer Büttiker formula. Furthermore we derived an expression for the transmission which permits efficient numerical implementation based on Green's functions. However it is not obvious, how to handle the Green's function or even the Hamiltonian matrix H of an open quantum system. The Hamiltonian of an infinite chain of atoms has infinite dimensions by definition and since the Green's function is proportional to the inverse of H (see (2.67)) it is necessary to divide the system of interest into two semi-infinite lead- and a central device region. Additionally, the algorithm should exploit the translation invariance of the contacts and permit an accurate treatment of the central device region, which determines basically the transport properties of the system.

To map the infinite dimensional Hamiltonian to a finite matrix, suitable for numerical methods, we consider a system consisting of only one lead connected to a conductor. Formally we separate the full Green's function G of the total system into the semi-infinite block matrix of the lead G_L and the finite block matrix of the central region G_C:

$$\begin{pmatrix} G_L & G_{LC} \\ G_{CL} & G_C \end{pmatrix} \equiv \begin{pmatrix} (E - i\eta)\mathbb{1} - H_L & \tau_L \\ \tau_L^\dagger & E\mathbb{1} - H_C \end{pmatrix}^{-1} \tag{2.85}$$

Here $\tau_L(E) = (E - i\eta) - H_{LC}$ denotes an overlap matrix between the two subsystems. Generating the identity matrix on the LHS of equation (2.85) and comparing the matrix

elements left and right we obtain two linear equation for G_{LC} and G_C:

$$[(E - i\eta)\mathbb{1} - H_L] G_{LC} + [\tau_L] G_C = 0 \tag{2.86}$$

$$[E\mathbb{1} - H_C] G_C + \left[\tau_L^\dagger\right] G_{LC} = \mathbb{1} \tag{2.87}$$

Solving for the overlap matrix G_{LC} leads to $G_{LC} = -g_L^R \tau_L G_C$ with the retarded Green's function of the contact $g_L^R = [(E - i\eta)\mathbb{1} - H_L]^{-1}$, which can be computed using an iterative scheme to be discussed at a later section. Plugging the result into the equation for G_C yields

$$G_C = \left[(E - i\eta)\mathbb{1} - H_C - \tau_L^\dagger g_L^R \tau_L\right]^{-1}. \tag{2.88}$$

This is the finite dimensional Green's function of the central region taking the influence of the lead into account by the so called *self energy* $\Sigma_L = \tau_L^\dagger g_L^R \tau_L$ of the contact. In general the conductor is connected to a number of leads. For this case we can straight forward extend the upper formalism to the total self-energy term $\Sigma = \sum_X \tau_X^\dagger g_X^R \tau_X$, leading to

$$G_C = [(E - i\eta)\mathbb{1} - H_C - \Sigma]^{-1}. \tag{2.89}$$

Introducing the self-energy Σ has certain consequences for the eigenstates of the investigated system. Many common quantum systems can be treated as closed systems, whose eigenstates are found by diagonalizing the Hamiltonian H_C with $H_C \psi_{\alpha 0} = \varepsilon_{\alpha 0} \psi_{\alpha 0}$. However, in the present study we are interested in open systems, i.e. a microscopic structure strongly coupled to leads. This gives rise to a self-energy Σ^R leading to an perturbed Hamiltonian $[H_C + \Sigma^R]$. Therefore, the eigenvalue problem changes to

$$\left[H_C + \Sigma^R\right] \psi_\alpha = \varepsilon_\alpha \psi_\alpha. \tag{2.90}$$

The most important difference to the unperturbed problem is, that the eigenvalues ε_α are complex, due to the non-hermiticity of the self-energy Σ^R. Using the derivative of the dispersion relation $\nu_m = \hbar^{-1} \partial_k \varepsilon_m(k)$ and the definition (2.82) one can show [77] that the coupling matrices Γ are proportional to the imaginary part of the self-energy Σ^R

$$\Gamma = i[\Sigma^R - \Sigma^A]. \tag{2.91}$$

If the coupling Γ vanishes, the imaginary part of Σ^R vanishes and $[H_C + \Sigma^R]$ would be hermitic, which would lead non-complex eigenvalues. However, in an open system the eigenvalues are in general complex

$$\varepsilon_\alpha = \varepsilon_{\alpha 0} - \Delta_\alpha - i(\gamma_\alpha/2) \tag{2.92}$$

with $\varepsilon_{\alpha 0}$ denoting the eigenvalues of the isolated conductor corresponding to the Hamiltonian H_C. The shift on the real axis Δ_α can be interpreted as modification of the dynamics of the electrons inside the conductor and the shift on the imaginary axis $\gamma_\alpha/2$ reflects the possibility that electrons can disappear into the contacts. This eigenvalue-shift induced by the self-energies (i.e. by the contacts) changes also the life-time of the eigenvalues: Moving from an isolated to an open system, the time dependence of the

eigenstates transforms as

$$\exp\left[-i\varepsilon_{\alpha 0}t/\hbar\right] \quad \rightarrow \quad \exp\left[-i(\varepsilon_{\alpha 0} - \Delta_\alpha)t/\hbar\right] \quad \exp\left[-\gamma_\alpha t/2\hbar\right]. \tag{2.93}$$

The squared amplitude of the wave function yields the probability $|\psi_\alpha|^2 \exp(-\gamma_\alpha t/\hbar)$ with the constant $\hbar/\gamma_\alpha$, which represents the average time an electron remains in state α before it escapes out into the leads. The case $\gamma_\alpha = 0$ corresponds to a vanishing coupling $\Gamma = 0$ leading to an infinite „live time" $\hbar/\gamma_\alpha$.

2.3.5 Electrode surface Green's functions and decimation technique

In order to describe the effects of the semi-infinite contacts on the device, we calculate the self-energy matrixes Σ_X $(X = l, r)$, which arise formally out of partitioning an infinite system and projecting out the contact Hamiltonians. As already discussed, we can finally calculate the electrode self-energy explicitly from the surface Green's functions discussed in the present section.
We follow the decimation technique presented in [13]. The in-plane (xy-plane) lattice periodicity of an empty metallic surface suggests the calculation of the surface Greens function in k-space. Therefore we choose a k-point mesh defined by

$$\mathbf{k}(n,m) = \frac{2\pi m}{M}\mathbf{k}_1 + \frac{2\pi n}{N}\mathbf{k}_2, \quad \text{with} \quad m = -\frac{M-1}{2}, ..., \frac{M-1}{2} \quad \text{and } n \text{ analog}, \tag{2.94}$$

where $\mathbf{k}_1$ and $\mathbf{k}_2$ denote the basis vectors and (m, n) specify one single point of the k-mesh. In the case of a fcc-[111] layer the basis vectors in real space are $\mathbf{r}_1 = a(1, 0, 0)$ and $\mathbf{r}_2 = a(\frac{1}{2}, \frac{\sqrt{3}}{2}, 0)$. In reciprocal space, which is defined by $\mathbf{r}_i \cdot \mathbf{k}_j = 2\pi \cdot \delta_{ij}$, this leads to $\mathbf{k}_1 = \frac{2\pi}{a}(1, -\frac{1}{\sqrt{3}}, 0)$ and $\mathbf{k}_2 = \frac{2\pi}{a}(0, \frac{2}{\sqrt{3}}, 0)$.
A fcc-lattice in [111] direction consists of metallic layers of the stacking order ABCABC...
. In a single-particle description the knowledge of the Hamiltonian H_a of one „ABC" unit is sufficient to build up the Hamiltonian of the full semi-infinit electrode due to translational invariance. Once the matrix elements of the real-space Hamiltonian $h_{a,ij}$ and overlap matrix elements $s_{a,ij}$ are given (e.g. from a tight-binding model), we perform a Fourier transformation on the established set of k-points

$$H^a(\mathbf{k}) = \sum_j h_{a,ij}\, e^{-i\mathbf{k}(\mathbf{r}_i - \mathbf{r}_j)}, \qquad S^a(\mathbf{k}) = \sum_j s_{a,ij}\, e^{-i\mathbf{k}(\mathbf{r}_i - \mathbf{r}_j)}. \tag{2.95}$$

Due to lattice symmetry in xy-plane, we can keep $i = 1$ fixed (arbitrarily chosen) and let j run over all atom indices of one „principal layer" (i.e. ABC-unit). Similarly, we define $H^b(\mathbf{k})$ and $S^b(\mathbf{k})$ (see Fig. 2.8), but with j numbering only atoms of the nearest neighbor principal layers. In order to write the surface Green's function in a compact manner, we introduce the matrixes $\alpha(\mathbf{k})$ and $\beta(\mathbf{k})$ corresponding to the intra- and inter-layer coupling, respectively.

$$\alpha(\mathbf{k}) := (E + i\eta 0^+)S^a(\mathbf{k}) - H^a(\mathbf{k}), \qquad \beta(\mathbf{k}) := (E + i\eta 0^+)S^b(\mathbf{k}) - H^b(\mathbf{k}) \tag{2.96}$$
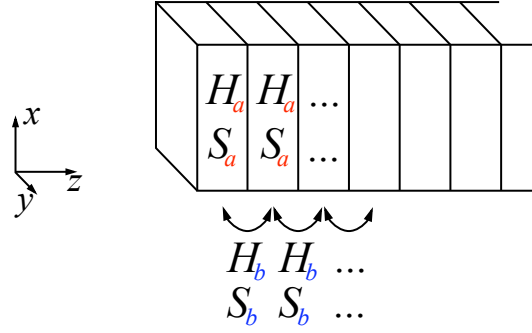
Figure 2.8: *Lead consisting of „principal layers", whereas every layer can be described with the real space single-particle Hamiltonian H_a and the corresponding overlapp matrix S_a resulting from the non-orthogonal basis set. The electronic overlap between two neighboring principal layers is given by H_b and S_b, repectivly*

The infinitesimal positive complex number $i\eta$ was introduced to ensure the convergence of the Fourier transformation and can be interpreted as extraction of the electrons from the contact. Using these definitions the Green's function of an semi-infinite lead can be written as follows:

$$G_{lead}(\mathbf{k}) = \begin{pmatrix} \alpha(\mathbf{k}) & \beta(\mathbf{k}) & 0 & \cdots \\ \beta^\dagger(\mathbf{k}) & \alpha(\mathbf{k}) & \beta(\mathbf{k}) & \\ 0 & \beta^\dagger(\mathbf{k}) & \alpha(\mathbf{k}) & \ddots \\ \vdots & & \ddots & \ddots \end{pmatrix}^{-1} \stackrel{!}{=} \begin{pmatrix} g_s(\mathbf{k}) & \cdots & \\ \vdots & \ddots & \\ & & \end{pmatrix} \tag{2.97}$$

Since we are only interested in the Green's function $g_s(\mathbf{k})$ on the surface of the lead, we can solve (2.97) for the matrix element $(1,1)$ of the RHS, which leads to the recursive relation

$$g_s(\mathbf{k}) = \left[\alpha(\mathbf{k}) - \beta(\mathbf{k}) \; g_s(\mathbf{k}) \; \beta^\dagger(\mathbf{k}) \right]^{-1} \tag{2.98}$$

$\alpha(\mathbf{k})$ and $\beta(\mathbf{k})$ are explicitly known matrices, so we can either solve this equation analytically (if $\alpha(\mathbf{k})$ and $\beta(\mathbf{k})$ are one dimensional) or by iteration starting from a reasonable guess for $g_s(\mathbf{k})$, e.g. the Green's function $g_s^0(\mathbf{k})$ of a single isolated principal layer. Solving the RHS of (2.98) with $g_s = g_s^{(0)}(\mathbf{k})$ leads to an improved version of g_s. Repeating this procedure recursively leads to a converged surface Green's function in k-space. Transforming $g_s(\mathbf{k})$ back to real space

$$g_s(\mathbf{r}_i - \mathbf{r}_j) = \frac{1}{NM} \sum_{m,n} e^{i\mathbf{k}(n,m)(\mathbf{r}_i - \mathbf{r}_j)} g_s(\mathbf{k}(n,m)) \tag{2.99}$$

gives us the surface Green's function, which is now compatible with the Hamiltonian of the central device region.

Recently, Kletsov and Dahnovsky could extend this method to a non-recursive scheme with an infinite number of principal layers [78] as well es interacting lead electrons [79].

2.3.6 Spectral function and local density of states

The spectral function is an important concept to characterize the electronic structure of an open quantum system and can be interpreted as a generalized local density of states. It is defined as the anti-hermitian part of the Green's function:

$$A(E) := i \left[G^R(E) - G^A(E) \right].$$ (2.100)

In order to get more insights into the physical meaning of this quantity, we have to plug in the eigenfunction expansion of the Green's function

$$G^R(\mathbf{r}, \mathbf{r}', E) = \sum_\alpha \frac{\psi_\alpha(\mathbf{r}) \phi_\alpha^*(\mathbf{r}')}{E - \varepsilon_\alpha}$$ (2.101)

into equation (2.100). From a mathematical point of view (2.101) is just the spectral representation of the propagator (2.89). However one has to note, that the occurrence of $\psi_\alpha \phi_\alpha^*$ is due to the fact, that the ψ_α with $\left[H_C + \Sigma^R \right] \psi_\alpha = E_\alpha \psi_\alpha$ do not form a complete orthonormal set. To achieve a orthogonality one needs the eigenfunctions ϕ_α defined by $\left[H_C + \Sigma^A \right] \phi_\alpha = E_\alpha^* \phi_\alpha$ following from the adjoint self energy Σ^A as well. It can be shown (e.g. [80]) that the combination of these sets of eigenfunctions fulfills the property $\int d^3r \ \phi_\alpha(\mathbf{r}) \psi_\beta^*(\mathbf{r}) = \delta_{\alpha\beta}$.
Using the definition of $A(E)$ and the expansion (2.101) the spectral function reads as

$$A(\mathbf{r}, \mathbf{r}', E) = \sum_\alpha \psi_\alpha(\mathbf{r}) \phi_\alpha^*(\mathbf{r}') \frac{\gamma_\alpha}{(E - \varepsilon_{\alpha 0} + \Delta_\alpha)^2 + (\gamma_\alpha/2)^2}.$$ (2.102)

Assuming that the eigenfunctions $\{\psi_\alpha, \phi_\alpha\}$ and eigenvalues ε_α depend weakly on the energy E the spectral function versus E consists of Lorenzian curves with peaks at energies corresponding to the eigenvalues of the isolated conductor. Due to electrode coupling these peaks are shifted by the above introduced parameter Δ_α and broadened by γ_α.
The diagonal elements of the spectral function contain the local density of states

$$\rho(\mathbf{r}, E) = \frac{1}{2\pi} A(\mathbf{r}, \mathbf{r}, E) = -\frac{1}{\pi} \Im \left[G^R(\mathbf{r}, \mathbf{r}, E) \right].$$ (2.103)

which provides insights into the spatial variation of states on a surface or a conductor. In the limit of $\gamma_\alpha \to 0$ the local density of states (2.103) yields the usual expression for isolated systems $\rho(\mathbf{r}, E) = \sum_\alpha \delta(E - \varepsilon_{\alpha 0}) |\psi_\alpha(\mathbf{r})|^2$. With the advent of scanning tunneling microscopy (STM) it has become feasible to probe the local density of states on an atomic scale thus making this concept helpful from an experimental point of view.
The trace of the spectral function corrected by the overlap matrix S represents the total density of states:

$$D(E) = \frac{1}{2\pi} \text{Tr} \left[A(E) \cdot S \right].$$ (2.104)

Also $D(E)$ converges in the limit of vanishing coupling ($\gamma_\alpha \to 0$) to the result of the isolated system $D(E) = \sum_\alpha \delta(E - \varepsilon_{\alpha 0})$. However, (2.104) provides a general expression

for the density of states that can be used even when eigenstates have finite lifetime.

2.4 Recursive Green's function method

In the upper section (2.2.1) we have shown how the computational effort for the calculation of electronic structure can be significantly reduced, if the system is describable with a short range electronic Hamiltonian. The division of the system into principal layers allows for a fast evaluation of an approximate Green's function of every block Hamiltonian. In the following we discuss an iterative algorithm called *recursive Green's function method* [81] for calculating the layer Green's function recursively and reducing the system size needed for the conductance calculation to a minimal set of atoms.

The transport experiments investigated in this work operate in the limit of low bias voltages, so the system can be treated in the framework of linear response theory. However, an electric potential profile has to be assumed, which is in our case a simple stepwise potential between layer 0 and layer 1 (compare fig. 2.9). First of all we have to define the position operator, which is given by

$$x = \sum_{i \in L(k>0)} c_i^\dagger c_i, \tag{2.105}$$

where $c_i^\dagger$ creates an electron in orbital i (with i restricted to the layers of the device region; k is the layer index as indicated in fig. 2.9). H_0 should denote the equilibrium tight binding like Hamiltonian of the central device region. With the position operator x we can define also the perturbing Hamiltonian H_1 with

$$H_1 = -eV\cos(\omega t)x, \quad \text{and} \quad H = H_0 + H_1 \tag{2.106}$$

including a simple cosine time dependence. The perturbation produces transitions among stationary eigenstates of the system leading to a time dependent current. The total charge at the device region is given by

$$Q = -e \sum_{i \in L(k>0)} c_i^\dagger c_i = -e\ x. \tag{2.107}$$

With equation (2.107) we can calculate the charge traversing the sample per unit time using the equation of motion for the current operator I:

$$i\hbar I = [H, Q] = -e[H, x] = -ei\hbar v_x \tag{2.108}$$

Applying the explicit expression for the Hamiltonian $H = H_0 + H_1$ and the position operator x we obtain an expression for the velocity of the electrons passing the left electrode-device interface

$$i\hbar v_x = - \sum_{i \in L(1); j \in L(j)} h_{ij}(c_i^\dagger c_j - c_j^\dagger c_i) \quad \text{and} \quad I = -ev_x. \tag{2.109}$$
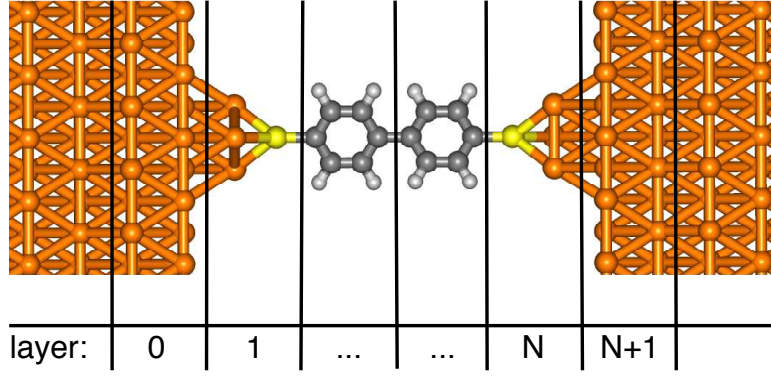
Figure 2.9: *Two phenyle rings connected via sulfur atoms to two gold electrodes. The ring units naturally prescribe a layer division of the system. The enumeration of the layers is shown below the junction geometry: Note that the first electrode layer of the left (right) contact is denoted as 0 (N + 1) and the „central device region" consists of the layers 1 to N.*

with the overlap matrix element h_{ij}. So in the case of a "small" perturbation potential V the knowledge of the charge flux between the left lead and the sample is sufficient to evaluate the total current through the system. This important result is of course related to flux conservation along the whole system.

Let us in the following denote as layer 0 and $N + 1$ the entire left and right electrode fragment, respectively (see Fig. 1(b)). The computation of the Green's function starts at the rightmost layer of the central region of the system, containing the rightmost device layer N and the semi-infinite right lead layer $N + 1$. Its electronic structure is reflected in the retarded Green's function matrix

$$G^r_{N,N+1} = \begin{pmatrix} ES_N - H_N & ES_{N,N+1} - H_{N,N+1} \\ ES_{N+1,N} - H_{N+1,N} & ES_{N+1} - H_{N+1} \end{pmatrix}^{-1}, \qquad (2.110)$$

which is more conveniently expressed in terms of the layer-self-energies Σ^r. The self-energy Σ^r_N of the right contact can be computed from the retarded surface Green's function $g^r(E)$ [81] as

$$\begin{aligned} \Sigma^r_N &= (ES_{N+1,N} - H_{N+1,N})(ES_{N+1} - H_{N+1})^{-1} \\ &\quad \times (ES_{N,N+1} - H_{N,N+1}) \qquad (2.111) \\ &\approx \tau_{N+1,N}(E)\, g^r_{N+1}(E)\, \tau^\dagger_{N+1,N}(E) \qquad (2.112) \end{aligned}$$

Here τ_{ij} denotes the coupling matrix of the layers i and j. The numerical scheme to project the influence of the semi-infinite contacts to the lead surface atoms has been already described in more detail in section 2.3.5. We can calculate the Green's function and self-energy of every principal layer k recursively, using the relations:

$$\begin{aligned} g^r_k(E) &= (ES_k - H_k - \Sigma^r_k(E))^{-1} \qquad (2.113) \\ \Sigma^r_{k-1}(E) &= \tau_{k-1,k}(E)\, g^r_k(E)\, \tau^\dagger_{k-1,k}(E) \qquad (2.114) \\ &\text{with} \quad k = N, ..., 2. \end{aligned}$$

In a layered system, we have chosen the interface such that the velocity operator has non-vanishing terms only for orbitals connecting the left-most electrode layer (layer 0) with orbitals in layer 1. To compute the Green's function occurring in the Landauer formula for the transmission (2.60) we thus need only the retarded Green's function of the system comprising layer 0 and layer 1

$$\mathcal{G}^r(E) = [ES_{01} - H_{01} - \Sigma_0^r(E) - \Sigma_1^r(E)]^{-1}, \tag{2.115}$$

which is easily computed from the right- and left-lead self energies Σ_i^r $(i = 0, 1)$. In order to exploit the simplicity of the velocity operator in this context, we use a formulation of Landauer formula for conductance (2.60) which is derivable from linear response theory [77] in the limes $\omega \to 0$ and which is equivalent with (2.60):

$$G(E) = \frac{2e^2}{h}\text{Tr}\left[(i\hbar v_z)\text{Im}\,\mathcal{G}(E)\,(i\hbar v_z)\text{Im}\,\mathcal{G}(E)\right] \tag{2.116}$$

The main difference to this an the previous representation of the conductance (or transmission function) is the appearance of the velocity operator, which can be understood if we consider the definition of the coupling matrixes (2.82) showing the proportionality $\Gamma_p \sim \hbar v$. For a detailed derivation of (2.60) from Kubo's formula for conductance the reader is referred to [77]. The occurring imaginary part of the Green's function can be calculated easily with the use of the advanced Green's function $\mathcal{G}^a$

$$\text{Im}\,\mathcal{G}(E) = \frac{1}{2i}\left[\mathcal{G}^r(E) - \mathcal{G}^a(E)\right] \quad \text{with} \quad \mathcal{G}^a(E) = [\mathcal{G}^r(E)]^{\dagger} \tag{2.117}$$

It is well known that the conductance is very sensitive to interference effects that arise form small atomic displacement [40, 41]. These effects lead to weak oscillations in the total transmission at $T = 0$ which are averaged out in most quantum transport measurements at higher temperature. To account for this phenomenon we average $G(E)$ over a small interval $[E_F - \Delta, E_F + \Delta]$ around the Fermi energy E_F,
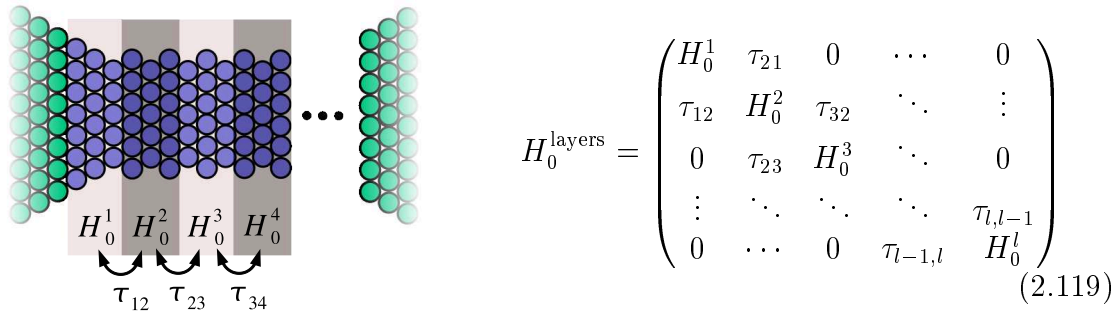
$$\langle G(E_F)\rangle = \frac{1}{2\Delta}\int_{E_F-\Delta}^{E_F+\Delta} \text{d}\varepsilon\, G(E) \tag{2.118}$$

whereas $\Delta = 50$ meV $\approx 2k_B T$ to obtain a representative value of the zero-bias conductance for comparison with experimental data.

2.4.1 Truncation of the Extended Hückel Hamiltonian

An aim of the present study is to calculate the conductance of nano-junctions consisting of up to 600 atoms during a dynamic process with varying conformation. To keep the computational effort feasible, we divide the quasi one-dimensional system into N principal layers perpendicular to current flow direction. Every principal layer k with $k = 1, ..., N$ is described with one block Hamiltonian matrix. Since the Hamiltonian of the central device region is diagonal dominant, we take only the overlap matrixes between nearest neighboring blocks (or principal layers) into account. Thus, an atom of layer k

has non-vanishing orbital overlap with other atoms in layer k and $k \pm 1$, but the overlap matrix elements to atoms in layer $k \pm 2$ are set to zero. So far, the layer thickness w is a parameter of the simulation which has to be chosen appropriately: is w too small, too many overlap matrix elements are neglected and the resulting conductance would underestimate the true value; on the other hand is w chosen to large, the computational effort comes close to the full device calculation, which should be avoided. However, if a reasonable thickness parameter d was found, we can exploit the advantage of the present layer-approximatimation: the linear scaling of the computational effort with the system length.

$$H_0^{\text{layers}} = \begin{pmatrix} H_0^1 & \tau_{21} & 0 & \cdots & 0 \\ \tau_{12} & H_0^2 & \tau_{32} & \ddots & \vdots \\ 0 & \tau_{23} & H_0^3 & \ddots & 0 \\ \vdots & \ddots & \ddots & \ddots & \tau_{l,l-1} \\ 0 & \cdots & 0 & \tau_{l-1,l} & H_0^l \end{pmatrix} \tag{2.119}$$

Figure 2.10: *(left) Division of the central device region into a set of principal layers. Every principal layer contains a few number of e.g. bulk layers. (right) Corresponding truncation of the full device Hamiltonian. The resulting matrix consists of block Hamiltonians corresponding the principal layers and nearest neighbor overlap between every block.*

2.4.2 Convergence-test of the layer approximation

Metallic nanowires have been among the first and most widely studied systems in molecular electronics [40,41,82,83]. Metallic systems are often most challenging for linear-scaling electronic structure methods, because the electronic wave functions are extended. To provide a stringent test for our „local" approximation, we have investigated the convergence of the layer approximation for two representative examples, namely gold- and silver-wires respectively.

We begin the investigation by dividing silver and gold model junctions into a set of „principal layers" with increasing thickness w. In order to establish the convergence of the method for large systems, the test geometry has to be of sufficient length. Here we investigate junctions of 45.2 Å length in z-direction, containing 388 silver or gold atoms with a nearest neighbor distance of 2.88 Å in both metals [84,85]. We prepare the electrodes as perfect fcc-clusters, which narrow towards the center to form a single-atom point contact at their tips, generating a dimer structure which permits a current flow in the crystallographic [111] direction. The extended molecule region and the layer divisions

are illustrated in Fig. 2.11a. The bulk electrodes are designated by the two larger layers on each side of the system.

We calculate the conductance for varying widths $w = 1, \ldots, 18$ d$_{[111]}$ of the „principal layers" (Fig. 2.11a), i.e. the full length of the extended molecule region. Figure 2.11b shows that the conductance of the silver and gold model junction as a function of the principal layer thickness w converges rapidly to the experimental value. The same holds true for the junction conformations labeled Ag 1 - Ag 4 and Au 1 - Au 4, which have a minimum cross section of 1-4 atoms, respectively. Furthermore, we calculated the convergence of the conductance for longer wire geometries (Fig. 2.11c), constructed by sequentially introducing additional atoms into the point contact at the minimum cross section. Thereby we obtain silver and gold junctions of 20, 24, 28 and 32 atomic layers in the z-direction.
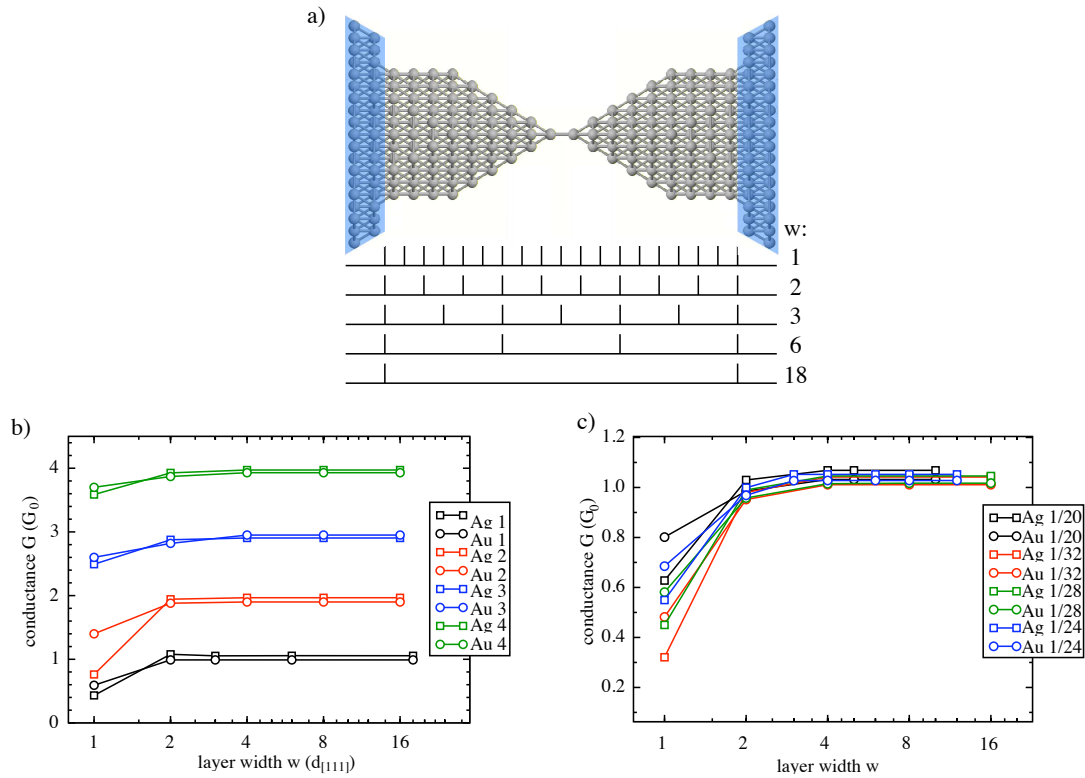
Figure 2.11: *Convergence test of the conductance depending on the „principal layer"-thickness for several nano-junctions. (a) Model nanojunction of 45.2 Å length and minimal cross section of one atom allowing for several different principal layer divisions, indicated by the marked lines below the conformation. On the right hand side the thickness of the principal layers of the actual division is indicated, respectively. w is given in units of the [111] atomic layer distance $d_{[111]} = 2.35Å$ (b) Corresponding conductance values for the upper described sets of „principal layers" for a silver and a gold contact, respectively. The dependence of the conductance on the layer division is also shown for similar metallic junctions with a minimal cross section of 2, 3 and 4 atoms, respectively. (c) Metal quantum wires with one conductance quantum, but with increasing length between 20 and 32 atomic layers show the same rapid convergence behaviour with increasing principal layer thickness.*

For $w = 1$ the conductance is significantly underestimated to approximately 0.5 G_0 for both metals, indicating that hopping processes across distances larger than the inter-atomic distance are important. For all choices of the layer thickness with $w > 1$ the conductance has converged to nearly the experimental values. For $w = 3$ the layer division retains the symmetry of the [111] crystal stacking order "ABCABC..." in fcc-latices. We investigate the convergence in more detail at the level of the transmission in Fig 2.12, which shows the total transmission function $\tau(E)$ of the geometry shown in Fig. 2.11a over an energy interval $[E_F - 6$ eV$, E_F + 6$ eV$]$. Again we find that all curves for $w > 2$ agree well with one-another.

In order to demonstrate the efficiency of this method we compare the computation time of the transmission curves shown in Fig 2. With a resolution of $\Delta E = 10$ meV the transmission of the system divided into 1, ..., 18 layers required 1368, 594, 429, 336, and 294 seconds, respectively. Using this approximation, e. g. with 6 principal layers, that takes 31% of the time of the „full-device" calculation, while increasing only a neglectable loss of accuracy.
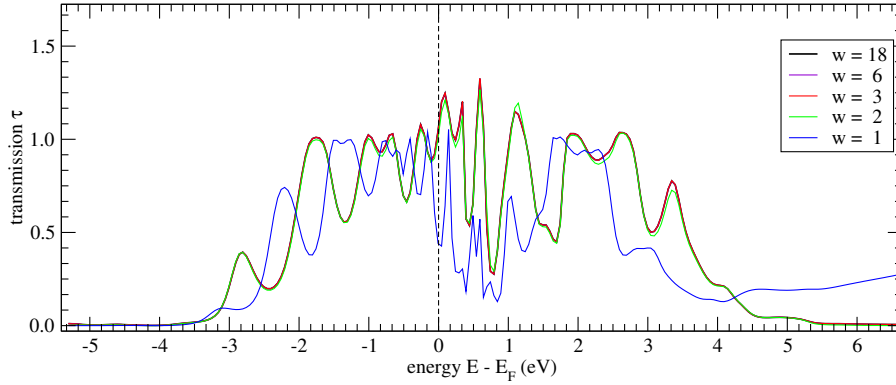
Figure 2.12: *The total transmission $\tau(E)$ of the model silver junction shown in Fig 1a, in the different levels of approximation, i.e. a changing number of „principal layers". Convergence with respect to the principal layer thickness is achieved as soon as w becomes is larger than 2.*

3 Structure and conductance in silver point contacts

3.1 Idealized silver electrodes

Due to their interesting physical properties and potential technological perspectives, metallic quantum wires and atomic-scale contacts are an object of intensive experimental [86–94] and theoretical investigations [72,82,95,96]. As the size of these constrictions is smaller than the scattering length of the conduction electrons, transport through such contacts is ballistic, and as the width of the contacts is on the length scale of the electron wavelength, the quantum nature of the electrons is directly observable. The electrical conductance of such quantum structures is given by the previously introduced Landauer formula $G = G_0 \Sigma \tau_n(E_F)$, where $G_0 = 2e^2/h$ is the conductance quantum. τ_n gives the transmission probability of the n-th channel and depends crucially on the orbital structure of the conducting atoms [88] and also on the atomic structure, in particular on scattering at defects and boundaries [95], as well as internal stress [72].

In practice, most conductance measurements of point contacts, even for simple metals, yield non-integer multiples of the conductance quantum G_0. Such deviations from the ideal behavior can stem from material-specific properties of the junction or from defects that result from the fabrication process. Especially in experiments based on atomic-scale contact fabrication by mechanical deformation (e.g., break junctions or scanning tunneling microscopy setups [86–88]), there is very limited control of the growth and properties of the atomic-scale contacts. In these experiments long-term stable and defect-free contacts with conductance at integer multiples of the conductance quantum G_0 are difficult to realize in practice as the fabrication process is essentially connected with the formation of atomic-scale defects such as dislocations.

To produce well-ordered contacts, a technique of nearly defect-free growth by slow quasi-equilibrium deposition is required, which can be provided by electrochemical deposition methods [89–93]. In addition, techniques of electrochemical annealing provide the possibility of healing atomic-scale defects in contacts even after fabrication (see below). Due to its high electrochemical exchange current density [97], silver is a promising candidate for efficiently applying electrochemical annealing techniques. Here we investigate the coherent transport of electrochemically deposited and annealed silver quantum point contacts that yield nearly ideal integer multiples of G_0 and explain their properties by comparison with conductance calculations for selected near crystalline junction geometries with a preselected number of contact atoms.

In this chapter we present calculations for various idealized silver nanojunction geometries of integer quantum conductance an analyze the correlation between structure (and

minimum cross section) and transmission function. Secondly we investigate the influence of distortion on the conductance by varying geometrical parameters. We then extend the study of the disorder influence by a statistical analysis of the conductance of silver junctions with randomly distributed surface vacancies similar to a dissoluting nanowire in electrolyte. Finally we examine the transmission functions of silver nano-particles contacted with an metallic electrode tip (similar to STM transport measurements). This system is interesting because small metallic nano-particles are from a structural point of view an intermediate case between an ideal fcc-lattice and a disordered system - they have a specific geometric structure with symmetries strongly depending on the number of atoms, which might influence the electronic transmission.

3.1.1 Model point contacts

In order to test the implementation of the previously described transport formalism and to get insights into the possible structures of metallic point contacts, permitting a conductance of an integer multiple of G_0, we calculated the coherent conductance of ideal crystalline silver nanojunctions (see Fig. 3.1). The geometries were generated by assuming two fcc electrode clusters, which are connected at their tips by a small number of Ag-Ag-bridges in the crystallographic [111] direction with a Ag-Ag nearest neighbour distance of 2.88 Å.

The zero-bias quantum conductance of a given junction geometry was computed with the Landauer formula (2.57). The electronic structure was described using an extended Hückel model [40, 42] including s-, p- and d-orbitals for each silver atom (around 3600 orbitals per junction). To take the influence of the semi-infinite leads into account, we employed the decimation technique (see chapter 2) to calculate the material-specific surface Green's functions [13] using the same type of model Hamiltonian and parameter set for the electronic structure as already used for the central device region. To reduce the influence of interference effects, we averaged the transmission $T(E)$ over a small interval $[E_F - \Delta, E_F + \Delta]$ around the Fermi energy (with $\Delta = 50$ meV), which is comparable to the temperature smearing in measurements at room-temperature.

As indicated in Fig. 3.1, we find nearly integer conductance of the idealized geometries for contact geometries 1-5: 0.97 G_0, 1.95 G_0, 2.89 G_0, 3.95 G_0, 4.91 G_0, respectively, with deviations from integer multiples of G_0 of about 0.1 G_0 which is in the range of the accuracy of our numerical method. We observe a correlation between the number of silver atoms at the point of minimal cross section, which aids in the construction of geometries with a particular value of the conductance. This proportionality „conductance $G \sim G_0 \cdot N$ number of atoms in the minimal cross section" may result from to the electron configuration of silver [Kr] $4d^{10}$ $5s^1$. The s-band dominates the local density of states [98] of silver at the Fermi edge, permitting one open transmission channel per Ag-atom. So this is a material specific property of silver unlikely to be encountered in other materials. It appears to hold only for a small number N of atoms in the minimal cross section, because it was shown in Landauer's scattering theory that the total transmission of a microscopic junction is given by the number of transversal modes, which depends primarily on the diameter of the junction.

Figure 3.2 shows the calculated total transmission as a function of the electron energy

within the energy interval $[E_F - 6eV, E_F + 6eV]$ for the five silver point contact geometries (1-5) given in Fig. 3.1. The conductance that is experimentally relevant corresponds to the transmission at the Fermi energy indicated by the vertical line in the figure. The transmission curve oscillations are sensitive to the atomic positions. Therefore, an average of the transmission around the Fermi energy yields a more representative value of the conductance G, taking effectively into account the atomic vibrations during the measurement.

In order to study to which extent the conductance values change due to geometrical changes in the interatomic distance of the contacting atoms and the relative angle between the contacting crystals, we introduced finite changes in contact geometry: We calculated the electrode distance and twist-angle dependence of the zero bias conductance. Increasing the electrode distance to twice the Ag-Ag bond length leads to a decrease by 86.7 % in the conductance, while twisting the electrodes by 60° against each other leads to a decrease of conductance of 22 % .

The results show that for silver, as a representative of a simple s-type metal, if defects and disorder in the contact area are avoided, the conductance in atomic-scale point contacts typically is an integer multiple of the conductance quantum G_0, for a small number N of atoms in the minimal cross section. On the other hand, if strong deviations from the crystallographic symmetry are induced, non-integer multiples of the conductance quantum are observed, which can be attributed to scattering due to defects and disorder within the contact area. These calculations are confirmed by measurements based on the method of combined electrochemical deposition and electrochemical annealing of point contacts, which yield integer multiples of the conductance quantum in ideal model geometries of contacting silver nanocrystals. As soon as annealing is omitted, drastic deviations from integer quantum conductance are obtained [99].
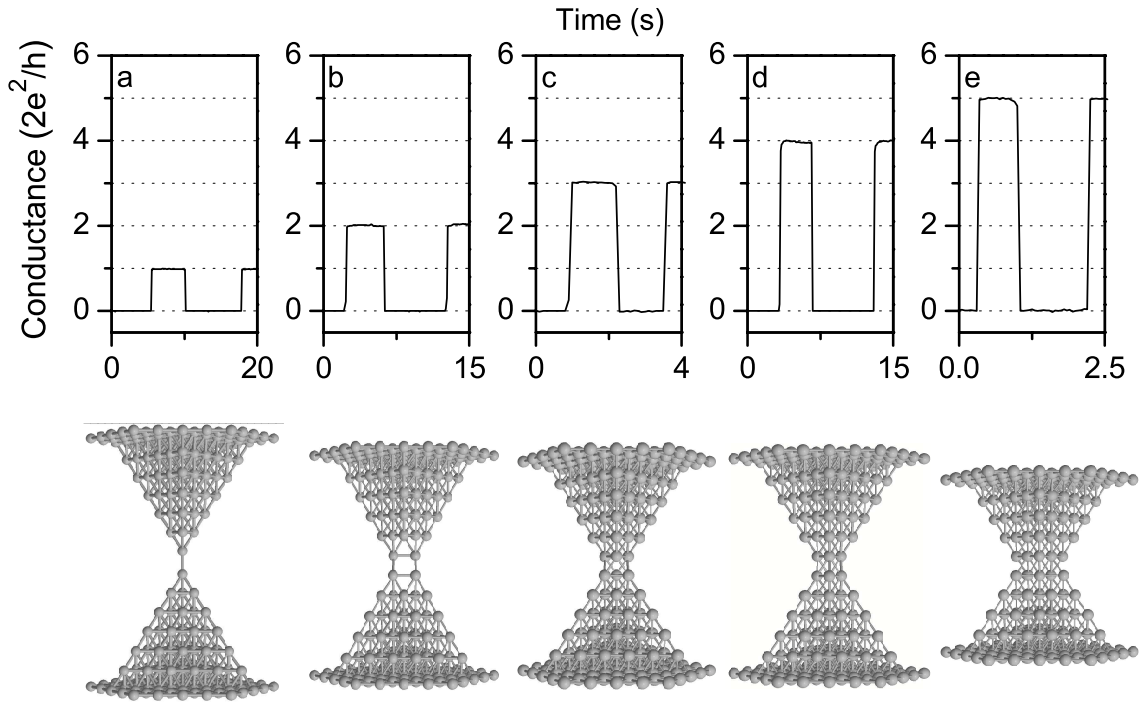
Figure 3.1: *Comparison of experimental conductance data of electrochemically annealed silver point contacts with calculations assuming idealized geometries. (a) Quantum conductance of five different annealed atomic-scale contacts at $1G_0$, $2G_0$, $3G_0$, $4G_0$, and $5G_0$, respectively (with $1G_0 = 2e^2/h$), which were reversibly opened and closed. (b) Idealized geometries of silver point contacts with predefined numbers of contacting atoms. Conductance calculations performed within a Landauer approach result in near-integer multiples of G_0 for each of the five contact geometries (1-5). For the conformations shown above, the axis of symmetry of the junction corresponds to the crystallographic [111] direction.*
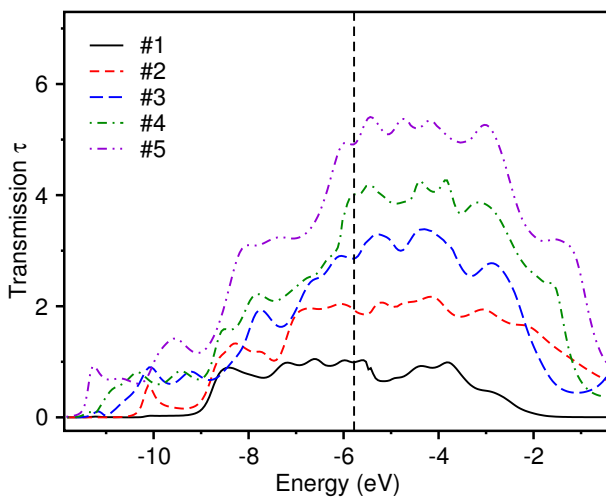
Figure 3.2: *Calculations of the transmission as a function of the electron energy for the five different silver contacts (1-5) of Fig. 3.1. The experimentally relevant values correspond to the conductance at the Fermi energy indicated by the vertical line in the figure.*

3.1.2 Conductance of deformed silver electrodes

The previously investigated silver nano-junctions are artificial in a sense that we have considered idealized metal cluster geometries of fcc lattice structure and highly symmetric electrode tip conformations. In a realistic experimental situation, in particular at room temperature, such assumptions are unlikely to be met, because in break-junction experiments as well as in STM arrangements there is always a non-vanishing tilt and twinning angle between the contacting electrodes also affecting the coherent scattering of electrons tunneling through the junction. In order to investigate the influence of such kind of disorder compared to the previously studied idealized conformations we have varied different structural parameters starting from a contact with fcc lattice symmetry and calculated the resulting conductance.
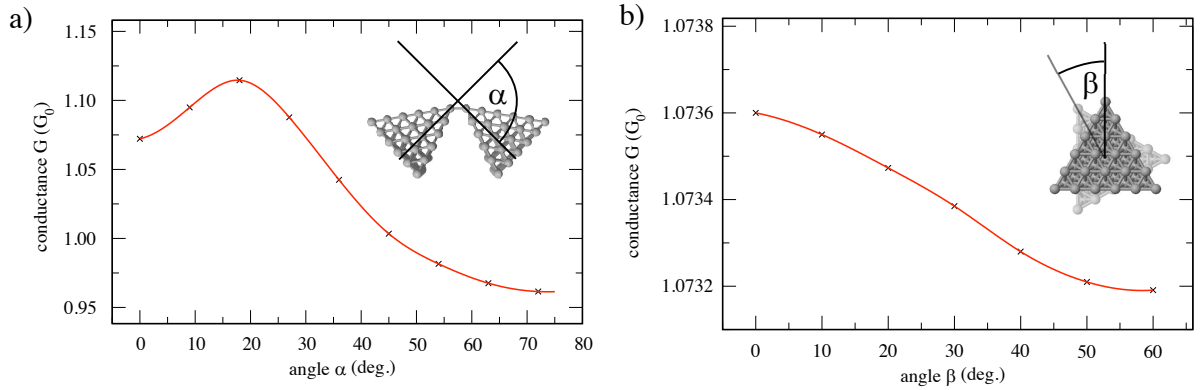
Figure 3.3: *The tilt- and twinning-angle dependence of the conductance of a silver point contact. (a) Only a moderate change of $\langle G \rangle$ is observed during tilting the electrodes up to 70 degrees. (b) The twinning of the electrodes between 0 and 60 degrees results in a nearly constant conductance.*

There are two obvious parameters which define the junction geometry with respect to the electrodes that are presently not under experimental control: The tilt and twinning angles of the two electrode fragments with respect to one another. In order to investigate the dependence of the conductance on these parameters, we have prepared an ideal fcc-silver junction with 224 atoms, as conformation 1 in the previous section, and varied the tilt angle $\alpha = 0, ..., 70$ deg. and twinning angle $\beta = 0, ..., 60$ deg., as shown in the insets of Fig. 3.3. Now we increase stepwise the angles α and β and calculate the zero-bias conductance for the obtained contact conformation using the tight-binding-like method and the Landauer formula.

Increasing the tilt-angle α from 0 to 20 degrees leads to a slight increase of the conductance by circa 0.05 G_0 which can be explained by the influence of interference effects, which strongly depend on small changes of the atomic positions. A further increase of α from 20 to 70 degrees results in a decreasing conductance by 0.15 G_0, which corresponds to the loss of crystal symmetry across the junction. An additional anisotropic effect might result from an changing overlap of d-orbitals. In contrast, twinning the electrode from 0 to 60 degrees leads only to a minor change in the conductance of $4 \cdot 10^{-4}$ G_0, which is

below the accuracy of the method. That means that twinning the contact conformation around a single Ag-Ag bond leaves the conductance nearly constant.

3.2 Conductance of silver electrodes with vacancies

When an electrode is manufactured in a break junction or generated by contacting the tip of an AFM/STM, it is also very unlikely that the perfect lattice geometries with perfect surfaces along the crystalline axis, assumed in nearly all theoretical investigations, are realized in practice. According to all models of electronic transport, each surface defect creates an additional scattering center that may impede coherent ballistic transport through the junction. Imperfections in the geometry of the electrode tips will thus influence the ballistic transport. On the other hand, we have seen in the previous section, in agreement with many prior studies [40,41,82,83], that the conductance of the junction is mostly determined by its most narrow region [99].

In order to estimate the significance of tip disorder we have therefore prepared a perfect junction as above and then randomly removed atoms from the surface of the electrode in the vicinity of the contact point. The number of silver atoms in the extended molecule region is systematically decreased by removing 28 atoms at randomly chosen surface positions. To maintain coherent transport, the two central atoms were never removed. Every junction geometry with $n \cdot 28$ vacancies ($n = 1, ..., 5$) was generated 500 times, with randomly chosen vacancy positions. For each conformation we computed and subsequently averaged the conductance. In order to increase the efficiency of the conductance calculations we employed the recursive Green's function algorithm (see chapter 2.4) with a principal layer thickness parameter $w = 3$.

Samples of the resulting junction conformations are shown in Fig. 3.4 (*left*) with the corresponding averaged conductance value in units of G_0, respectively. In addition, the total number of surface vacancies on the current junction geometry is given below the conductance values. At a number of vacancies below 28 the zero-bias conductance is close the ideal value of a perfect Ag dimer junction of $1.0G_0$. The systematically increasing amount of surface vacancies leads to a decreasing conductance in steps of $\approx 0.1G_0$.

Figure 3.4 (*right*) shows the sloping of the conductance values averaged over conformations with equal number of surface impurities. Creating 140 vacancies, which is half of the initial number of atoms, reduces the total conductance by 40% in average. The rapidly increasing size of the error-bars indicates that the change in the conductance depends strongly on their positions.
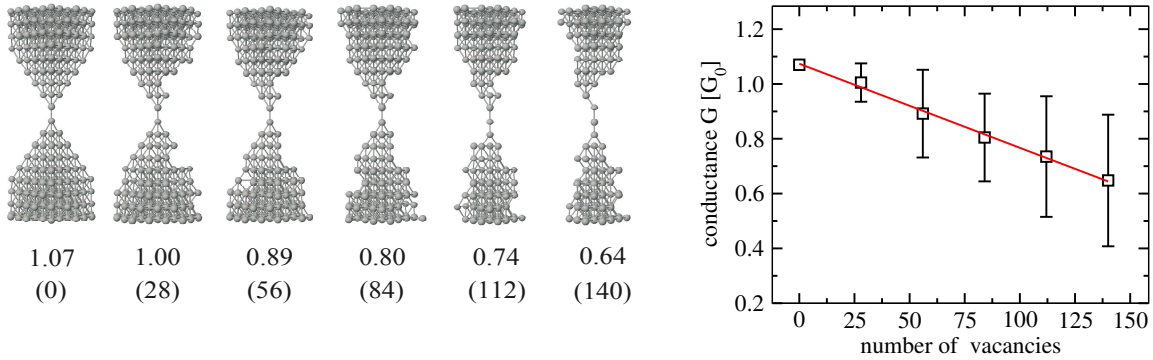
Figure 3.4: *(left) Representative examples of the generated conformations of silver nanojunction with an increasing number of surface vacancies. The presence of defects leads to a decrease of the conductance by up to 30%, indicated by the corresponding conductance values below the geometries. The number of vacancies in conformation is given in brackets. (right) Conductance values averaged over conformations with equal number of surface impurities. The error-bars indicates that the change in the conductance depends less on the number of defects, but more on their positions.*

3.3 Silver nanoclusters

Recent experiments of silver junctions [92,99] suggest a strong stability of the observed zero-bias conductance in electrochemically grown silver junctions. While this effect was locally explained [100] by the selection of specific contact geometries, the overall shape of the silver contacts is likely to vary strongly from one realization of the next. To assess the effect of these large-scale geometric differences, we have prepared locally similar, but globally different junction geometries by placing silver clusters of various size in different orientations on a perfect surface and then contacting the tip of the cluster with an „ideal" junction. For this purpose we use the optimized cluster geometries from Ref. [1, 101], which where generated by Monte Carlo minimization and the modified dynamic lattice search method. Figure 3.5a shows the top view of the studied silver clusters with 5, 7, 180, 220, and 260 atoms and decahedron (*m*-Dh) core symmetry [102]. Such kind of clusters consist of two pentagonal pyramids sharing a common basis and a fivefold axis. They are formed by five tetrahedra sharing a common edge along the fivefold axis. When five regular tetrahedra are packed, gaps remain, which are filled by distorting the tetrahedra, thus introducing some strain, which might also effect the coherent transport properties in such a metallic cluster. As illustrated in Fig. 3.5b we consider the metal clusters attached to a silver substrate layer of the crystallographic [111] direction. The second electrode is realized by a pyramidal tip on top of the nano-cluster similar to a STM-setup.

We optimized the position of the silver nano-cluster on the substrate using a Metropolis Monte-Carlo technique combined with the semi-empirical Gupta potential for the silver atoms as described above. During the simulation the silver cluster is treated as a rigid body, so only translations and rotations of the cluster are allowed - structural rearrangements insight the cluster are forbidden. The metal cluster surface consists of a set of

[111], [110] and [100] facets. The minimum of the potential energy is reached, if the system is arranged such that the largest [111] facet (which is always the largest subsurface in the present cases) and the [111] substrate layer are facing each other. The top electrode is assumed to point directly on one arbitrarily chosen silver atom on the cluster surface.

Figure 3.5c shows the total transmission function of the clusters Ag_5, ... ,Ag_{260}. The conductance of the systems is given by the average of the transmission over a small interval around the Fermi energy $[E_f - \Delta, E_f + \Delta]$ with $\Delta = 50$ meV. For the clusters with 5, 7, 180, 220, and 260 atoms we find conductance values of 1.10, 1.08, 1.15, 1.17, and 1.17 G_0, respectively, which means, that the conductance is less effected by the size of the nano-cluster and depends more on the point contact to the second electrode. This observation may explain the observed stability of the experiment: While reconstruction of the junction geometry assures the selection of a specific local geometry, the overall conductance depends only very little on the global shape of the clusters forming the contact.
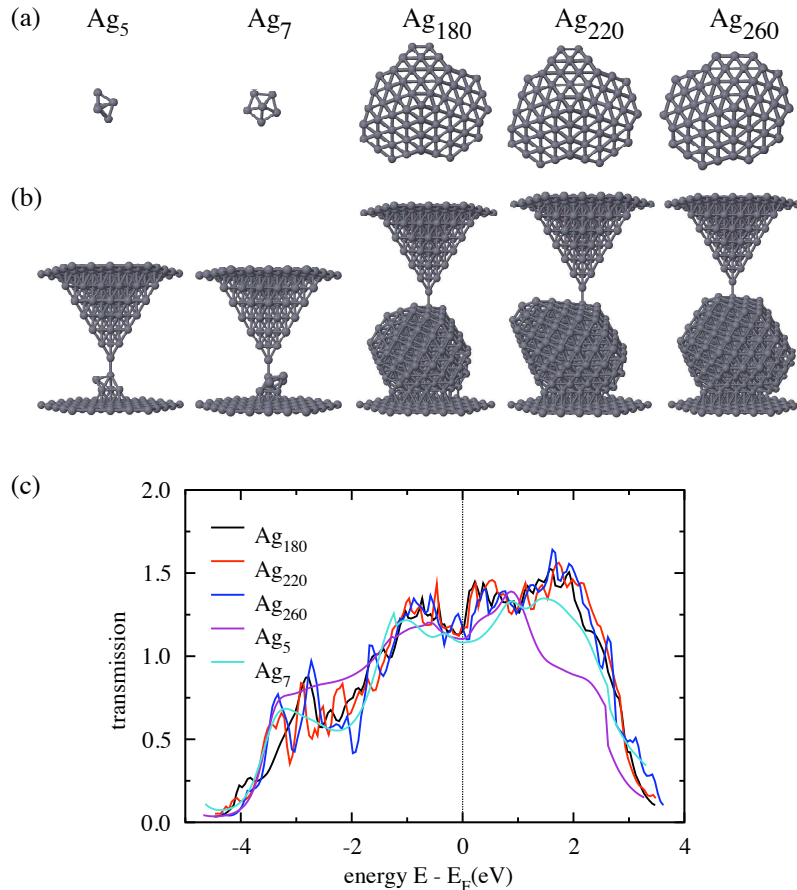
Figure 3.5: *Transmission of silver nano-clusters. (a) Shows the top view on the examined nano-cluster conformations with 5, 7, 180, 220, and 260 atoms. (b) Cluster conformations energetically optimized on a silver substrate layer with a pyramidal electrode on top. (c) Calculated transmission function of the junction conformations shown in b. The vertical line indicates the Fermi energy.*

We also note that an irregular fluctuation of the transmission as a function of energy, which increases with the cluster size. Such fluctuations can be conceptually explained by the interference of the incident electron waves with waves scattered repeatedly in the extended molecule region containing the sliver nano-cluster and the electrode tip. An analysis of the average energy spacing of the extrema of the transmission (which may be measured by applying a gate voltage) can help to estimate the size of the backscattering region.

3.3.1 Conclusions

To conclude, the first results of the ballistic transport calculation of crystal symmetric silver nanojunctions, using a recursive layer Green's function approach, demonstrate that for silver as a representative of a simple s-type metal, if defects and disorder in the contact area are avoided, the conductance is an integer multiple of the conductance quantum G_0 (at least for small diameters of the contact region).

These results where confirmed by experiments of combined electrochemical deposition and electrochemical annealing of point contacts, which have proven to be a very efficient technique to generate such well-ordered contacts. On the other hand, if annealing is omitted, non-integer multiples of the conductance quantum are observed, which can be attributed to scattering due to defects and disorder within the contact area. As soon as disorder or local distortions of the atomic lattice within the contact area are introduced in the model geometry, drastic deviations from integer quantum conductance are obtained. Most experimental realizations of nanoscale junctions will contain some degree of structural disorder, which is difficult to assess in situ experimentally.

As idealized electrode conformations are unlikely obtained in several other fabrication techniques we also investigated the influence of imperfect contact geometries on the conductance by studying many different possible realizations of silver. Using a fcc-lattice symmetric silver electrode contact as starting point we varied two characteristic structural parameters of the junction. Tilting the junction electrodes up to 60 degrees reduces the conductance by 20%, while twinning the electrodes leaves the conductance nearly unchanged. We found that the introduction of up to 50% surface vacancies leads to only small variates of the ballistic transport properties of silver contacts, as long as the immediate vicinity narrowest point of the junction was not affected. This analysis was supported by a study of the effects of global conformational change in silver junctions for locally conserved junction geometries. Here we find that variations in the global cluster geometry ranging from 5-260 atoms have only a weak effect on the zero-bias conduction of junctions with locally conserved geometry. The obtained conductaces of silver nanoclusters confirm the results of the transport properties of idealized fcc contact geometries, where we already found a strong dependence of the total conductance on the diameter of the minimal cross section.

4 Simulation of the atomic transistor

Controlling the electronic conductivity on the quantum level will impact the development of future nanoscale electronic circuits with ultralow power consumption. Fascinating physical properties and technological perspectives have motivated intense theoretical and experimental investigation of atomic-scale metallic point contacts in recent years [86, 88, 93, 99, 103–108]. The quantum nature of the electron is directly observable, because the width of the contacts is comparable to the electron wavelength and conductance is quantized in multiples of $2e^2/h$ in ideal junctions. In real metallic point contacts, which have been fabricated by mechanically controlled deformation of thin metallic junctions [82, 103, 109, 110] and electrochemical fabrication techniques [107], the conductance depends on the chemical valence [88]. Two-terminal conductance-switching devices based on quantum point contacts were developed with an STM-like setup [104] and electrochemical methods [105]. Recently, quantized magnetoresistance in atomic-size contacts was switched between two quantized conductance levels by rotating the point contacts in a magnetic field [106].

The investigations of the present chapter were motivated by an earlier experimental study (Ref. [92]), which reports on the fabrication and operation of the first single atom transistor, a three-terminal device based on the bistable movement of a small group of bridging silver atoms, switching a current between integer values of the conductance quantum.

After a brief introduction into the experimental conditions we will describe a multi-scale approach to model the structure, dynamics and electronic transport properties of the atomic transistor. With the help of the simulations we will discuss the underlying tip reconstruction process and explain several effects observed in the conductance measurements like the long-time stability of the repeated switching and intermediate levels at non-integer conductance. Special attention is given to the influence of the electrolyte on the electrode deposition and switching process - we describe the extension of our approach by a continuum model of the solvent and discuss the results of the simulation results.

4.1 Experimental Motivation

Reference [92] reports on the developed of a three-terminal gate-controlled atomic quantum switch with a silver quantum point contact in an electrochemical cell, working as an atomic-scale relay. It is based on the control of individual atoms in a quantum point contact by an independent gate electrode, which allows for a reproducible switching of

the contact between a quantized conducting on-state and an insulating off-state. The device operates stable for long sequences of electrochemically controlled switching between the nonconducting off-state and the quantized conducting on-state, where the quantum conductance of the switch follows the gate potential, as commonly observed in transistors. Figure 4.1a shows the experimental setup: Two gold electrodes (thickness approximately 100 nm) serve as electrochemical working electrodes and are covered with an insulating polymer coating except for the immediate contact area. A silver wire of 0.25 mm diameter was used for the counterelectrode and the quasi-reference electrode. The electrolyte solution consists of 1mM $AgNO_3$ + 0.1 M HNO_3 in bi-distilled water. The bias voltage between the two gold electrodes for the conductance measurements was kept at 12.9 V. The change of the electrochemical potential difference between the reference electrode and the gold working electrodes was performed by varying the control potential. The electrochemical potential of 10-40 mV between the reference electrode and the two gold electrodes permits the formation of silver islands on the two gold electrodes which finally meet each other by forming an atomic-scale contact. If such a contact is formed, the following procedure was performed in order to configure an atomic-scale switch. After an upper threshold (0.94 G_0 in case of a „1 G_0-switch") near the desired conductance value for the on state is exceeded, deposition is stopped and a computer controlled electrochemical cycling process starts, that applies a dissolution potential until the conductance drops below a lower threshold (0.05 G_0). Now the deposition starts once more until the conductance exceeds the upper threshold and so on. At the first such dissolution-deposition cycles of each fresh formed contact, conductance values still vary from cycle to cycle. After repeated cycling an abrupt change is observed from this irregular variation of the conductance values to a controlled and reproducible gate-voltage induced switching between two levels. Single atom switches fabricated by this technique operate stable over thousands of switching cycles at room temperature for switching between 0-1G_0 up to switching between 0-20G_0 - examples of the gate-voltage induced conductance switching are show in figure 4.1b and c for switching between 0 and 1 G_0 and switching between 0 and 18 G_0, respectively.

When the gate potential is set to an intermediate hold level between the on and the off potentials, the currently existing state of the atomic switch remains stable, and no further switching takes place. This is demonstrated in figure 4.1d both for the on-state of the switch (left arrow) and for the off-state of the switch (right arrow). Thus, the switch can be reproducibly operated by the use of three values induced by the gate potential for switching on, switching off, and hold. This provides the basis for atomic-scale logical gates and atomic-scale digital electronics.

Nevertheless, to understand and optimize this promising experimental method, it is necessary to investigate certain questions regarding the underlying structural and electronic properties of the employed silver nano-junctions. For switching in the range of low conductances (below 5 G_0) it seems to be possible, that the switching mechanism is based on the reproducible rearrangement of a small silver cluster, consisting only of a few atoms (≤ 13), between the left an the right contact. The fact that the experiment succeeded also for switching between up to 0 and 20 G_0 suggests an other explanation of the underlying mechanism, because the gate-potential induced energy would not be sufficient to rearrange a single silver cluster that would allow for switching between 0 and 20 G_0.
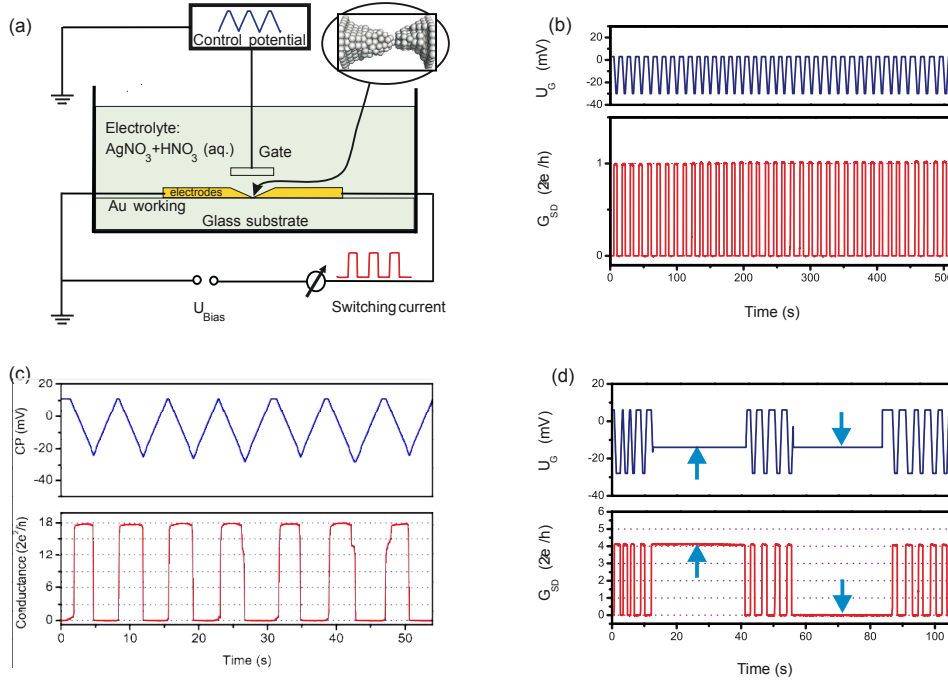
Figure 4.1: *Switching current by electrochemical, gate-controlled atomic movement. (a) Schematic of the experimental setup: A silver point contact is deposited electrochemically in a narrow gap between two gold electrodes on a glass substrate. Repeated computer-controlled electrochemical cycling permits fabrication of bistable atomic-scale quantum conductance switches. (b) Experimental realization of switching current reproducibly with a single silver atom point contact between a conducting on-state at $1G_0(1G_0 = 2e^2/h)$ and a non-conducting off-state. The source-drain conductance (G_{SD}) of the atomic switch (lower diagram) is directly controlled by the gate potential (U_G) (upper diagram). (c) Similar demonstration an atomic transistor conformation permitting bistable switching between 0 and $18G_0$ (d) Demonstration of quantum conductance switching between a non-conducting „off-state" and a preselected quantized „on-state" at $4G_0$. A conductance level can be kept stable, if U_G is kept at a „hold" level (see arrows).*

4.2 Atomistic model of the quantum switch

While we can understand the conductance properties of such junctions on the basis of atomistic conductance calculations [99], the physical process underlying the switching mechanism remained unclear. Reproducible switching between quantum conductance levels over many cycles cannot be explained by conventional atom-by-atom deposition but requires a collective switching mechanism. Our previous calculations have shown that only well-ordered junction geometries result in integer multiples of the conductance quantum. Neither partial dissolution of the junction nor its controlled rupture yields the necessary atomic-scale memory effect. A more detailed model of the structural [82, 109, 111] and conductance [88, 112] properties of such junctions is therefore required. In order to clarify the open questions regarding the switching mechanism of the atomic

transistor and to examine several effects occurring in the measured conductance curves we have developed a multi-scale algorithm containing a quantum mechanical treatment of the electronic structure to calculate transport properties, a classical force field method based Monte Carlo treatment of the atomic structure and a continuum model to take electrostatics into account.

We assume a simulation box with an edge length of $24.0 \times 24.0 \times 40.0$ Å^3 in x-, y- and z-direction, respectively. As start conformation for the simulation of the deposition process we consider two hexagonal silver layers in crystallographic (111) direction consisting of 144 atoms with a nearest neighbor distance of 2.88 Å. To increase the growth probability towards each other we assume additional silver tips at the planes consisting of 10 atoms on each layer.

Starting from the previous system we simulate the deposition process in the following way: At each electrode deposition cycle we insert one silver ion at a random position between the left and right silver cluster. Afterwards a relaxation of the ion position into a local energy minimum on the electrodes takes place. For the electrochemical deposition we use a simulated annealing routine that is based on a classical Metropolis Monte-Carlo algorithm [31]. It was already successfully applied to the simulation of the growth process of thin amorphous films [113]. One simulated annealing cycle consists of a high number of trail steps into a random direction (and object rotations of random axis and angle, is case of deposition of extended molecules). A trial step moving the ion from the position $\mathbf{r}$ to $\mathbf{r}'$ is accepted within the Metropolis probability criterion

$$P(\mathbf{r}, \mathbf{r}') := \begin{cases} \exp(-\beta \left[E(\mathbf{r}) - E(\mathbf{r}') \right]), & \text{if } E(\mathbf{r}) < E(\mathbf{r}') \\ 1, & \text{else} \end{cases} . \tag{4.1}$$

In the present simulation we use four simulated annealing cycles per ion deposition, with each cycle consisting of 15000 steps. The temperature T, which plays the role of a parameter in arbitrary units, reaches from 250 at the beginning to 0.001 at the end of the annealing process.

The total energy plays the central role in this algorithm. In the first period of the ion deposition, in the unbounded situation, the ion is exposed to the coulomb potential governed by the surrounding source/drain electrodes which are set to -34 meV and -46 meV, respectively. To include their influence and to treat the electrostatic field we use a finite differences scheme [114], i.e., we introduce a lattice with 1.0 Å mesh spacing and occupy every mesh point with the potential -34 meV (-46 meV) if the mesh point is surrounded by at least one Ag atom of the left (right) electrode. So we can use the given potential distribution in the electrodes as Dirichlet boundary conditions (in z-direction) for the Poisson problem to calculate the potential between the contacts. In x- and y- we use periodic boundary conditions and after solving Poisson's equation for the electrostatic potential $\phi(\mathbf{r})$ the energy of the ion in this field is given by $E(\mathbf{r}) = q \cdot \phi(\mathbf{r})$, with q being the charge of the Ag$^+$ ion. As soon as the silver ion attaches the left or the right electrode, the potential energy surface is described by the empirical Gupta potential [115], which accounts for the interactions among the atoms in the cluster. It is based on the second moment approximation of the electron density of states in the tight-binding theory and can be parametrised as follows:

$$E_{\text{Gupta}}(\mathbf{r}) = \frac{U_N}{2} \sum_{i=1}^{N} \left(A \sum_{j \neq i}^{N} e^{-p\tilde{r}_{ij}} - \sqrt{\sum_{j \neq i}^{N} e^{-2q\tilde{r}_{ij}}} \right) \quad \text{with} \quad \tilde{r}_{ij} = \frac{|\mathbf{r}_i - \mathbf{r}_j|}{r_0} - 1. \quad (4.2)$$

According to Ref. [115] the parameters $\{U_N, A, p, q, r_0\}$ were chosen as { 1, 0.09944, 10.12, 3.37, 2.88 }. The first term in equation (4.2) represents a pairwise Born-Mayer repulsion energy and the second models a N-body attractive contribution. For an efficient evaluation of the potential we save adjacent atoms in linked lists and apply the linked cell algorithm [30] with a cutoff radius of $4.0a$ ($a = 2.88$Å).

In order to speed up the calculation we keep all atomic positions of the silver clusters fixed, if a new silver ion enters the simulation box and treat the potential given by the cluster atoms as external field for the ion. An additional reduction of computational costs is achieved by storing all cluster atoms on a grid. Here we us a grid spacing of 10 Å. Every grid point is related to a linked list of objects containing the information of the atomic position, charge and pointers to the neighboring list elements. To evaluate the total energy now only these cluster atoms are taken into account which belong to grid points in the direct surrounding of the added silver ion (often called *Linked-Cell-approximation* in literature [30]).

The ion deposition cycle is repeated until a predefined number n of paths from the left to the right electrode exists (see fig. 4.2a, upper row). Otherwise the current electrode conformer is used again as start geometry, where all atomic coordinates are fixed and another Ag$^+$-ion is brought into the simulation box. We deposit up to 800 atoms in the junction until a predefined number of non-overlapping pathways connect the left and right electrode. As a non-overlapping pathway, we define a unique set of touching atoms that extend from one electrode to the other, which permits us to identify the minimal cross-section of the junction.

Next, we simulate the switching process (see fig. 4.2a, lower row): The change in the electrochemical potential induces a change in the interface tension of the liquid-metal interface, making possible a deformation of the junction geometry parallel to the junction axis. It is well-known that changes in the electrochemical potential modulate the interfacial tension of the whole electrode [116–118], which results in a mechanical strain on the junction. We simulate the opening/closing cycle of a junction by evolving the atoms of a central cluster under the influence of the electrochemical pressure. During the opening/closing process the silver clusters are displaced in steps of 0.15 Å. For each cluster displacement we perform 10000 simulated annealing steps, where the temperature-parameter is reduced from 300 to 3 (arbit. units). We assume that only the atoms in this region move in the switching process, while most of the bulk material remains unchanged. The central cluster comprises the atoms of the minimal cross-section connecting the two electrodes and all atoms within a radius of 9.0 Å around this central bottleneck. While the electrodes gradually move apart/closer together, all atoms of the central cluster relax in simulated annealing simulations generating a quasi-adiabatic path between the open and the closed conformation. We probe the structural bi-stability by comparing the atomic positions of the conformer before and after one switch operation. If

$\Delta r_{\max} := \max\{|\mathbf{r}_i^{\text{before}} - \mathbf{r}_i^{\text{after}}|\}$ is smaller than $0.2a$ $(0.3a)$ for $n = 1, 2$ $(3, 4, 5)$ the conformer is saved as „structural bi-stable". This seems to be a rough approach, but we will see in the results section, that after several switching steps the structural bi-stability further increases. We assume a sphere around the first contact atom with the radius $r = 3.0\text{Å}$ and define all atoms outside of the sphere as fixed. To simulate one „on-off-on"-procedure of the switch, we move the fixed left (right) electrode atoms 3 Å to the left (right) in the case of $n = 1$. For $n = 2, 3, 4, 5$ we used larger displacements due to stronger structural rearrangements in the tip region. As described above, we define now the actual conformer as „structural bi-stable", if the deviation between the atomic positions before an after the switching step is small.

In the atomic switch experiment explained in [92] the bi-stability is observed in conductance values. Using the quantum transport method described in the previous chapter 2.4 (the recursive Green's function method), we select now these atomic switch conformers, that show bi-stable and integer quantum conductance. We calculate the conductance of a „structural bi-stable" conformation before and after one switching operation; is the deviation $\Delta G \leq 0.1 G_0$ and in the case of an integer conductance value $\approx m \cdot G_0$ $(m \in \mathbb{N})$ the conformer is accepted as bistable quantum switch structure.

Not surprisingly, the junction rips apart at some finite displacement from the equilibrium, an effect also seen in break-junction experiments. For most junctions, this process is accompanied by a surface reorganization on at least one, but often both, tips of the electrode(s). When we reverse the process, some junctions snap into the original atomistic conformation (see Figure 4.3b) with subatomic precision. At the end of the switching simulation, we compare the final and the starting geometry. If after the first switching
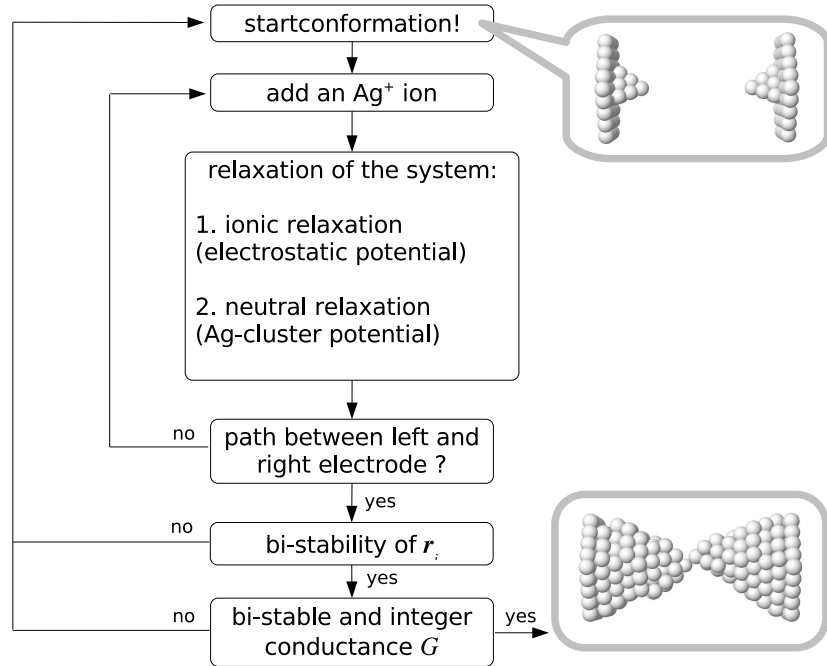
Figure 4.2: *Simplyfied flow chart of the simulation script including the electrode deposition, the bistability test and the conductance calculation.*
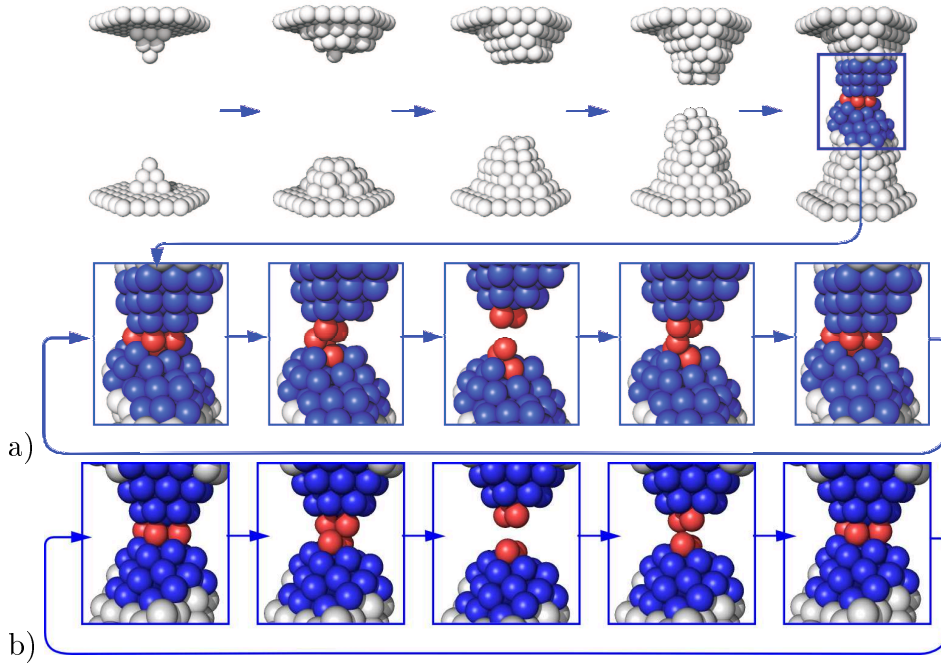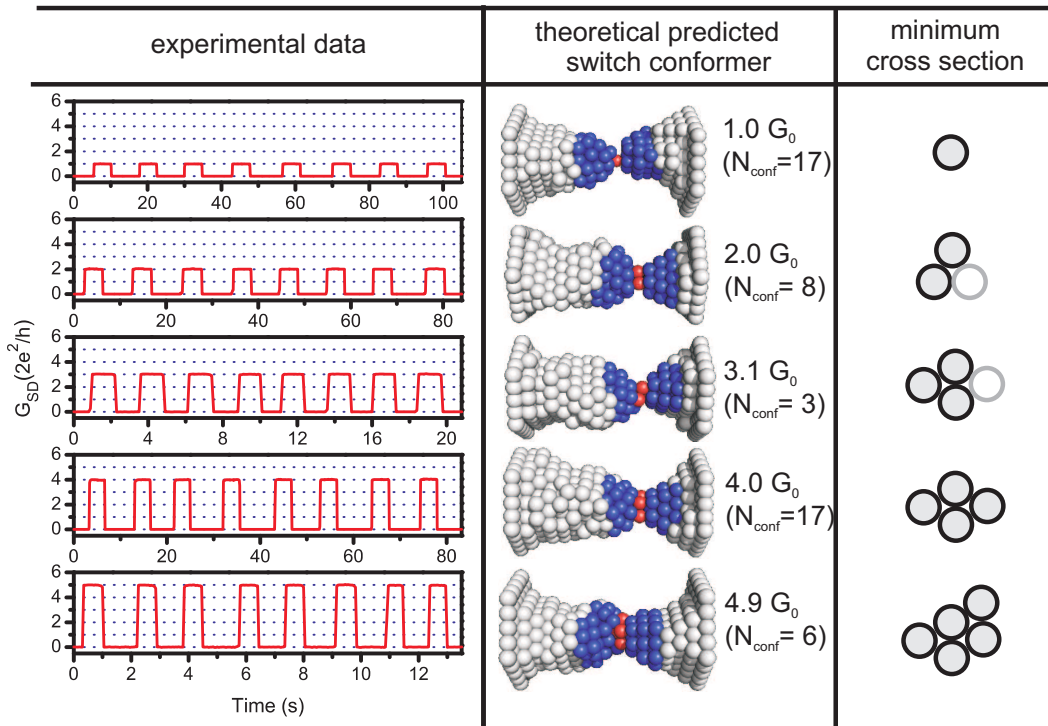
Figure 4.3: *Simulation of atomic point contact growth and switching process. (a) Snapshots of the deposition simulation. Upper row: The growth process starts with two disconnected Ag (111) layers and stops, when a non-overlapping pathway with a predefined number of silver atoms connects the electrodes. Lower row: Simulation of the switching process reveals a bistable tip-reconstruction process as the mechanism underlying the reproducible switching of the conductance. During the simulation, we kept the gray marked silver atoms at their positions at the end of the deposition and permitted the central cluster to evolve (blue and red atoms) under the influence of the electrochemical pressure. The central silver atoms (red) define the minimal cross-section (see Figure 4.4, right column). These atoms return with sub-Angstrom precision to their original positions at the end of the switching cycle. (b) Snapshots of the tip reconstruction of a 4 G_0 switch conformation. The red marked silver atoms form a bridging contact similar to two scissors pulled into each other.*

cycle the junction has returned to the same geometry, that means in the present case that all atoms return to their original positions to within 0.28 Å, we consider the junction switchable and perform further switching cycle simulations to test stability. Otherwise, we discard the junction completely and start from scratch.

We then compute the zero-bias conductance [71, 119, 120] of the entire junction using a material-specific, single particle Hamiltonian and realistic electrode Green's functions (see chapter 2.3.5). We use the recursive Greens function method [81, 121], which maps the problem of computing the full device Greens function to the calculation of principal layer Greens functions, which drastically reduces the computational effort but maintains the accuracy. The electronic structure is described using an extended Hückel model including s-, p-, and d-orbitals for each silver atom (7200 orbitals per junction) [122] in the standard minimal basis set of non-orthogonal Slater type orbitals. The extended

Hückel method was previously shown to give reasonable predictions [40, 41, 115, 123] for the conductance of metal nanowires (containing about 800 atoms) where DFT-like methods [109] would be prohibitively costly. We take the influence of the leads into account, by assuming a semi-infinite fcc lattice for the left and the right reservoir. We compute the material-specific surface Green's functions by applying a decimation technique that exploits the translational symmetry of the semi-infinite contacts [13].

In total we have performed 15280 full deposition simulations generating $N_{conf} = 17$, 8, 3, 17, and 6 junctions with $n = 1,..., 5$ conductance quanta, respectively. Most deposition simulations fail to generate a switchable junction, because the acceptance criterion for switchability was very strict. We note that the same holds true for most control simulations starting from the perfect conformations of [99], indicating that simple rupture of even nearly ideal junctions cannot be the basis of the switching mechanism. We find that the retained junction conformations (typically comprising 500-800 atoms) have a preselected integer multiple (n) of G_0 in close agreement with the experiment. Because these observations result from completely unbiased simulations of junction deposition and switching, they explain the observed reversible switching on the basis of the

Figure 4.4: *Relation between the structures of atomic point contacts and their conductance. (a) Quantum conductance switching between a nonconducting off-state and a preselected quantized on-state at $1G_0, 2G_0, 3G_0, 4G_0,$ and $5G_0$, respectively (note individual time axis). (b) Representative conformations of simulated junctions, computed zero-bias conduction, and number of junctions with the specified conductance. (c) Representative minimal cross-sections for each conductance level. The minimal cross-sections are characteristic for each group of the switch conformers and determine their quantized conductance.*

generation of bistable contact geometries during the deposition cycle. If we consider the tip-atoms at each side of the electrodes in the open junction, the equilibrium geometry of both clusters depends on their environment. In the open junction, this environment is defined by the remaining electrode atoms on one side, while in the closed junction, the tip-cluster of the other electrode is also present. The simulations demonstrate the existence of two stable geometries for each cluster in both environmental conditions, respectively. Reversible switching over many cycles is thus explained by reversible tip reorganization under the influence of the gate potential, similar to induced surface reorganization [124–126]. While the overall structure differs between junctions with the same conductance quantum from one realization to the next (see Figure 4.4, middle column, for representative examples), the minimal cross-section that determines the conductance is largely conserved (Figure 4.4, right column). The direct comparison of our atomistic, quantum conductance calculations, using the unaltered conformations from the deposition/switching simulations, with the experimental conductance measurements offers a strong validation of the geometries generated in our deposition protocol. The observed agreement between computed and measured conductance is impressive, because the conductance of metallic wires is well-known to be strongly dependent on the geometry.

Figure 4.5 shows the probability distribution to obtain a bistable 1 G_0, ..., 5 G_0 switch conformation at a deposition simulation as performed in this study. Every probability was calculated by the fraction of number deposition processes n_{trys} divided by the number of obtained bistable point contacts $n_{success}$. With increasing number of bridging atoms the number of atoms which are involved into the tip-reconstruction increases. If many atoms participate in the tip reconstruction it becomes likely that the bi-stable rearrangement fails at some point, so the probability to obtain an atomic transistor conformation switching between high conductance differences decreases exponentially.
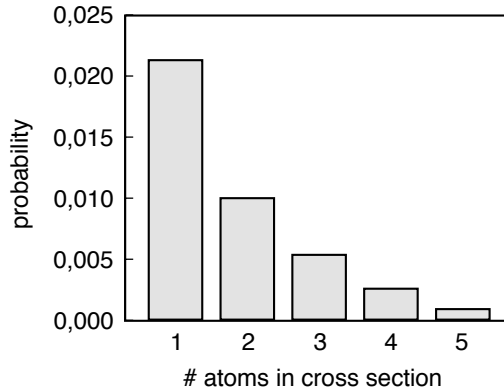
Figure 4.5: *Diagram of the exponentially decaying distribution of the propability to obtain an atomic transistor conformation allowing for bistable tip reconstruction with quantized conductance.*

4.3 Conductance during switching

During one opening/closing process in a bistable electrode configuration the electrode geometry allows for one and the same conductance value at the closed state of the
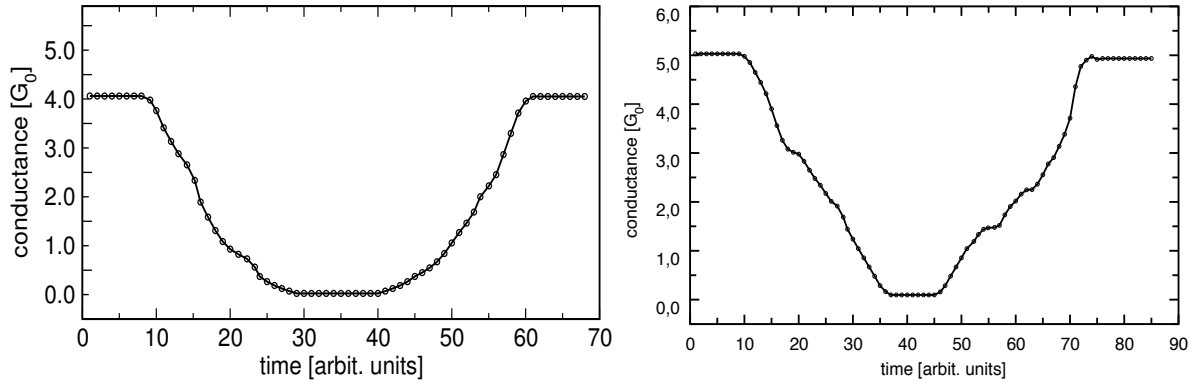
Figure 4.6: *Variation of the computed conductance of a 4 G_0 and a 5 G_0 switch during one open/close process. In agreement with the experimental observations, we find asymmetric plateaus in the conductance curve, if the switch is opened or closed. This can be traced back to the existence of several low-energy path ways connecting the open and closed state.*

nano-junction, however the atomic positions not necessarily pass the same path in the configuration space at rupture and at closing the contact. Slightly different trajectories in the configuration space would lead also to asymmetries in the time dependent conductance during one switching process. Experimental results of conductance curves at high time resolutions (1μs) indicate such an asymmetry effect, where the switching form „off" to „on" shows several intermediate conductance levels while switching the contact from „on" to „off" seems to occur instantaneously.

To examine whether this hysteresis like behavior can be traced back to the existence of several path ways in the configuration space connecting the „on" and the „off" state, we compute the conductance of a 4 G_0 and a 5 G_0 switch during one open/close process. Figure 4.6 shows the resulting conductance over step number, while the junction was pulled apart in steps of 0.15 Å. Opening the junction results in conductance plateaus close to 3.0 G_0 and 2.0 G_0 and closing the contact shows plateaus at 1.5 and 2.0 G_0. Particularly int the case of the 5 G_0 switch it is visible that the plateaus on the right hand side of the minimum are more distinctive then the plateaus on the left hand side.Since the atomic structure calculation proceeds in the adiabatic regime, the simulation shows that there are different trajectories in configuration space connecting the open and closed geometry of the silver nano-junction.

4.4 Snapping into conformation with integer quantum conductance

In the experiment bistable silver contact conformations are produced by a protocol that generates a junction that switches between 0 G_0 and a random (also non-integer) conductance value lower than 20 G_0 during the first switching cycles. After repeated cycling the contact snaps into a bistable geometry, allowing for switching between integer conductance values. In contrast the structure growth simulation starts from scratch, if the

contact of the junction yields a non-integer conductance value. In this section we will examine, whether the assumption of gate-potential induced electrode displacement, as underlying mechanism for the switching process, also allows for an explanation of the snapping of the electrodes from a conformation with non-integer to a conformation with integer conductance.

Here we employ a silver point contact with only one bridging silver atom but an initial conductance of $1.68G_0$. The additional contribution above the conductance quantum is caused by the orbital overlap of silver atoms in the surrounding of the red marked bridging atom, which is an entity of the particular junction conformation, visible in the leftmost inset of figure 4.7. In the following simulations we open the point contact by 3.0 Å in steps of 0.15 Å leading to nearly zero transmission. The electrode displacement induces now a tip rearrangement, where the bridging (red marked) silver atom takes an energetically more stable position exactly in between the left and right electrode tip (see third inset of figure 4.7). The inversion of the electrode displacement closes the contact again, which has now a more stable geometry at a conductance of 1.1 G_0. The conductance calculation over an additional switching process shows that the obtained electrode configuration reproduces its conductance in the closed state and so allows for bistable switching.
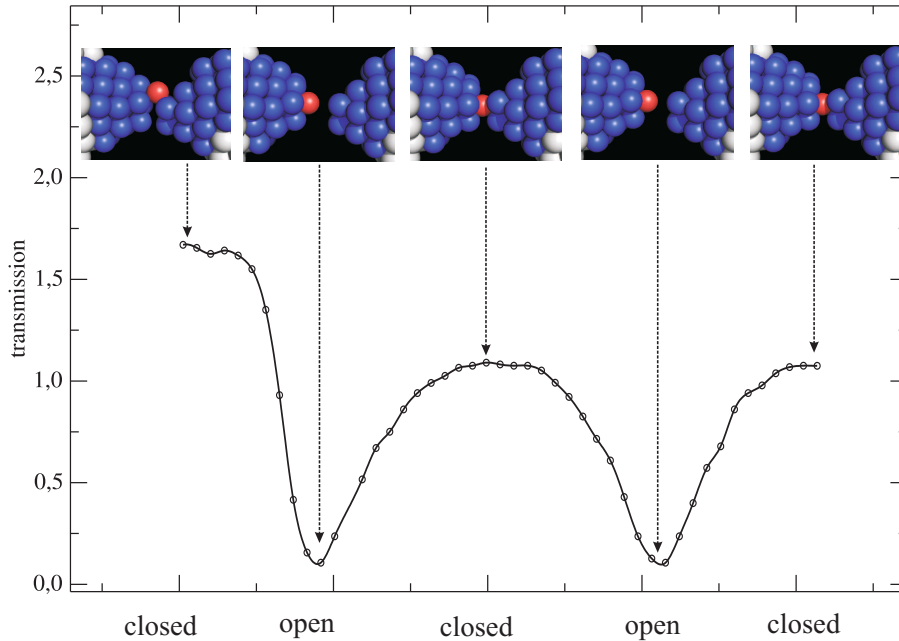
Figure 4.7: *Snapping into a bistable conformation of integer quantum conductance. Two switching processes were simulated starting from a electrode conformation with a non-integer conductance of 1.68 G_0. The first switching cycle induces a structural rearrangement into a more stable electrode geometry, witch permits bistable conductance switching at the integer levels 1 G_0 and 0 G_0.*

4.5 Electrode training-effect

So far in the current calculations a switchable junction was called bistable, if the contact reproduces its conductance value after one switching cycle. However, it is not evident that the junction would yield the same transmission after a second or third opening/closing process, because also thermal fluctuation effects are incorporated into the structure simulations, which might destabilize the tip reconstruction.

Therefore we have repeated this process up to 20 times for five different contact geometries with an „on-state"-conductance of 1, ..., 5 G_0. After every switching cycle, in „on-state"-conformation, we have calculated the average structural deviation from the previous „on-state"-conformation as

$$\Delta R = \frac{1}{N} \sum_{k=1}^{N} |\mathbf{r}_k^{(i-1)} - \mathbf{r}_k^{(i)}| \tag{4.3}$$

with $\mathbf{r}_k^{(i)}$ denoting the position vector of atom k in conformation number i. N is the number of atoms contained in the flexible part of the contact region (blue and red marked atoms). In addition we evaluated the total conductance difference of the junction in conformation $(i-1)$ and conformation (i):

$$\Delta G = |G^{(i-1)} - G^{(i)}|. \tag{4.4}$$

The results are shown in fig. 4.8: The left graphs demonstrate that the structural differences (in units of the Ag-Ag bond length a=2.88Å) of the „on-state"-conformations drastically decreases form 0.03 Å to 10^{-3} Å, i.e., that the bistable tip reconstruction process becomes even more stable with every switching cycle. Since the coherent transmission is directly coupled to the electronic and atomic structure this behavior is also
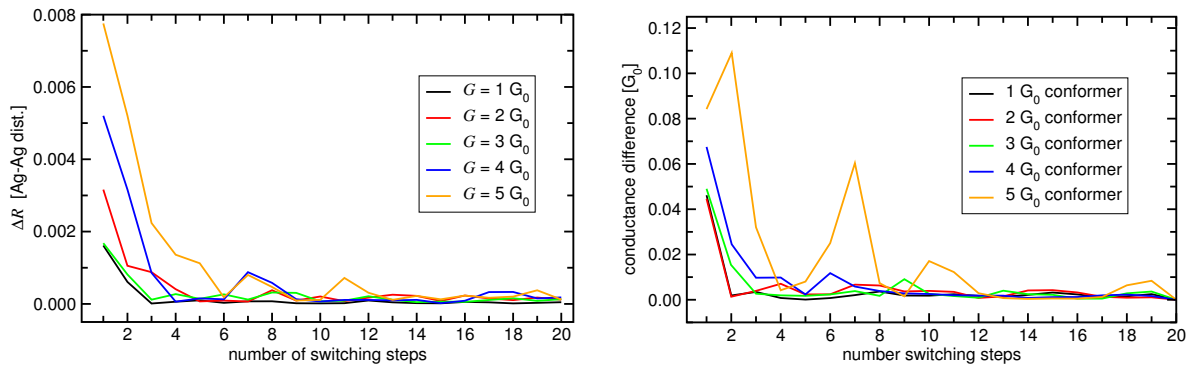

Figure 4.8: *Difference in the computed structure parameter ΔR (left) and the conductance ΔG (right) between subsequent „on-state"-conformations as a function of the switching cycle for selected junctions of 1 G_0, 2 G_0, 3 G_0, 4 G_0, and 5 G_0, respectively. Junctions switch reproducibly for over 20 cycles between increasingly stable on and off conformations (training effect).*

visible in the conductance of the contact: Figure 4.8 (right) shows the conductance deviation ΔG after every opening/closing process. This difference decreases also from an already small value of 0.1 G_0 to 10^{-3} G_0 after 12 switching cycles.

The observed decay of ΔR and ΔG can be interpreted as „training effect", in which the junction geometries become increasingly stable, alternating between two bistable conformations.

4.6 Interlevel switching
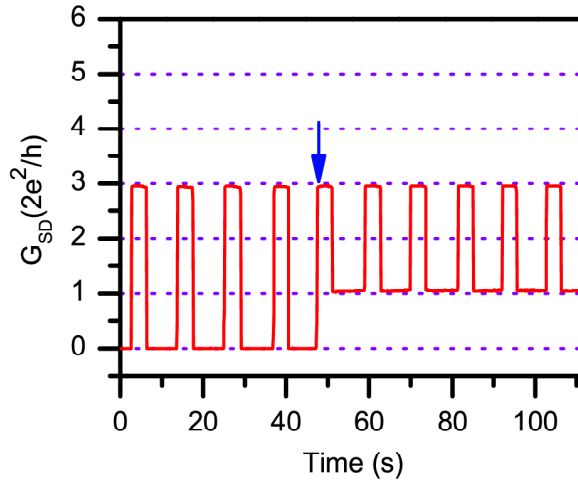
Figure 4.9: *Experimental demonstration of a multi-level atomic-scale transistor switching between an "off-state" and two different "on-states".*

In order to explain the multilevel conductance switching described above, we combine atomic structure simulations of opening/closing processes in silver nanojunctions with zero bias conductance calculations. We generate non-idealized silver electrode geometries by simulation of the deposition process: Starting from distant Ag(111) layers we evolve individual atoms in a material-specific potential for silver. By depositing one ion at a time, we generate junctions with a predefined integer conductance quantum as previously described. Figure 4.10a (left) and (right) shows two final, representative silver nano-junctions consisting of 508 and 561 Ag atoms with 3 and 5 atoms in the minimal cross-section (marked red), respectively

We then simulate many switching cycles for each junction. Experimental modification of the electrochemical potential modulates the interfacial tension of the embedded silver electrodes which results in a mechanical strain on the junction. We simulate the opening/closing cycle of a junction by evolving the atoms of a "central" cluster under the influence of the electrochemical pressure. While the electrodes gradually move apart or closer together, all atoms of the central cluster relax in a quasi-adiabatic path between the open and the closed conformation. The silver nano-junctions in Fig. 4.10a allow for bistable conductance switching between 0 and 3 G_0 (left) or 0 and 5 G_0 (right). In our

simulations, we find a reproducible bistable electrode reconstruction of the central cluster of atoms, allowing for the bistable switching between predefined conductance values.

The calculation of conductance for each electrode displacement step is shown in Fig. 4.10b for these geometries. The leftmost conductance minima (at step 18 for the left junction, at step 37 for the right junction) are related to a complete rupture of the contact yielding 0 G_0 for both conformations. In this case the amplitude of the electrode displacement is 8.55 Å (11.4 Å) for the left (right) silver contact geometry. Using approximate experimental values, we decrease the electrode displacement to 2.85 Å (8.30 Å) for the left (right) electrode in subsequent switching cycles. The reduction of the displacement amplitude results in long-term reproducible, bistable switching between conductance levels of 1 G_0 and 3 G_0 (left panel) and of 3 G_0 and 5 G_0 (right panel).

Close inspection of the intermediate geometries of the junction explains this surprising result, which does not occur for every junction: Some bistable junctions exhibit conductance plateaus, which are characterized not by one, but by a whole ensemble of structurally related conformations. Detailed analysis of this ensemble reveals the mechanism of the multilevel switching which was observed in the experiments described above: For the junction on the left of Fig. 4.10a, a single silver atom rolls over a finite displacement range over the two other bridging atoms to its left (see insets of Fig. 4.10b, left) before finally disconnecting. Choosing the correct displacement amplitude, this induces multi-level switching, because not only the terminal geometries, but also the formation/dissociation pathways are conserved in the switching process. When we repeat the switching cycle for multiple times for both junctions (Fig. 4.10c) we find a lock-in effect with a conductance variation below 0.11 G_0. This lock-in effect is also in agreement with our experimental observations.

To explain the correlation between atomic structure, energy and conductance we calculate the potential energy surface (PES) and the zero-bias conductance for junction geometries generated by independently varying the electrode-electrode distance d and a reaction coordinate r (see Fig. 4.11a) of one specific bridging atom chosen to correlate linearly with d along the observed reaction path ($r = 0.56$ d). We find the global energy minimum at the closed and unperturbed state of the contact (Fig. 4.11b). We find parallel valleys on both the conductance and energy surface, which explain the stability of the conductance plateaus at 1 G_0 and 2 G_0 during the switching process.
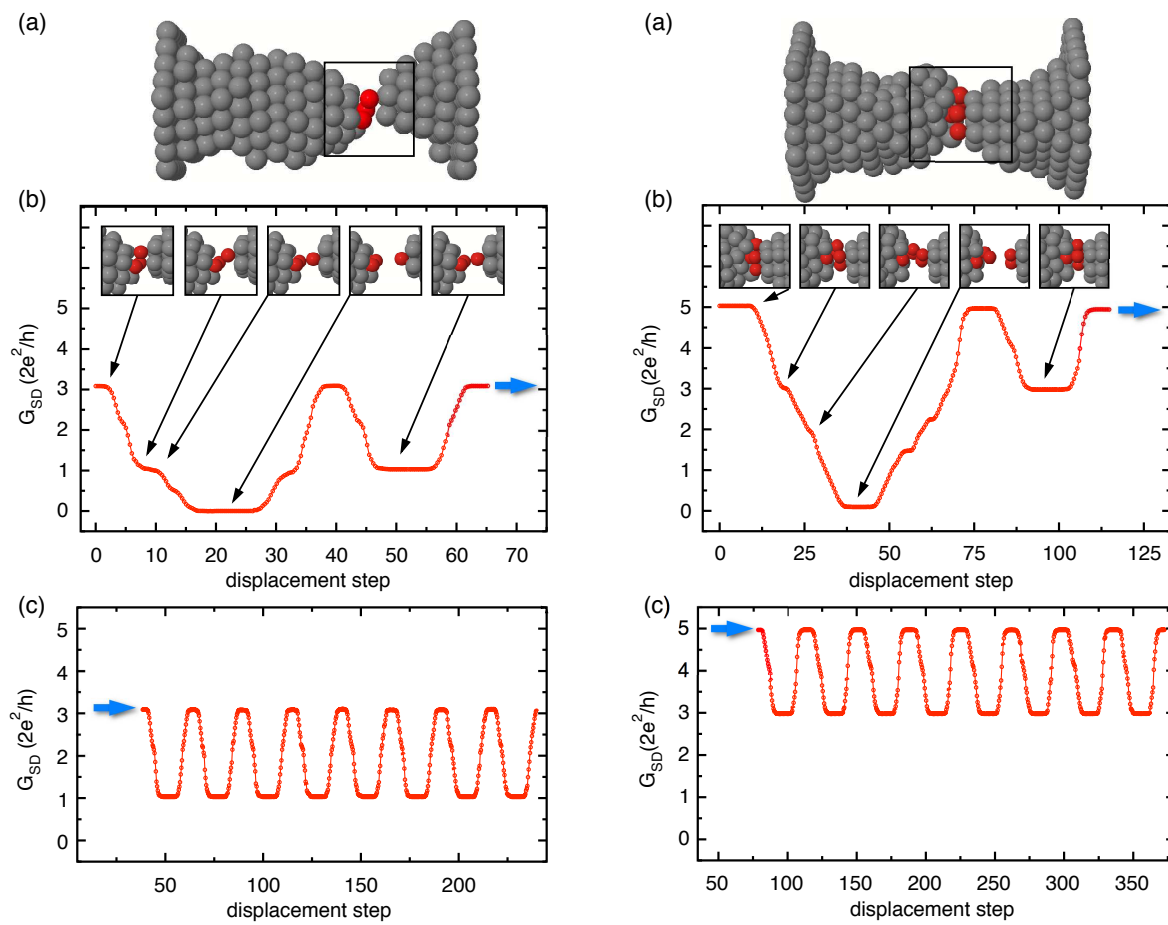
Figure 4.10: *Computer simulations of multi-level-switching conformations switching between 1 G_0 and 3 G_0 (left) and 3 G_0 and 5 G_0 (right): (a) Initial nano-junction conformations in their „on-state" with a conductance of 3 G_0 (left) and 5 G_0 (right). The bridging silver atoms of the minimal cross sections are marked in red. (b) Conductance during two switching cycles with the corresponding tip geometries shown as insets. (c) Subsequent switching cycles follow the sequences shown in (b), demonstrating repeated interlevel switching. The simulation verifies the reproducible bistability of the silver contacts, in perfect agreement with the experimental observations.*
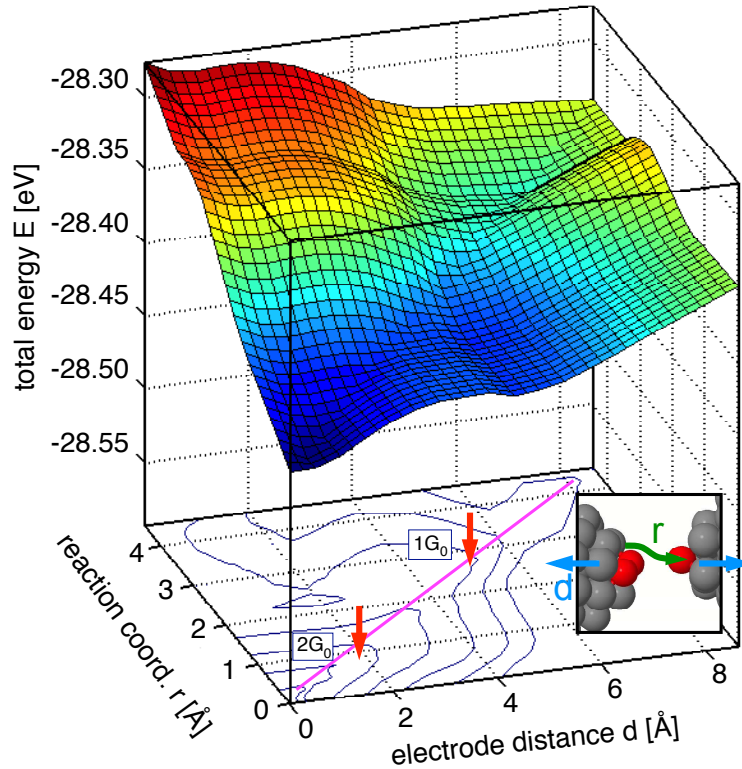
Figure 4.11: *Relation between structure, total energy and conductance of a multi-level point contact: (top) potential energy surface as a function of the electrode distance d and the reaction coordinate r (inset), (bottom) independently computed contour plot of the conductance projected to the bottom of the diagram. The regions indicated by red arrows on the bottom surface indicate parallel valleys on the energy and conductance surfaces. As long as the switching process alternates between points on these two valleys on the energy surface reproducible switching will be observed (Inset) Schematic of the path of the bridging silver atom during the opening process characterized by the reaction coordinate r.*

4.7 Environmental effects on the atomic transistor

The silver ions of the deposition simulations, described in the section above, are exposed to a semi-empirical metal cluster potential (Gupta-potential) and an electrostatic potential, defined by the applied bias potentials and the actual electrode geometry. Figure 4.12 shows a schematic of the circuit including the corresponding potentials of the source, drain and gate electrodes, respectively. The applied voltage of the silver ion deposition is -30.0 mV and the voltage for the transport measurement of the point contact is set to 12.9 mV.

So far we assumed fixed atomic positions as soon as the attached silver ion found its potential energy minimum. However, the applied bias potential leads to a non-vanishing surface charge on the electrodes, which might effect the structural stability of the Ag atoms forming the outer electrode layers.

To estimate the strength of this effect we compare the Ag-Ag binding energy with the electrostatic repulsion energy of the charged surface atoms: Assuming the Gupta poten-

	ϕ_L (meV)	ϕ_R (meV)
deposition	-42.9	-30.0
opening	+17.1	+30.0
closing	-17.9	-5.0
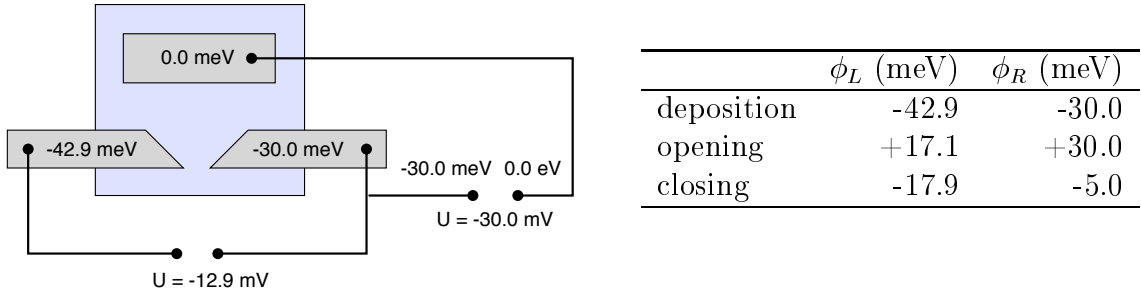
Figure 4.12: *(left) Simplified circuit of the electrodes atomic in the transistor experiment including the applied potentials. (right) The table shows the different electrode potentials during the deposition and switching process of the atomic transistor.*

tial for the metallic binding energy we obtain 2.95 eV for two silver atoms in equilibrium distance of 2.88 Å. If we apply e.g. 1.0 V to a metallic surface, the surface charge per atom is 0.1 - 0.2 e [127], which yields a Coulomb repulsion energy of 0.2 eV for Ag atoms in equilibrium distance. This demonstrates that the influence of the destabilizing coulomb repulsion is at least one order of magnitude lower than the attracting metal-metal interaction. Nevertheless, small changes of the potential energy surface might effect the overall structure of the grown electrodes and the tip reconstruction during the switching process. An additional electrostatic effect in atomic transistor configurations is the screening of the electric field by ions of the electrolyte solvent embedding the electrodes. The presence of ions between the silver contact leads to a decrease of the electrostatic coupling of the electrodes.

Therefore we generalize the model for the structure simulations: In the first step we optimize also the atomic positions in the surrounding of an attached silver ion during the deposition process, to take the rearrangement caused by the charged electrode surface into account. The second step replaces the vacuum between the silver contacts by a continuum description of the embedding electrolyte based on Poisson-Boltzmanns equation. We expect, that both improvements of the model do not change the results of section 4.3-4.6 qualitatively but permit a more realistic treatment of the system and give more insights into environmental effects.

4.7.1 Local relaxation approach

In the ion deposition simulations, described previously, we assumed the atomic positions of the silver cluster ions to be fixed. Only the Ag$^+$ ion going to be adsorbed was allowed to move. Since the attached ion leads to a charge redistribution on the cluster surface the approximation of frozen cluster atom positions may be imprecise.

Therefore, we extend the deposition protocol in the following way: As soon as the inserted ion has attached to the cluster surface and diffused to a stable energy minimum, we reinitialize the point charges of the cluster surface, i.e., the „new" surface atoms charge is approximated by $Q \approx 2\pi a^2 \cdot \sigma$ with the surface charge density

$$\sigma(\mathbf{r}) = e\, \mathbf{n}(\mathbf{r}) \cdot \nabla_{\mathbf{r}} \phi(\mathbf{r})|_{\mathbf{r} \in A} \tag{4.5}$$

and atoms inside cluster (no surface atoms) lose their charge. In this definition **n** denotes the surface normal on the surface A and the nabla operator is discretized by standard finite differences approximation. After that we consider a sphere (radius $R = 3$ Å) around the attached ion and optimize the atomic positions of all atoms inside the sphere using same Metropolis Monte Carlo method as in the previous simulation. The configuration space turns out to be sufficiently sampled if we apply 3 numerical simulated annealing cycles with each cycle consisting of 15000 trial steps.

As a result we find that the stable nearest neighbor distance of the cluster surface atoms increase in average from 2.88 Å to 3.02 Å, as new balance of the interplay between the attracting Gupta potential and the repulsive Coulomb potential. Due to the repulsive effect of the Coulomb interaction we expect a weak destabilization of the bistable tip reconstruction during the switching process. However, all atomic switch conformations we identified as bistable in the previous approach remain bistable, if we include the local relaxation effects.

4.7.2 Electrolyte model of Gouy-Chapman

A charged surface in contact with an electrolyte attracts nearby counter ions and repels its coions present in the solution (Figure 4.13). The surface charge and the attracted counter ions represent the so called Electrical Double Layer (EDL). Such a counter ion cloud is likely to react to the applied electric field and can significantly change the electrical properties of the solid surface. In microscopic systems those effects become even more important because in this regime the applied electric fields can be very strong due to the very small dimension and radius of curvature.

The Gouy-Chapman (GC) continuum model assumes that the EDL consists of two layers of charge: On one hand the surface electrons of the metal and on the other hand the layer of the attracted ions, which are able to move in solution and so the electrostatic interactions are in competition with Brownian motion. This leads to a region close to the electrode surface containing an excess of one type of ion and an exponential potential drop over the region called diffusive layer (see fig 4.13). Extending the ideas from Gouy and Chapman, Stern assumed an additional so called „compact layer", i.e., a region of maximal counter ion density at the metallic surface screening the metal potential ϕ_0 to an effective value $\phi_0 - \zeta$, with the shift ζ being determined from electrokinetics measurements.

The phenomenon of the exponential decay of the surface potential assumed in the GC representation is directly predicted by Poisson-Boltzmann theory. This approach is based on the following assumptions:

- Ions embedded in the solution are supposed to be pointlike charges.

- The ionic soluion is supposed to be a dilute solution, thus the ions do not interact with each other.

- The solvent water is considered as a continuum dielectric of permitivity $\varepsilon = \varepsilon_0 \varepsilon_r$.
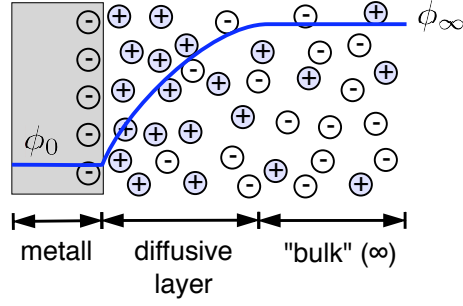
Figure 4.13: *Schematic of a electrical double layer occurring at the metal/electrolyte interface. The region of the exponential potential drop due to the interplay of attracting screening forces and repealing Brownian motion is called „diffusive layer".*

The electrostatic potential $\phi(\mathbf{r})$ in the solution is induced by the metallic surface and acts on each ion concentration c_i, which is given by Boltzmann distribution function

$$c_i = c_i^\infty e^{-\frac{z_i e \phi}{kT}} \quad \text{with} \quad c_i^\infty = n_i c^\infty. \tag{4.6}$$

Here c_i^∞ denotes the ion i concentration in bulk, n_i is the number of ions i, c^∞ denotes the bulk concentration and z_i is the ion i charge number. Equation (4.6) directly points out the interplay between electrostatic $z_i e \phi$ and thermal energy $k_B T$. The ion distribution c_i is related to the charge distribution q_i via

$$q_i = z_i e c_i. \tag{4.7}$$

Thus we obtain the total charge density to be

$$q = \sum_i q_i = \sum_i z_i e c_i. \tag{4.8}$$

According to standard electrostatics the resulting potential $\phi(\mathbf{r})$ is given by Poissons equation $\nabla\left[-\varepsilon \nabla \phi(\mathbf{r})\right] = q$. Using the actual charge density (4.8) we obtain

$$\nabla\left[-\varepsilon \nabla \phi(\mathbf{r})\right] = \sum_i z_i e c_i^\infty e^{\frac{z_i e \phi(\mathbf{r})}{kT}}. \tag{4.9}$$

We can simplify the previous equation in the particular case of a binary symmetric electrolyte with $z_+ = |z_-| = z$ and $c_+^\infty = c_-^\infty = c^\infty$. Thus we obtain from the Poisson-Boltzmann equation (4.9) the so called Gouy-Chapman equation [128] :

$$\nabla\left[-\varepsilon \nabla \phi(\mathbf{r})\right] = -2zec^\infty \sinh\left(\frac{ze\phi(\mathbf{r})}{kT}\right) \tag{4.10}$$

The situation simplifies even more, if the thermal energy can be assumed as large compared to the electrostaic energy $ze\phi \ll kT$, which is typically fulfilled at room temperature. In this regime we can linearize equation (4.10) to

$$\nabla\left[-\varepsilon \nabla \phi(\mathbf{r})\right] = -\frac{2z^2 e^2 c^\infty}{kT} \phi(\mathbf{r}). \tag{4.11}$$

With previous approximations we can directly solve for the electrostatic potential and obtain $\phi(x) = \phi_o e^{-x\kappa}$ with

$$\kappa = \sqrt{\frac{2z^2 e^2 c^\infty}{\varepsilon k T}}. \tag{4.12}$$

The characteristic length κ^{-1} is called Debye length and is widely used to estimate the EDL thickness, because its simple formula depends only on the electrolyte characteristics.

Idealized geometries

Before we address the more complicated Poisson-Boltzmann potential in atomic transistor conformations we want to briefly discuss three simple one-dimensional situations (see fig. 4.14), but already in a parameter space chosen according to the experimental conditions of the bistable silver point contacts of interest. In the following we always consider the case of an aqueous electrolyte ($\varepsilon_r = 78.5$) at ambient temperature ($T = 298$K). The bulk concentration is chosen to be $c^\infty = 0.1$M and the charge number is $z = 1$. We solved in all three cases of fig. 4.14 the linearized GC equation $\phi''(x) = \kappa^2 \phi(x)$ obtaining $\phi(x) = Ae^{\kappa x} + Be^{-\kappa x}$.

In case (a) the surface potential on the left, where a metal is assumed, is chosen to $\phi_L = 43$meV and on the right the solution should fulfill the condition of $\phi(\infty) = 0$. Thus we obtain the plotted solution $\phi(x) = \phi_L e^{-\kappa x}$. The thickness of the present electrical double layer is defined by the distance d where the potential $\phi(x)$ decreased to the value ϕ_L/e so $d = \kappa^{-1}$. Note that the thickness of the electrochemical double layer does not depend on the value of the ϕ_L, only on the charge z, the concentration c^∞ and the temperature T of the electrolyte.

In case (b) and (c) the parameters of the general solution $\phi(x) = Ae^{\kappa x} + Be^{-\kappa x}$ have the form

$$A = \frac{\phi_R - \phi_L e^{\kappa s}}{e^{-\kappa s} - e^{\kappa s}} \quad \text{and} \quad B = \frac{e^{-\kappa s}\phi_R - \phi_L}{e^{-\kappa s} - e^{\kappa s}} \tag{4.13}$$

with s denoting the distance of the electrodes. In (b) the electrode distance s was assumed to be 50 nm according to the initial electrode distance of atomic transistor conformations before the ion deposition starts. Since the gap between the electrodes is large compared to the thickness of EDL and the electrostatic potential in infinity is set to $\phi(\infty) = 0$ by the third gate electrode the potential is nearly equal to zero in the region between the electrodes. If the electrode distance is drastically reduced to 7.6 Å, which equals three times the Ag-Ag distance of 2.88 Å, the EDL of the left and the right contact overlap significantly and thus the potential $\phi(x)$ gets close to the linear solution of the vacuum situation.
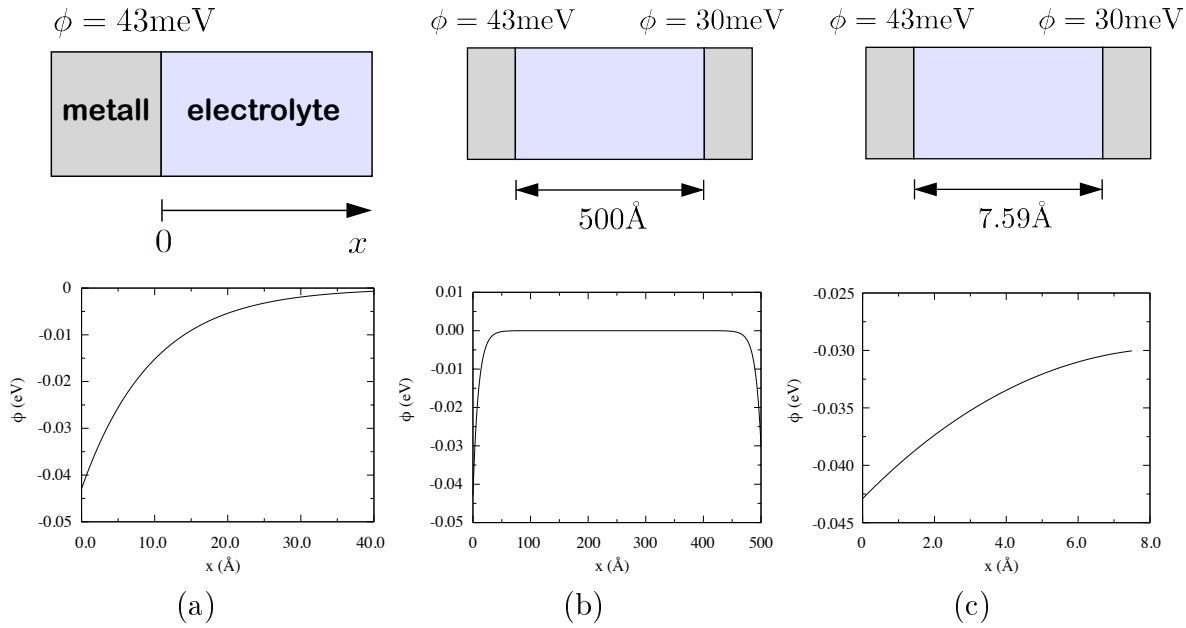
Figure 4.14: *Examples of one-dimensional Poisson-Boltzmann problems at different cases of boundary conditions. Below the geometry the solution $\phi(x)$ of the Poisson-Boltzmann equation is shown: (a) Electrolyte in front of a metallic wall. (b) Electrolyte between two well separated metallic walls at different potentials. (c) Electrolyte in a narrow gap between two metallic electrodes.*

### 4.7.3 Electrical double layer in atomic transistor conformations

In the previous discussion of the Poisson-Boltzmann approximation to the electrolyte influence we have restricted the situation to simple and intuitive one dimensional problems. In longitudinal charge transport direction of atomic switch conformations occurs the same situation of a one-dimensional Poisson-Boltzmann problem with two fixed boundary potentials. However, in this device there are two additional dimensions perpendicular to the transport direction and an irregularly formed electrode surface leading to a more complex situation.
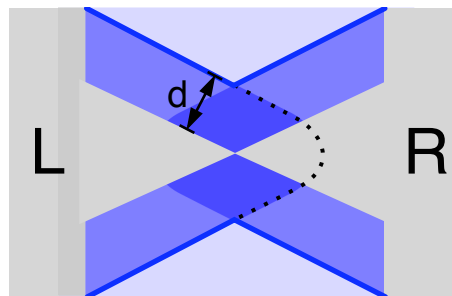
Figure 4.15: *Schematic representation of the overlapping electrochemical double layer surrounding the silver point contact in atomic transistor conformations.*

Figure 4.15 shows a schematic representation of the electrochemical double layers screening the electrostatic potential of electrons of the two silver tips in a metallic point contact. Since there is only a microscopic gap between both electrodes the double layers of thickness d overlap in the contact region.

The full three dimensional complexity of the atomic switch conformation is taken into account in fig. 4.16: Here we plot the electrostatic potential in a single atom transistor conformation projected to a sectional plane in parallel to charge flux direction. In case (a) the silver clusters are surrounded by vacuum and we use fixed Dirichelet boundary conditions at the lead surface with the experimentally applied electrode potentials 43 meV and 30 meV at the left and right contact, respectively. The four remaining boundaries of the simulation box ($40 \times 30 \times 30$ Å^3) were assumed to be of von Neumann type, i.e., the derivative of the potential perpendicular to the simulation box surface has to vanish. In vacuum the potential varies within the boundaries given by the electrode potentials $\phi_L < \phi_P(\mathbf{r}) < \phi_R$. However, in the case of an embedding electrolyte (fig. 4.16b) the potential varies between $\phi_L < \phi_{PB}(\mathbf{r}) < 0$, due to the presence of screening ions. As expected the potentials in a) and b) agree in closer surrounding of the electrodes. Nevertheless, far away from the electrodes, in particular on the top and bottom of the sectional planes in a) and b) we observe a huge quantitative difference of ϕ_P and ϕ_{PB}. In absence of the electrolyte (a) there is a monotonous behavior of $\phi_P(\mathbf{r})$ along the edges $(y, z) = (0, 0)$ and $(y, z) = (H, 0)$. The screening effect of the electrolyte ions dominates the potential $\phi_{PB}(\mathbf{r})$ at this region in case (b) so we observe local extremes at $(x, y, z) = (L/2, 0, 0)$ and $(x, y, z) = (L/2, H, 0)$. According to the experimental conditions of electrolyte concentration and temperature we find $\kappa^{-1} = 10$ Å. However, we have to remark that the assumptions made in the GC-approach [127] may lead to an overestimation of κ^{-1} of the order of 30%, depending on the bias voltage.
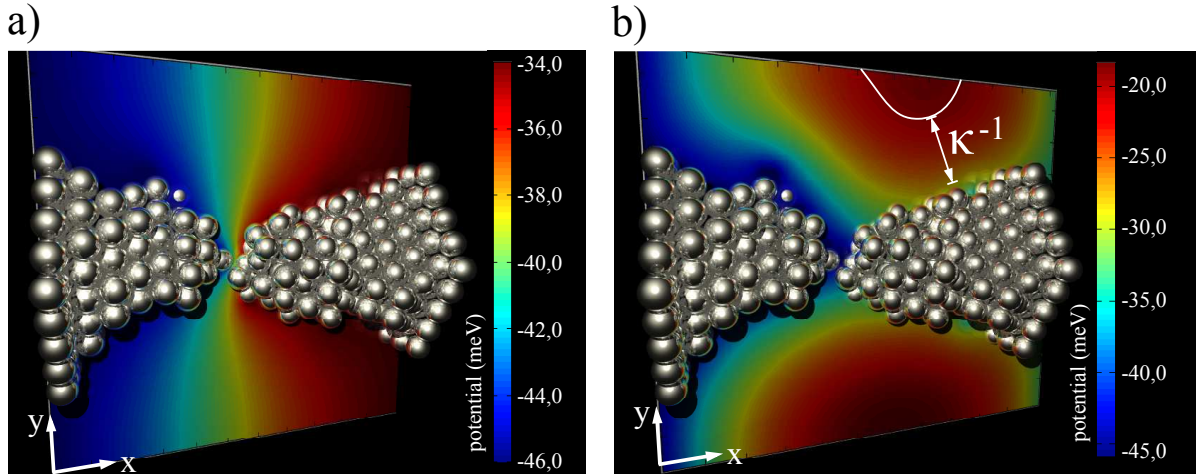

Figure 4.16: *Potential distribution mapped to a sectional plane along the charge flux direction in atomic transistor conformations. (a) Potential of single atom switch in vacuum. (b) Potential of single atom switch screened by ions of the electrolyte. κ^{-1} denotes the thickness of the electrolytic double layer.*

During the electrode deposition process the left electrode cluster grows under the influence of the electrostatic field of the right electrode cluster and vice versa. As an electrolyte contains charged ions the electrostatic field of the electrodes is screened by the covering solvent, which may lead to a systematic change of the junction geometry during the electrode growth process, due to the presence of the electrolyte. Therefore we performed 50 electrode growth calculations in vacuum and with an embedding electrolyte, using the same atom-by-atom deposition simulation protocol as in the previous calculations [100] and compared the electrode conformations grown under the different conditions.

Figure 4.17a shows a schematic of the characteristic shape of the silver junction grown in vacuum (solid line) and under consideration of the electrolyte screening (doted line). At the beginning of the simulation there is still a gap of the order of 30 Å between the left and right electrode, so the silver clusters are well separated and if we take the electrolyte into account, the screening effect dominates the growth process. So far away from the contact region the electrodes grow nearly unaffected by each other, if an electrolyte screens the electrostatic potential. However, in vacuum the growth process towards each other starts earlier at the beginning of the deposition, leading to clearly visible thinner contact geometries than in the electrolyte. This effect is demonstrated in fig. 4.17b and fig. 4.17c, where we show two representative examples of atomic transistor geometries grown in vacuum and in electrolyte, respectively.

The diagram in fig. 4.17d shows the number of atoms n_i per fcc layer i averaged over the 50 grown nano-junctions. According to the examples shown it turns out that n_i^{vac} of the junction in vacuum is about 15 smaller than n_i^{elec} of the junctions taking the electrolyte into account for $i = 1, ..., 9$. If the gap between the clusters gets smaller ($d < 7.0$Å) the electrolyte influence on the electrode tips is reduced and so the difference between n_i^{vac} and n_i^{elec} decreases. As the coherent conductance of such atomic transistor conformations is mainly dominated by the minimal cross section [99, 121] we can exclude an influence of the different electrode shapes on the conductance of the junction. However, the thicker backbone of the electrodes may help to stabilize the tip reconstruction process in the minimal cross section during switching.
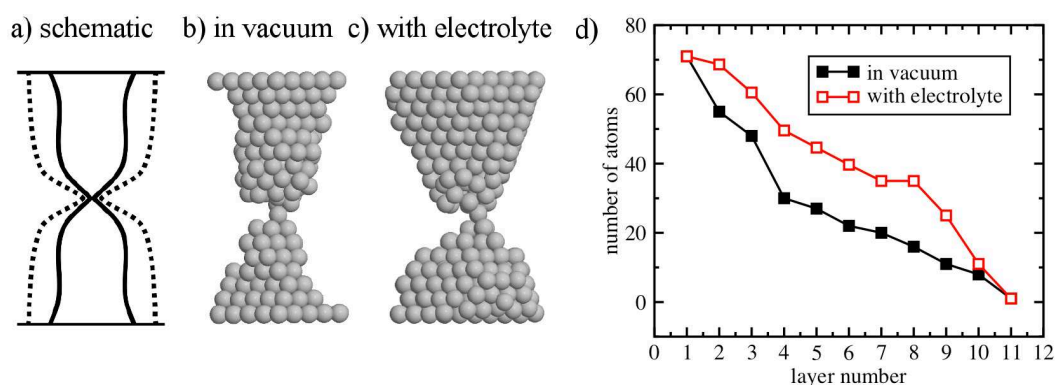
Figure 4.17: *Electrolyte influence on the growth structure of silver point contacts. (a) Schematic of the electrolyte influence on the contact region of a nano-junction. (b) Simulated example of silver point contact conformation in vacuum and with electrolyte (c). (d) Number of atoms per metal layer with and without electrolyte.*

4.8 Intermediate levels at non-integer conductance

High time resolution measurements of the conductance during the contact closing process permit the observation of additional characteristic conductance fluctuations during the contact closing process of the atomic transistor conformation. Figure 4.18 shows three examples of non-integer conductance fluctuations measured at different closing processes of the same single point contact conformation. From the conductance measurement of multiple switching cycles it turned out, that this effect occurs asymmetrically only at switching from „off" to „on" state and not at the inverse process, where the switching is approximately instantaneous. The reason for the non-integer conductance states at the closing process remains unclear, however there are at least two possible explanations of this effect: (i) Additional molecules, e.g. H_2, H_2O, NH_2, in the electrolyte solution might form a bridge between the two electrode clusters and lead to a non-integer conductance or (ii) single atoms of the electrode tip region could hop between the left and right contact induced by thermal energy. This structural fluctuation of the contact geometry could induce the observed conductance variations. The nature of this effect will be examined in the following.
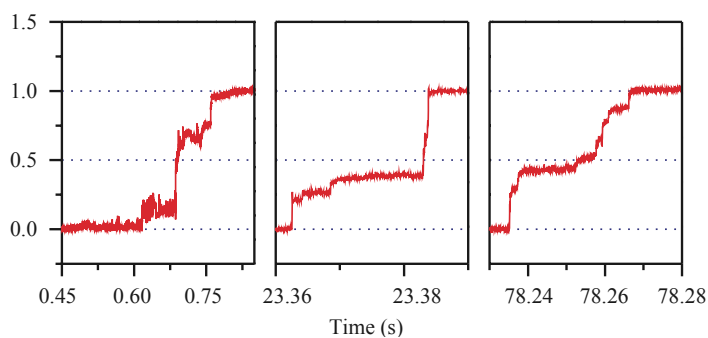

Figure 4.18: *Three examples of conductance fluctuations during the closing process of the same atomic point contact.*
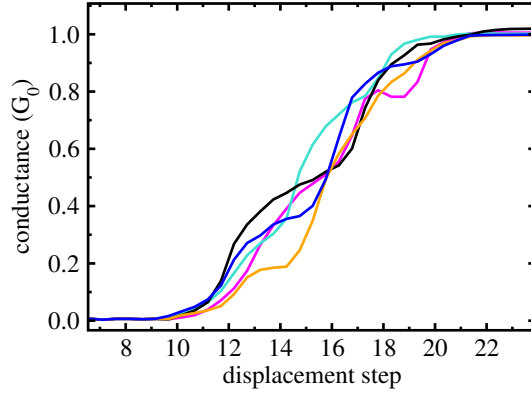
Figure 4.19: *Total conductance of five different single atom transistor conformations during a contact closing process. All five bistable conformations show weak plateaus at non-integer conductance values.*

We have calculated the conductance of five representative single atom switch conformations during the closing process with high resolution of the displacement steps. Additional molecules or ions in the solution are not explicitly represented in the present simulation. With these calculations we want to investigate the nature of the conductance fluctuations during the electrode closing process and clarify whether this effect is due to additional molecules in between the contacts or caused by single atom fluctuations of the bridging atom.

Figure 4.19 shows the calculated conductance curves of single atom switch conformation 1-5 consisting of 634, 622, 631, 649 and 625 atoms, respectively. Similar to the previous simulations we have obtained the underlying contact geometries using the electrode deposition protocol based on Monte-Carlo employing a material specific Gupta-potential as well as electrostatics to describe the Ag-Ag interaction. When we choose a small displacement step size of 0.1 Å, such that the whole contact closing from the displacement of 2.9 Å to 0.0 Å consists of 29 steps, we observe weak plateaus in the conductance curve.
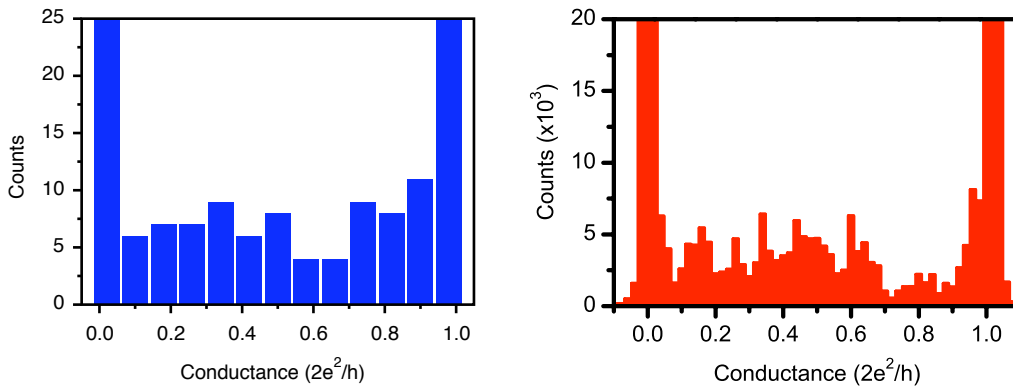

Figure 4.20: *Conductance histograms: (left) Calculated histogram based on the conductance curves shown in the previous figure. (right) Measured conductance histogram showing local maxima at non-integer conductance values. (Note: The height of the peaks at 0.0 G_0 and 1.0 G_0 has no physical meaning, because the number of counts at these values depend only on the number of „time"-steps of the open and closed contact situation, which is arbitrarily chosen.)*

In the conductance graphs of fig. 4.19 we find weakly visible plateaus at about 0.3 G_0 and 0.8 G_0 occurring typically at step 14 and step 18.

In addition fig. 6.2 (left) shows a histogram collecting all conductance values of the previous five conductance curves (see fig. 4.19). Here we use histogram spacing of 0.08 G_0 for the columns of the y-axis. The histogram representation again confirms weak plateaus at about 0.3 G_0 and 0.8 G_0, however, the distribution at these values is rather broad.

Nevertheless, the comparison with the experimental histogram fig. 6.2 (right) shows qualitatively the same features. As we do not take additional molecules or ions into account in the simulations, thus we can conclude, that their disturbing influence in experiment does not lead to conductance fluctuation in the closing process of the contact. From the simulations we find that the conductance noise in this case is due to single Ag-atom mobility: As illustrated in fig. 4.21 the potential energy surface (here illustrated in two dimensions) has a barrier between the local energy minimum at the left and the right contact. Approaching the silver contacts stepwise decreases the energetic height of the barrier. At the critical height $E_c = k_B T$ the thermal energy enables the silver atoms to hop from the left energetic minimum to the right and vice versa leading to small conductance fluctuations until the minimum is unique at the closed state of the contact.
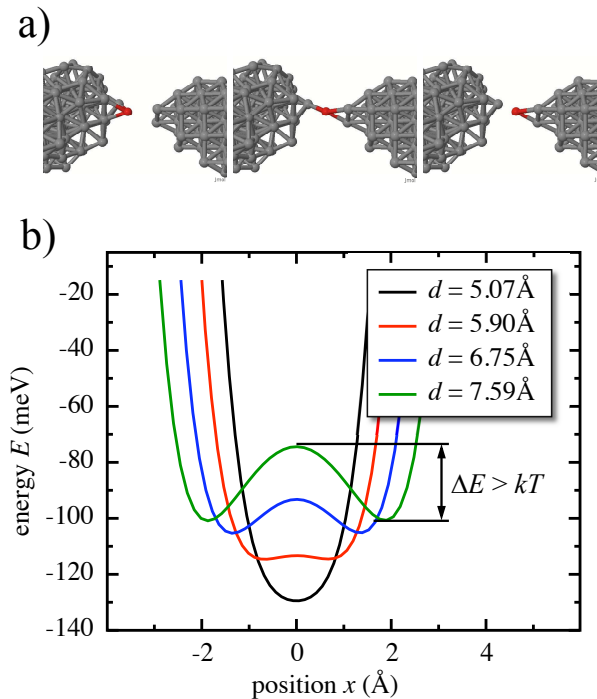
Figure 4.21: *(a) Point contact conformation with a silver atom (red) in a meta-stable state leading to conductance fluctuations during the switching process. (b) Formation of a potential barrier between the stable positions at the left and right contact. With decreasing electrode distance d the temperature induced conductance fluctuations vanish again.*

4.9 Summary and outlook

In the present chapter we have developed a multi-scale simulation protocol to investigate various properties of the single atom transistor. The approach combines a physical analysis on three different length scales: (i) Electronic properties were treated within the material specific extend Hückel model Hamiltonian and are used as input for the Landauer-Büttiker scattering theory. (ii) The geometric structure of the nano-junction was calculated with atomistic resolution using the (classical) many-body Gupta-potential. (iii) Electrostatic properties including the effect of the electrolyte was taken into account employing a continuum model - the well established Poisson-Boltzmann theory.

Using this approach we find that the bistable reconfiguration of the electrode tips is the underlying mechanism of the formation of nano-junctions with predefined levels of quantum conductance. These levels are determined by the physically realizable bistable junction conformations, similar to magic numbers for metal clusters [126], that are most likely material-specific. For silver, the observed quantum conductance levels appear to coincide with integer multiples of the conductance quantum.

In agreement with the experiment we find, that at halting the deposition process at a non-integer multiple of G_0, subsequent switching cycles either converge to an integer conductance at a nearby level or destroy the junction. By snapping into bistable conformations, junctions are mechanically and thermally stable at room temperature for long sequences of switching cycles. We can explain this experimental observation with the obtained electrode „training-effect" at repeated switching of the electrode conformation, which increases the bistability of the tip reconstruction at every switching cycle. In addition we could explain the measured interlevel switching with the occurrence of metastable contact conformations with integer quantum conductance giving rise to plateaus in the conductance curve at a complete rupture of the contact. Besides these plateaus we could also figure out the reason for the observed weak conductance fluctuations at non-integer conductance values. According to our model they can be traced back to single atom hopping between two neighboring stable energy minima induced by temperature. Furthermore we have analyzed the influence of the dielectric double layer in atomic transistor conformations generated by the electrolyte and find, that this screening electrochemical environment leads to an additional stabilization of the switching process.

In future such devices may be manufactured using conventional, abundant, inexpensive, and nontoxic materials and possess extremely nonlinear current voltage characteristics, desirable in many applications. Their electrode arrays can be deposited with lithography, making devices compatible with existing electronics. Because the switching process is achieved with very small gate potential (mV), the power consumption of such devices may be orders of magnitude lower than that of conventional semiconductor-based electronics. Integrated circuits based on this novel principle of operation represent a completely new class of quantum electronic devices, also opening intriguing technological perspectives. Figure 4.22 demonstrates the operation of two atomic transistors in parallel. Using the previously described multi-scale model we can contribute to the device optimization and determine boundaries for the minimal atomic transistor distance where two bistable conformations still can operate and optimize the electrostatic conditions taking the electrolyte into account.
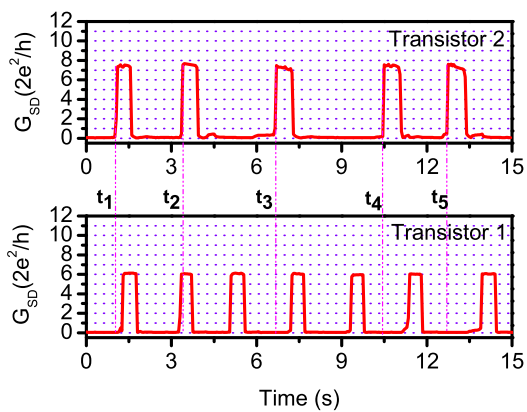
Figure 4.22: *Parallel and independent operation of two atomic transistors grown on one and the same substrate chip in a common electrolyte.*

5 Conductance of organic wires

In recent years, several experimental groups have reported measurements of the transport characteristics of individual or small numbers of molecules. Even three terminal measurements showing evidence of transistor action has been reported using carbon nanotubes [129, 130] as well as self-assembled monolayers of conjugated polymers [131, 132]. A fundamental property of a molecular wire is the scaling of the conductance with the wire length, a behavior which is a direct consequence of the charge transport mechanism. For short molecules (< 3 nm) connected between metallic contacts it is well accepted that the conductance decays exponentially with the system length. However, measurements of the conductance of short molecules in dependence of their length are challenging, because of the strong variation of the contact geometry. Additionally, in previous experimental works it has been difficult to systematically examine the hopping regime in conjugated molecular wires connected to metallic contacts, because of the relatively large range of molecular lengths required (spanning many nanometers) and the complexity of adsorbing long molecules to metal surfaces while controlling orientation. Electrical transport measurements on molecules up to 18 nm in length have been reported [133], and charge hopping in molecular junctions has been observed [134–136], but systematic length dependence of conduction has not been a principal focus.

In the present work so far we have discussed only mono-nuclear extended molecule regions, but it is well known that the presence of metal-organic interfaces complicates electronic structure and, as a result, electronic transport calculations. After a short experimental motivation of the topic we perform benchmark calculations on the coherent transport properties of oligo-phenylene wires in order to validate the RGM for organic wires. In addition we examine the influence of thermally induced structural disorder on the conductance of these molecules. Finally we investigate the relation between structural, electronic and transport properties of oligo-phenyleneimine wires and discuss the results in comparison with experimental observations.

5.1 Experimental motivation

Recently Choi *et al.* (*Science* **320**, 1482 (2008)) performed measurements which provide direct evidence for a change in transport mechanism from tunneling to hopping in molecular junctions based on conjugated oligo-phenyleneimine (OPI) wires of varying length (1.5 - 7.3 nm). The molecules were deposited on a gold substrate (forming the bottom electrode) and contacted via an atomic force microscope (AFM) tip to create the second contact (see fig. 5.1). They could show that near 4 nm in length, the mechanism of transport in the wires changes abruptly, as evidenced by striking changes in the length, temperature, and electric field dependence of the current-voltage ($I - V$) characteristics.
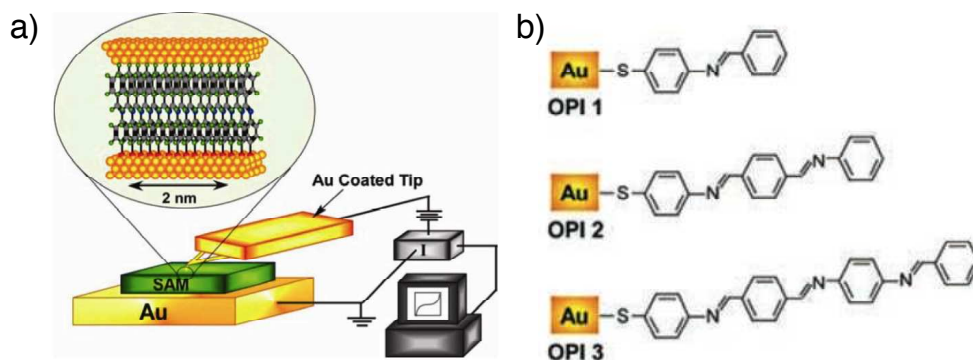
Figure 5.1:   *Experimental setup for the investigation of charge transport characteristics (i. e. length dependence) in organic wires [132] (a) A self-assembled monolayer of molecular chains is fabricated on a gold substrate, which forms the first electrode. The second electrode is introduced by contacting the monolayer with an AFM-tip from the top. (b) The self-assemble monolayers consist of oligo-phenyleneimine (OPI) wires ranging in length from 1.5 to 7.3 nm. They covalently bond to the substrate via sulphur.*

OPI molecular wires were grown on the gold substrate by immersing gold into 1 mM 4-aminobenzenethiol in absolute ethanol, followed by a stepwise growth process with alternate addition of benzene-1,4-dicarboxaldehyde and benzene-1,4-diamine. Each wire terminated with -NH$_2$ or -CHO groups was end capped with benzaldehyde or aniline, respectively to provide a consistent terminal group throughout the OPI series that facilitates reproducible electrical characterization. Afterwards they extensively examined the obtained monolayer by ellipsometry, x-ray photoelectron spectroscopy (XPS), reflection absorption Fourier transform infrared spectroscopy (RAIRS) and cyclic voltammetry (CV). In addition to other structural information they could conclude that the OPI wires are tilted with an angle increasing from 20 deg. to 45 deg. with respect to the surface normal as the wire length increases.

After the preparation and characterization of the monolayer they performed the investigation of the transport characteristics using the already mentioned conducting probe (CP) AFM (fig. 5.1a). The results regarding resistance R versus molecular length L are shown in fig. 5.2: Each data point in the semi-logarithmic plot represents the average of 10 $I - V$ traces. They observe a clear transition of the length dependence of the resistance near 4 nm, which corresponds to the length of OPI5, indicating that the conduction mechanism is different in short (OPI1 to 4) and long (OPI6 to 10) wires. In the case of short wires the linear fit in fig. 5.2 indicates that the data are well described by the exponential resistance dependence

$$R(L) = R_0 e^{\beta L} \qquad (5.1)$$

for non-resonant tunneling, whereas the corresponding β value was found to be 3 nm^{-1}. The extremely small β in the case of long OPI wires suggests that the principal transport mechanism is hopping. The inset of fig. 5.2 shows a non-logarithmic plot of R versus L, which indicates a linear resistance increase in the case of long wires. This is consistent with the assumption of hopping transport in this regime, thus equation (5.1) does not
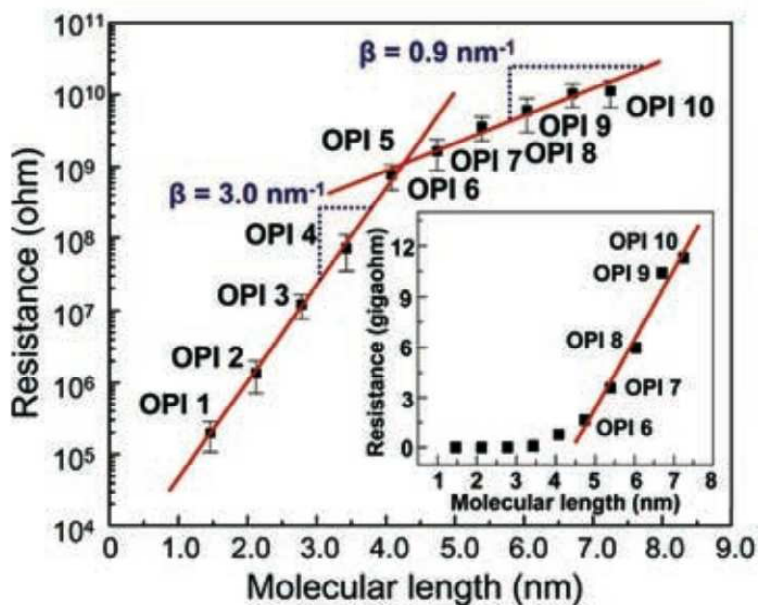
Figure 5.2: *Length-dependent resistance plot of oligophenyleneimine wires taken from ref. [132]. Since the resistance of OPI 1-4 increases exponentially the underlying transport mechanism is expected to be non-resonant tunneling. The current through wires longer than OPI5 is based on electron/hole hopping processes, deduced from the linear length dependence of the resistance in this case.*

hold for OPI6 to 10. Performing additional measurements of the temperature dependence of the resistance they could validate the different transport mechanisms [132].

Nevertheless, several questions remained regarding the nature of the hopping sites in long wires. Choi *et al.* found an activation energy for the hopping process of 0.28 eV, which might be the energy barrier for the electronic hopping process or the energy required to change the dihedral angles of the molecular ring units to flatten the wire and thus extend the π-conjugation. Understanding the origin of this value would lead to a better overall understanding of the transport mechanism in such kind of organic wires. Using ultraviolet-visible absorption spectroscopy the authors demonstrate that the conjugation does not extend over the entire wire, but rather electronic delocalization is limited to 3 repeating ring units. Comparing these results with electronic structure and transport calculations can give insights into the distribution of the actual occurring dihedral angles in the molecular wire.

5.2 Recursive Green's function method applied to organic systems

5.2.1 Transmission of benzene wires

Applying the RGM method to silver and gold quantum point contacts has already shown the reliability of the method in the case of metallic devices. Before investigating the

conductance properties of OPI wires it is necessary to check the reliability of our RGM implementation in the case of well studied organic systems. We have therefore studied the coherent conductance of phenyle-di-thiol (PDT), a „drosophila" of molecular electronics. Because this molecule was studied extensively in the past [11, 137–143], it allows for a comparison of the RGM approach with experiment and various other levels of theory. We investigate the transmission of oligophenylene molecules of varying lengths, which lend themselves nicely to an investigation of the layer approximation in an organic, semi-conducting system. The structure of the molecules suggests a natural introduction of layers in terms of single phenyl-ring units, similar to the layers introduced by base-pairs in DNA [122].
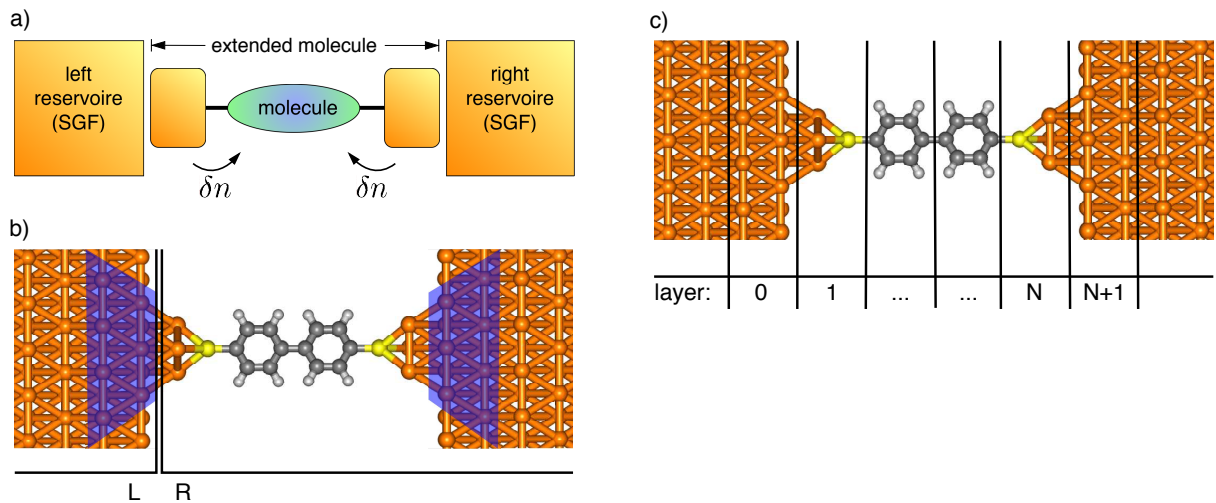
Figure 5.3: *Schematic representation of the different regions of a single molecule junction in the Landauer approach. (a) Definition of the extended molecule including a fraction of the electrodes. This permits the natural charge transfer δn and screening effects as an organic system is attached to a metal surface. (b) Realization of a molecular junction by a phenyl-ring-based wire coupled via sulphur atoms to the [111]-layers of gold leads. The semi-infinite leads are represented by their surface Green's function defined on the atoms of the blue colored area. Horizontal lines indicate a possible division into a left and and a right part of the system. (c) Representative division of the system into principal layers to illustrate the recursive Green's function approach.*

Figure 5.4a illustrates the oligiphenylene molecules covalently bound to Au_{19}-clusters, using the same notation as for the conformations in Ref. [98]. The molecule is connected to the Au electrodes at both sides by a symmetric covalent bond of a sulfur atom to three Au atoms. In the literature this bonding situation is referred to as the hollow position [98]. The electrode clusters where constructed from fcc lattices as above, while the geometry of the phenyle wires was optimized using density functional theory (DFT) in the local density approximation (LDA) [98, 144, 145]. As can be seen in Fig. 5.4a there is a non-vanishing tilt-angle between the phenylene-rings, which varies between 33.7 and 34.5 degrees due to the interplay of steric repulsion and π-conjugation of adjacent rings. A detailed investigation of the influence of (conjugation induced) tilting on the coherent transport properties in biphenyle-derived dithiols was recently given in Ref. [51].

In Fig. 5.4b the total transmission is shown as a function of energy for the molecular junctions above, once with (dashed line) and once without the layer approximation (solid line). Due to the neglect of several overlap matrix elements the transmission and conductance obtained with the layer approximation is below the full device transmission. The measured conductances of oligophenylene wires with amine end groups indicate even lower conductance values which may arise from the differences in the coupling to the electrodes. With increasing length of the phenyl wire the transmission gap decreases from 3.89 eV to 2.56 eV. The equidistant transmission at the Fermi energy of the different molecular wires indicates the correct exponential decrease of the conductance with linear increasing wire length [131, 146–148].
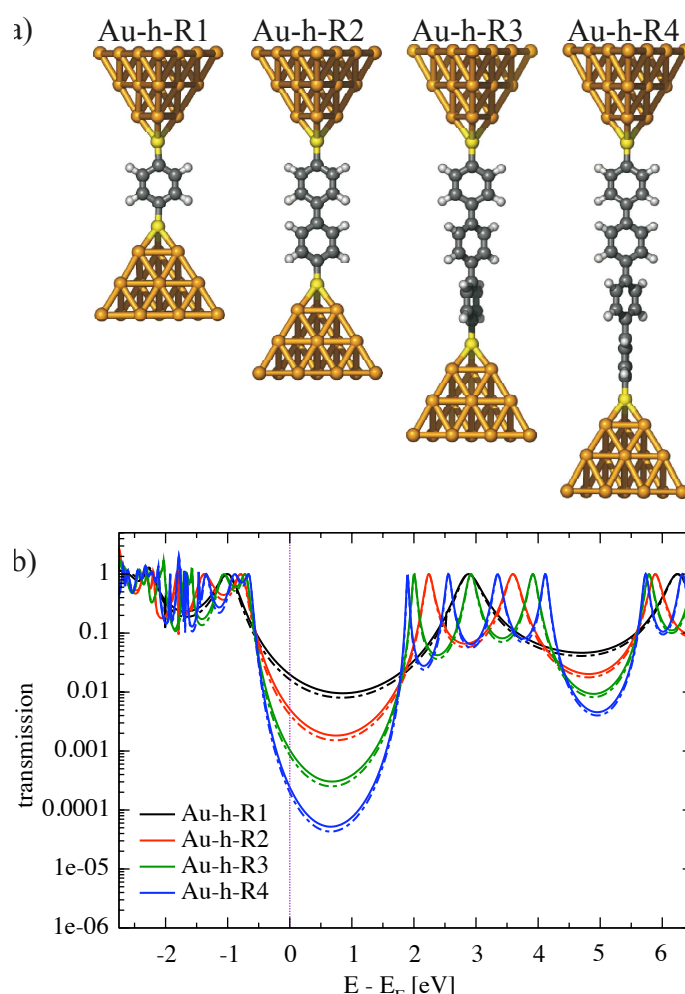
Figure 5.4: *Configurations of the organic molecular wires studied in this work. (a) Oligophenylene molecules covalently bond to Au_{19} clusters along the cristallographic [111] axis. One phenylene ring unit represents one principal layer. (b) Total transmission as a function of the energy of the shown oligophenylens with (dashed line) and without (solid line) the principal layer approximation in good qualitative agreement with the DFT results of Ref. [149]. In the layer approxiation one principal layer contains a single phenyle ring unit. The vertical line indicates the Fermi energy.*

5.2.2 Length dependence of the conductance

The proportionality of the conductance decay $G/G_0 \sim e^{-\beta N}$ of the oligophenylene wires, once with and once without the layer approximation, is shown in Fig. 5.5. In both cases we obtain a decay coefficient $\beta = 1.47$ which is close to the experimental value $\beta_{exp.} = 1.5$ reported in [148] for amine end groups. Nevertheless, the comparison between theory and experiment remains difficult because of the different end groups used.
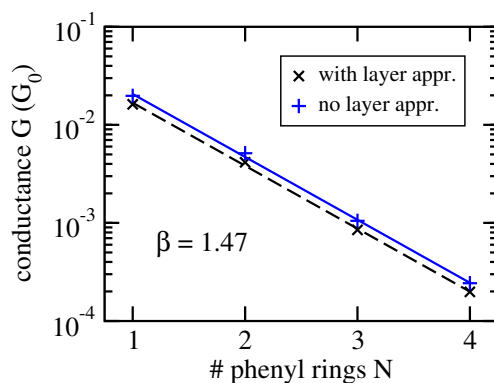
Figure 5.5: *Length dependence of the conductance of the oligophenylene wires. The conductance decreases exponentially with the number of the phenyle rings in the wire in good agreement with experimental data.*

5.3 Conductance fluctuations of oligo-phenylene wires

Next we investigate the influence of thermally induced molecular vibrations on the coherent transport properties of an Au-h-R4 wire. For the simulation of the dynamics of the system we use of the AMBER 8 molecular dynamics package [150], which employs the well established GAFF-forcefield and a Langevin thermostat method to model temperature. Assuming fixed gold atoms of the electrodes we simulate the evolution of the system at 300 K for 10 ps in time steps of 2 fs. Every 10-th time step a snapshot of the conformation is taken as input for the conductance calculation generating 500 conformations for analysis. For each conformation we calculate the zero-bias conductance. Within the simulation period we find repeated conductance fluctuations by more than an order of magnitude.

Recent investigations have already focused on the influence of intramolecular vibrations on the conductance [100]. Here, we find an interesting model system where thermal fluctuations induce large-scale conformational change. The conductance of a conformation correlates highly with its „planarity", because the fully planar conformation leads to a strong overlap of the π-orbitals, which in turn increases the transmission. However, such planar configurations are forbidden at zero temperature because of steric repulsion of the hydrogen atoms emanating from the rings. Figure 6.5a shows the fluctuation of the torsion angles ϕ_1, ϕ_2 and ϕ_3 between the ring-units occurring in Au-h-R4, respectively. All three torsion angles fluctuate strongly around an equilibrium average of 31.9 degrees, which agrees well with the experimentally observed equilibrium value of 34 degrees. The

histogram Fig. 6.5b shows that the outer torsion angles ϕ_1 and ϕ_3 have slightly broader distributions than ϕ_2, which may be caused by the lower potential energy barrier at the electrodes. The average conductance over 10 ps arises as an average of strongly fluctuating instantaneous values, as illustrated in Figure 6.5c.

In the course of the the 10 ps simulation we find 6 "near-planar" configurations of adjacent rings and 2 "near-planar" conformations of all three rings. To characterize this geometric feature we compute the average of the absolute torsion angles $\bar{\phi} = \frac{1}{3}(|\phi_1| + |\phi_2| + |\phi_3|)$, which has 4 minima (with $\bar{\phi} < 20$ deg.) and 3 maxima (with $\bar{\phi} > 45$ deg.) in the observation period. As illustrated in Fig 8c the conductance has associated minima where $\bar{\phi}$ is maximal, e. g. at 2.2, 4.3, and 9.4 ps. Correspondingly the highest conductance values are obtained, if $\bar{\phi}$ is small, e. g. at 4.6, 5.5, and 9.8 ps. This effect is also illustrated in Fig. 6.5d, which gives a higher time-resolution of the grey regions of Fig. 6.5a and 6.5c. This analysis shows that the experimentally relevant conductance at room temperature arises as an average of thermally excited high-conductance conformations, which are forbidden at zero temperature.
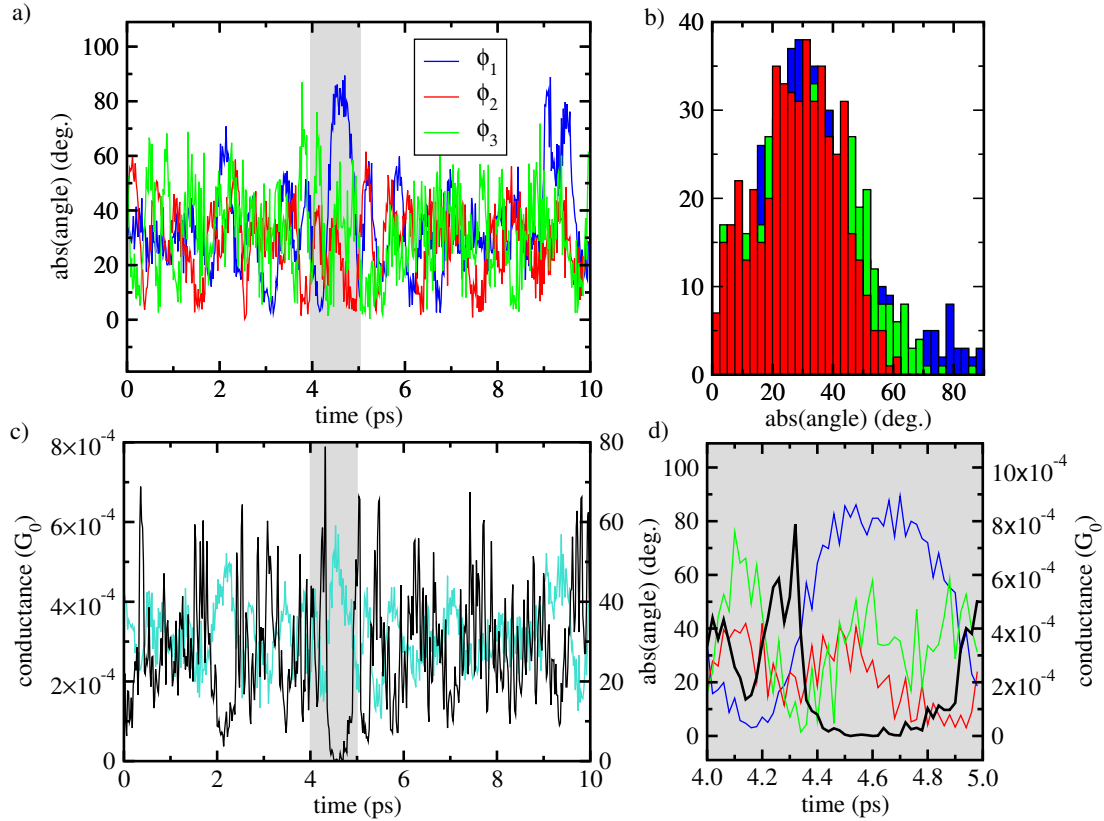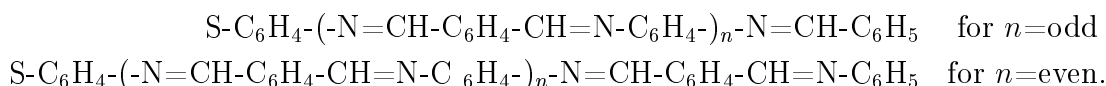

Figure 5.6: *Thermal influence on the conductance of a molecular wire at 300 K.(a) Fluctuation of the torsion angles ϕ_1, ϕ_2 and ϕ_3 between the ring-units occuring in Au-h-R4, respectivley. (b) Distribution histogram of the frequency of occurrence of a particular torsion angle. (c) Corresponding conductance (black) and average torsion angle $\bar{\phi}$ (turquoise) at the fluctiation process durring 10 ps simulation time. (d) Zoom into the 4ps-5ps range, which shows that a short-time increase of the torsion angles (red, green and blue curve, left axis) leads to a strong decay of the total transmission (black curve, right axis) of the nano wire.*

5.4 Oligo-phenyleneimine wires

Starting from benchmark calculations assuming an experimentally and theoretically well investigated organic system - oligo-phenylene wires - we could show, that the recursive Green's function approximation is able to predict the conductance within a reasonable accuracy. Choosing the principal layer thickness parameter d to 4.4 Å allows for a correct reproduction of the length dependence of the conductance compared to experiments and higher levels theory results. After ensuring the reliability of the method in calculation of the transmission function of organic systems, we want to investigate the structural and electronic properties of OPI wires. The nature of the transition from coherent to incoherent transport should be clarified considering the influence of dihedral angles and the extension of the frontier orbitals.

5.4.1 Structural properties

Compared to the previously discussed oligophenylene wires, the oligo-phenyleneimines (OPI) consist also of stringing phenylene ring units and of a thiol group at one end. However the main structural differences are the lacking second thiol group at the other end of the wire and the way how the phenylene ring units are connected. In the case of the OP wires the connection is formed directly between two C atoms of the ring ($\cdot C_6H_4$-$C_6H_4\cdot$), however OPI wires consist of an additional $\cdot N{=}CH\cdot$ unit between every phenylene ring unit. For reasons of the synthesis of these molecular wires always two N atoms point towards the C_6H_4 ring or away from it. Thus the whole wire is built up by the scheme

$$S\text{-}C_6H_4\text{-}(\text{-}N{=}CH\text{-}C_6H_4\text{-}CH{=}N\text{-}C_6H_4\text{-})_n\text{-}N{=}CH\text{-}C_6H_5 \quad \text{for } n{=}\text{odd}$$
$$S\text{-}C_6H_4\text{-}(\text{-}N{=}CH\text{-}C_6H_4\text{-}CH{=}N\text{-}C_6H_4\text{-})_n\text{-}N{=}CH\text{-}C_6H_4\text{-}CH{=}N\text{-}C_6H_5 \quad \text{for } n{=}\text{even}.$$

First of all we have optimized the geometries of OPI1-OPI5 using the density functional theory (see chapter 2.2.3) implementation TURBOMOLE [144]. Here we apply generalized gradient approximation (BP86), a Gaussian type orbital basis set as well as effective core potentials to describe the influence of the nuclei plus inner shell electrons. In order to obtain the equilibrium conformation of the molecules we use density functional molecular mechanics under the condition $-\partial E/\partial \mathbf{R}_k = 0$, with $\mathbf{R}_k$ being the nuclear coordinates. The so called Hellmann-Feynman-Theorem [151, 152] states that

$$-\frac{\partial E}{\partial \mathbf{R}_k} = \langle\psi|\frac{\partial H}{\partial \mathbf{R}_k}|\psi\rangle \tag{5.2}$$

$$= \int d^3r\, n(\mathbf{r})\frac{Z_k e^2(\mathbf{r}-\mathbf{R}_k)}{|\mathbf{r}-\mathbf{R}_k|} + \sum_{k<l}\frac{Z_k Z_l e^2(\mathbf{R}_k-\mathbf{R}_l)}{|\mathbf{R}_k-\mathbf{R}_l|}, \tag{5.3}$$

similar to the prediction of electrostatics. The current atomic arrangement is stable if the electronic and the ionic part of the Hellmann-Feynman forces vanish, which can be simulated using a conjugate gradient method like implemented in Turbomole.

For the occurring C-C single bonds we obtained a length of 1.41 Å on average, for the
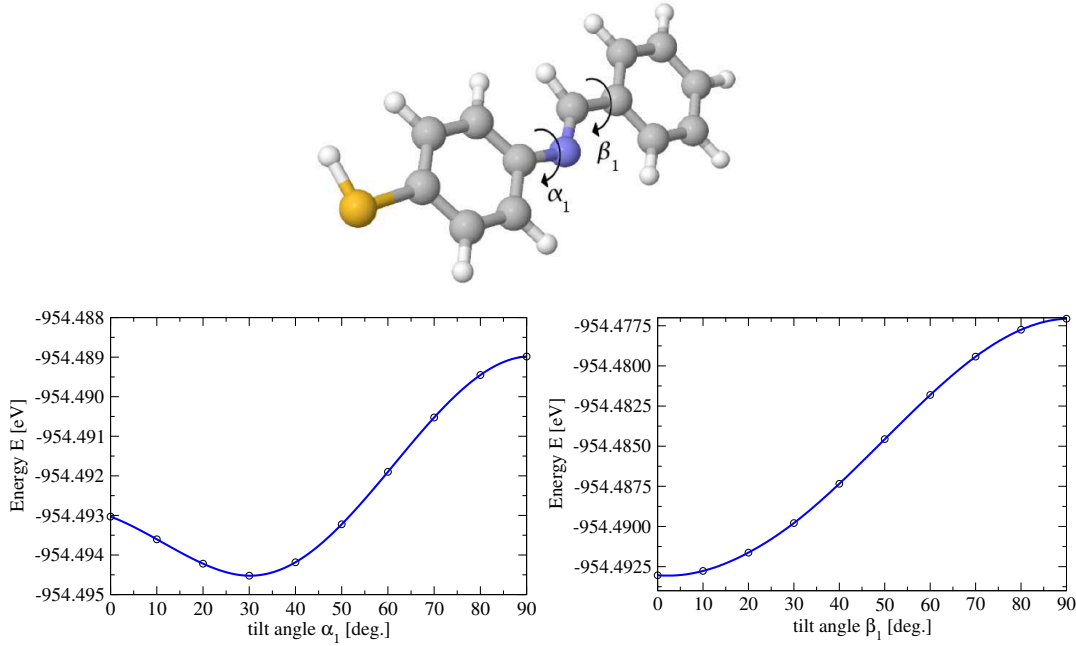
Figure 5.7: *(top) Conformation of the OPI1 molecular wire pointing out the torsional angle α_1 and β_1. (left) Total energy depending on α_1 showing an energy barrier of 5.5 meV. (right) Total energy depending on β_1 showing an energy barrier of 15.5 meV.*

double bonds C=C a length of 1.47 Å and for the N=C bond 1.29 Å. The total molecular length, which is the terminal H to S distance for OPI1-5 amounts to 1.45, 2.11, 2.76, 3.41 and 4.06 nm, comparing well with the experimental findings of 2.1, 2,8 and 3.4 nm for OPI2-4 [132], respectively. Additional structural parameters are the dihedral angles α and β between the N-C and C-C bond shown in fig. 5.7 for the case of OPI1. In contrast to β, which is equal to zero, the average value of α is 31.9 deg. due to the stearic repulsion of the hydrogen atoms pointing towards each other (see fig. 5.7). The graphs below the conformations show the total energy of the wire during twisting the wire by $\alpha = 0,...,90$ deg. or $\beta = 0,...,90$ deg., respectively. It turns out that the energy barrier for a full rotation for α is $\Delta E_\alpha = 5.5$ meV and β the barrier is $\Delta E_\alpha = 15.5$ meV. In comparison to the thermal energy $k_B T = 25$ meV at room temperature, the rotational energy barriers of the OPI wires are clearly lower, thus strong thermal fluctuations of the π-conjugation of the molecules can be expected.

5.4.2 Electronic properties

Coherent as well as incoherent charge transport properties mainly depend on the distribution of the orbitals over the molecule, so after investigating the geometric structure of the OPI wires we examine their electronic properties. The DFT calculations on the equilibrium geometries of OPI yield also the electronic structure. In the present work we calculate the so called Kohn-Sham-gap defined as

$$E_g^{\mathrm{KS}} = \varepsilon_{\mathrm{LUMO}} - \varepsilon_{\mathrm{HOMO}}. \tag{5.4}$$
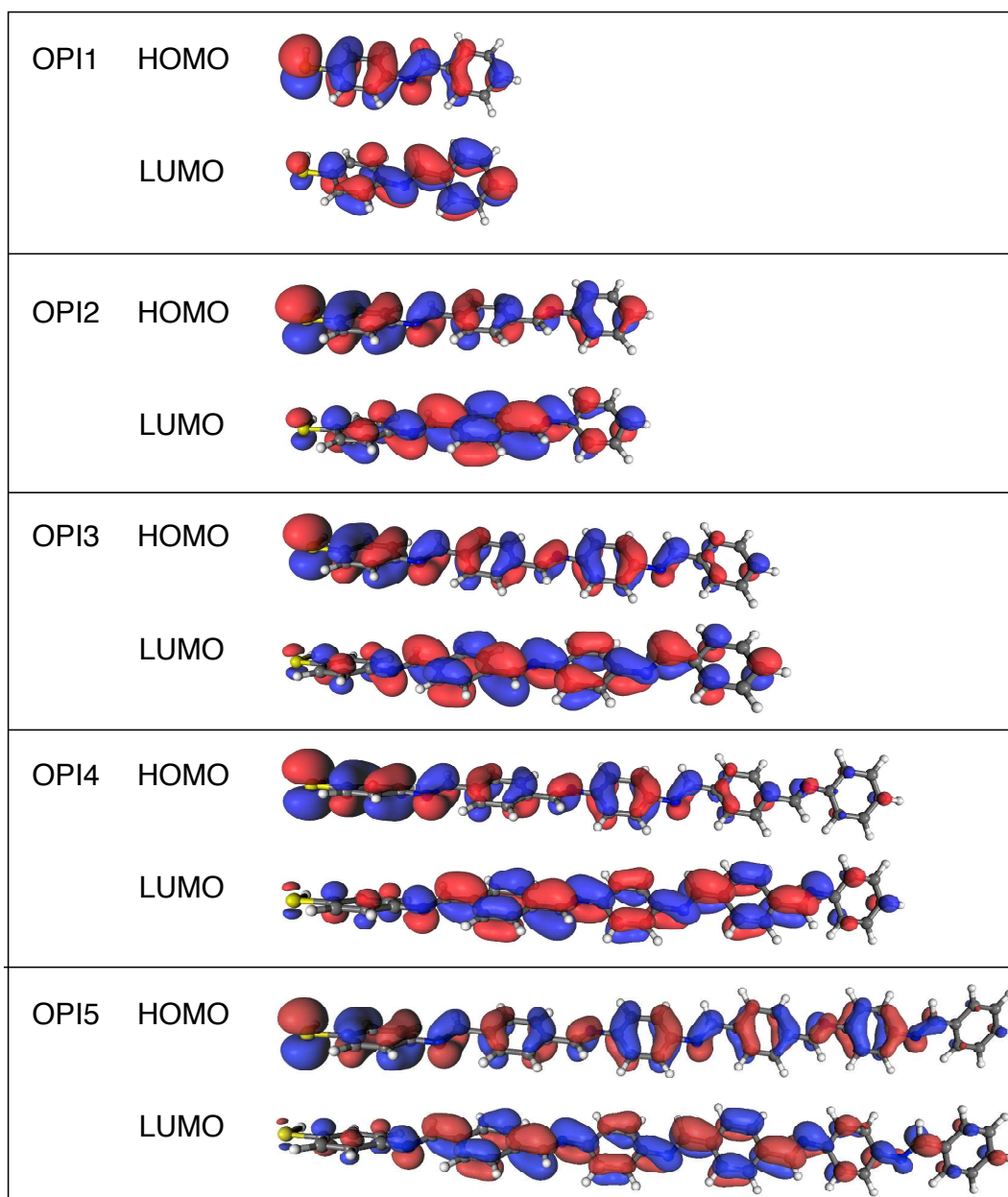
Figure 5.8: *Iso-surface plots of the frontier orbitals of OPI1-5 at an iso-value of partial charge density of 0.01 a.u. The color code red and blue corresponds to the real and imaginary part of the wave function, respectively. The distribution of the partial charge densities of the HOMO and LUMO permits insights into conjugation length of the molecular wire, which is crucial for the dominant charge transport mechanism.*

It is known that in local density or generalized gradient approximation E_g^KS underestimates the experimental value significantly by about 40%. This absolute value is partially improvable using hybrid functionals for the exchange correlation approximation (like PBE0 or B3LYP). However, in the present study we are interested in the relative change in the gap energy with increasing molecular length. For OPI1-5 we obtain the Kohn-Sham-gap E_g^KS of 2.38 eV, 1.99 eV, 1.78 eV, 1.67 eV and 1.63 eV. For comparison we

calculate also the Hartree-Fock HOMO-LUMO gap energies leading to 5.20 eV, 4.35 eV, 3.87 eV, 3.64 eV and 3.58 eV for OPI1-5, respectively. The decreasing gap energy with increasing the wire length was also observed in experiment [132], however the absolute value of the gap energy in the cases for OPI3-5 is underestimated by 36% in case of DFT and overestimated by 32% in case of HF compared to the experimental results from Choi *et al.* measuring an gap of 2.6 eV. While the underestimation of gap energies in DFT was already discussed, the failure of the absolute HF-gap is due to the lack of electron-electron correlation. In DFT hybrid functionals these errors rather cancel each other than being formally corrected.

Figure 5.8 shows iso-surface plots of the partial charge density distributions of the HOMO and LUMO of OPI1-5, with the real and imaginary part of the wave function marked red and blue, respectively. The charge density is plotted at an iso-value of 0.1 a.u. Both HOMO as well as LUMO have a *p*-like delocalized spatial distribution, but they clearly differ in symmetry. The bonding HOMO has nearly E_{1g}/A' symmetry at the phenylene rings (meaning that there is one single node plan perpendicular to the ring) and the anti-bonding LUMO has E_{2u}/A' symmetry at the ring units (meaning that there are node planes perpendicular to the ring). In addition fig. 5.8 shows that the HOMO is rather localized at the thiol group end than equally distributed over the molecular wire, due to the strong electron affinity of the sulfur atom. However for longer wires the LUMO is mainly localized at the center of the chain. Qualitatively, fig. 5.8 confirms that at OPI4 (and even more at OPI5) the partial charge densities of the frontier orbitals, which are of major importance for the coherent current flow, significantly increases at the right most phenylene ring unit. In addition the LUMO shows the same effect also at the thiol group of the OPI4 and OPI5 wire, reducing the probability for coherent tunneling dramatically. Thus, the electronic structure calculations on OPI molecular wires can explain the transition from tunneling to hopping transport at a critical wire length of 7.3 nm by the spatial distribution of the frontier orbitals. However, one has to note that the calculations above neglect the influence of the metallic electrodes on the partial charge densities, but since the left and right electrode material consists of the same metal (and thus provides the same electron affinity), we assume that their influence on the orbital distribution compensates mutually.

5.4.3 Coherent conductance

Finally we investigate the coherent transport properties of OPI1-5 wires using the previously described recursive Green's function method. In contrast to the oligo-phenylene wires OPI1-5 have only one single thiol group at one end and a hydrogen atom at the other end. Therefore also the electrode coupling is asymmetric: One the „left" end (compare fig. 5.9) we introduce a gold cluster consisting of 25 atoms and assume the sulfur atom of the molecule to bind in a hollow position to the cluster assuming the well known Au-S bond length of 2.36 Å [153]. On the right end of the wire we use a directly opposed gold cluster consisting of 26 atoms with an equilibrium H···Au distance of 1.6 Å taken from ref. [154]. In contrast to the „left" contact, which is formed by a covalent Au-S bond, the right contact is based on weaker van-der-Waals interaction between the wire and the metal cluster. The weak interaction between molecule and electrode on the

„right" end of the system enables a large variety of the contact geometry in experiment due to thermally induced molecule and gold atom mobility, which might be a source of disagreement between experimental and theoretical results.

To utilize the advantages of the RGM we divided the OPI wires into layers by introducing a sectional plane through every C=N double bond occurring in the OPI wire, leading to N principal layers with N being the number of phenylene ring units in the wire. In analogy to the previous calculations on oligo-phenylene wires, we use a material specific extended Hückel Hamiltonian to describe the electronic structure and embed the two left- and rightmost metallic layers of the extended molecule into semi-infinite bulk electrodes described with already stored self-energy matrixes $\Sigma_{L/R}^{r}(E)$.

The lower left part of fig. 5.9 shows an excerpt of the total transmission function $T(E)$ of OPI1-5, which was calculated in an interval of ± 2 eV around the Fermi energy. Since the electrode coupling at the right end of the wire is experimentally not uniquely defined, but the calculations are restricted to one special geometry, we expect deviations between the experimental and calculated transmission, however the relative ordering and distance between $T(E)$ of the OPI wires should be unaffected by this uncertainty. The calculated transmission gap of OPI1-5 amounts 2.38, 1.87, 1.84, 1.85 and 1.84 eV, respectively. This proofs the experimental observation of an decreasing HOMO-LUMO gap of OPI1-3 and nearly constant gap size of OPI3-5. The transmissions at the Fermi edge of OPI1-5, which determines the conductance of each wire, is nearly equidistant in the current logarithmic representation and amounts $3.1534 \cdot 10^{-3}, 2.5459 \cdot 10^{-4}, 2.0 \cdot 10^{-5}, 1.1 \cdot 10^{-6}$ and $6.0 \cdot 10^{-8}$, respectively. This exponential decay of the transmission is characteristic for (off-resonant) coherent tunneling. The lower right part of fig. 5.9 shows in detail the conductance depending on the wire length. Since an exponential decaying behavior is expected we use

$$G(L) = \alpha \; e^{-\beta L} \tag{5.5}$$

as fit-function. The length-dependence parameter $\beta = 3.29$ nm^{-1} compares well with the experimental result $\beta = 3$ nm^{-1} of ref. [132]. The parameter $\alpha = 0.24$ G$_0$ is more difficult to interpret in relation to the measurements, because in experiment the current through a whole set of OPI wires with the same length is measured, thus the total conductance of the SAM is expected to be an unknown multiple of $\alpha e^{-\beta L}$.

5.5 Conclusion

In the present chapter we have probed the performance of the recursive Green's function approach, which divides the extended molecule region into principal layers with nearest neighbor coupling, calculating tunneling transport properties of the well studied oligo-phenylene wires. We obtained reasonable agreement with results of higher level theories (e.g., DFT) for the total transmission function as well as for length-dependence of the conductance. In addition to the validation of the method with oligo-phenylene wires we have investigated the impact of thermally induced large-scale geometric change on the conductance. Averaging the conductance over 500 conformations obtained from a 10 ps molecular dynamics simulation at room temperature, we find temporal conduc-
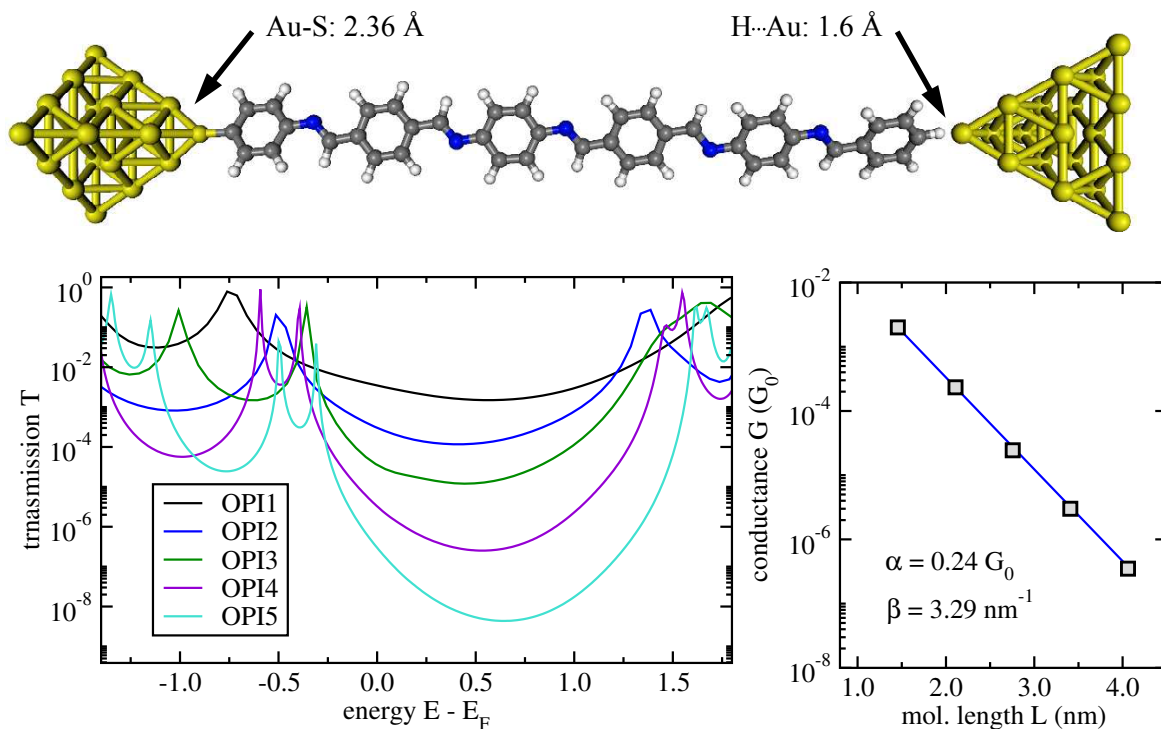
Figure 5.9: *(top) Central device region for calculating the conductance of OPI wires. As an example the OPI5 wire is shown as well as the gold electrode fragments consiting of 25 atoms. Since the molecule contains only one thiol group end there is an asymetry of the left and right electrode coupling. (left) Total transmision function of OPI1-5 close to the Fermi energy. (right) Length-dependence of the conductance of OPI1-5. The conductance decreases exponentially with the molecular wirer length with the given characteristic decay parameter β.*

tance fluctuations of more than an order of magnitude. The average conductance, which agrees well with the experimentally observed value [131], results from high-conductivity conformations that are sterically unfavorable at zero temperature. The advances in the modeling approach thus permit the detailed characterization of disorder effects, which is present in almost all experimental realizations, on the conductance of molecular wires.

Motivated by an experimental study [132] we have investigated the correlation of structural, electronic and transport properties of oligo-phenyleneimine wires. We observed that the two types of energy barriers of the dihedral angle rotations are lower than 16 meV, which is lower than $k_B T$ at room temperature. The measured activation energy for the hopping process of 0.28 eV [132] is one order of magnitude higher than the rotational barriers and thus can not be explained by the energy necessary for flattening the molecule to improve the π-conjugation. The electronic structure calculations confirmed the observation that the charge carrying frontier orbitals do not extend over the entire wire - the electronic delocalization is limited to 3-4 repeating ring units. The total transmission functions of the OPI molecules show the characteristic exponential decay with the wire length and the obtained decay parameter β agrees well with the experimental value [132]. The small deviation may be caused by a flatter molecule geometry in exper-

iment permitting a slightly stronger π-orbital overlap, because in this case the molecules are embedded into a self-assambled monolayer. Additional calculations on the hopping transport properties combined with quantum chemistry methods could give insights into the behaviour of longer wires.

6 Protein embedded nanoparticle deposition

Recently, there has been great interest in self-assembled biostructures as a tool for the controlled fabrication of one-, two-, or three-dimensional ordered nanomaterials and devices [155]. Numerous proteins self-assemble into well-defined superstructures (sheets, wires, tubes, or capsids) and have been used to template particle arrays and nanowires of inorganic materials [156–161], providing unique inorganic-biomolecule hybrids with properties derived from both the inorganic (of magnetic, electric, or optical nature) and the biological (specific recognition capabilities) material. Stress-related proteins may overcome the difficulties of the sensitivity of proteins to the „unnatural" reaction conditions, for example, towards variation of the pH, higher temperatures ($>37.8°$C), and the presence of non-native chemicals, because of their robustness and tolerance of a variety of unnatural conditions [162–164]. Moreover, their potential for application has just recently been demonstrated for *Flash-memory-device* fabrication based on chaperonin-derived nanocrystal assemblies [165].

Motivated by the experimental work of the group of Silke Behrens (Institute of Technical Chemistry, KIT, Campus North) in the present study we will analyse the possibility of metallic nanoparticle growth using an extended protein as template. Therefore, firstly we optimize the protein structure without any metallic extension in aqueous solution under normal ambient conditions. Secondly we generate a set of palladium atoms bonded to the protein, serving as nuclei for the Pd^{2+}-ion deposition. Assuming this start conformation we simulate the deposition of the nanoparticle and end up as soon as the number of metal atoms has reached the measured value. In the following we will answer the question, whether the introduced nanoparticle qualitatively changes the secondary protein structure or stabilizes the entire macro-molecule, which was partially investigated using circular dichroism (CD) spectroscopy, but remained not completely understood.

6.1 Experimental motivation

In their recent work the group of Silke Behrens developed a technique of size-constrained synthesis of catalytically active metal particles using a genetically modified stable protein (SP1) [166,167]. SP1 is a ring-shaped homododecamer (12 mer), 11 nm in diameter, with a central, 2-3 nm inner pore and a width of 4-5 nm. The protein has an extremely high thermal and chemical stability, for example, it exhibits a melting temperature of $107°$C and resistance to detergents, such as sodium dodecyl sulfate (SDS), and to proteases [168]. The experimentalists genetically fused a histidine (His) tag to the N-terminus of SP1 (6hisSP1), thus obtaining a variant with additional His residues facing the inner-pore of

the ring structure [169]. Histidine is a typical metal-binding site in proteins due to the presence of the deprotonated N atom in the imidazole ring, analogous to the N atom of guanine or adenine [170, 171].

When the 6hisSP1 mutant was treated with Na_2PdCl_4 (typically 720 Pd atoms per dode-camer) for 2 h at room temperature, a homogenous pale-yellow solution resulted. Excess Pd was removed by dialysis. The Pd^{2+} ions were subsequently reduced by a reduction bath containing dimethylamine borane (DMAB), resulting in a clear-brown colloidal so-lution, which was stable for several months. Transmission electron microscopy (TEM) imaging of the precipitate revealed aggregated, 3.4-nm-sized particles. The particulate texture and size suggest that the wild-type template also influences initial particle nu-cleation.

Circular Dichroism (CD) spectroscopy was used to analyze the secondary structure of 6HisSP1 before and after the metallization procedure. Figure 6.1 compares the measured CD spectra of the 6hisSP1 mutant and the Pd-6hisSP1 nanobioconjugate. The 6hisSP1 mutant displays the typical CD bands of a protein, which has a significant α-helical fraction with a maximum around 192 nm and two minima at 208 and 221 nm, respectively. After metallization and binding of Pd nanoparticles to 6hisSP1 the maximum weakly shifts to 193 nm and the negative bands approach each other slightly, leading to a steeper shape of the „trough" between the minima.
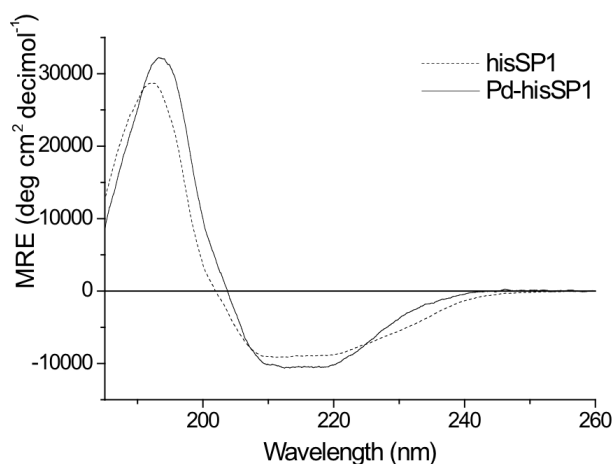

Figure 6.1: *Circular Dichroism spectra of the SP1 protein with and without the deposited palladium nanocluster allowing for the characterization of the secundary structure of the protein.*

The mean residue ellipticities also show minor intensity changes. In order to decide whether the protein denaturates by the metal cluster deposition or whether the main properties of its secondary structure remain unaffected we simulate the protein structure in the framework of molecular dynamics in the cases before and after the metallization and analyze geometrical features. The question whether the proteins secondary structure is conserved (also after metallization) is important, because it decides whether this new hybrid system remains compatible to biological organisms (e.g. in cancer therapy). In addition we will analyze the growth shape of the nanoparticle, which determines its fields technological of applications.

6.2 Protein simulation

After generating a molecular structure of the start geometry of SP1, that consists of 19 different types of amino acids, we consider a cubic box of 11 nm edge length as simulation box for the total energy minimization using the AMBER molecular dynamics package. We use the GAFF force field and periodic boundary conditions in a NPT ensemble. Thus we considered the temperature to be fixed at 300 K modeled by the so called Nose-Hoover-thermostat and assume a pressure of 1 atm. For the solvent treatment we employed a all-atom description of the water molecules in the MD optimization that runs 5 ns.
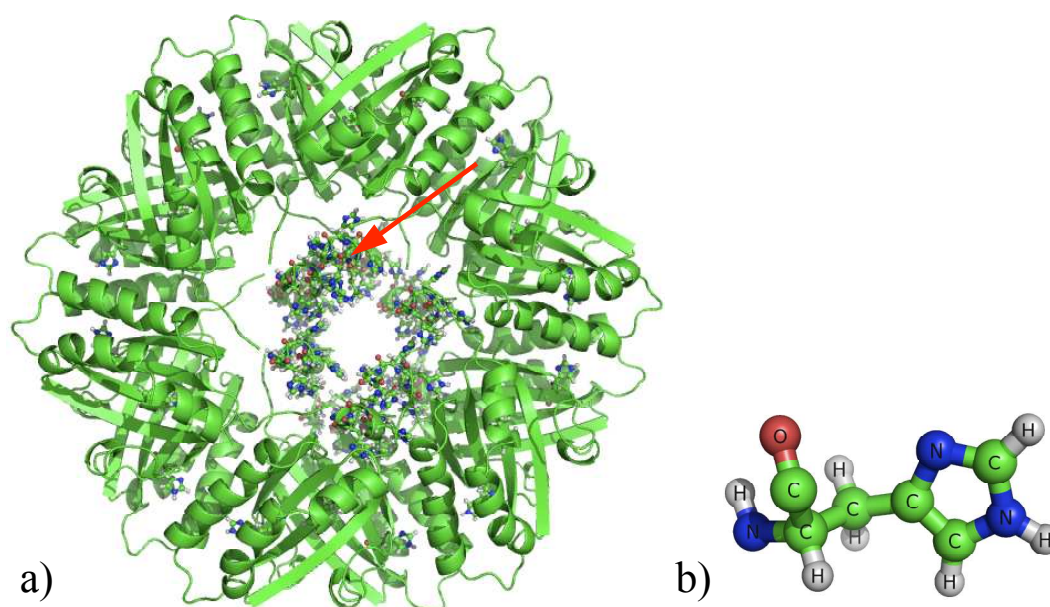
Figure 6.2: *Donut-shaped protein serving as template for palladium nanoparticle deposition: (a) Cartoon representation of the protein's secondary structure. Note the important histidine residues (pointed out by the red arrow) serving as anchoring group for the palladium ions. (b) Three dimensional sketch of an isolated histidine molecule.*

Figure 6.2a shows the resulting protein geometry in secondary/quaternary structure representation. The energy minimized structure has about 10.0 nm outer diameter and 3.5 nm inner diameter. The ring consists of numerous α-helixes arranged in nearly radial direction stabilizing the overall structure of the protein. In the center of the molecule fig. 6.2a shows a smaller inner circle consisting of histidine residues required later for the palladium-protein interface.

6.3 Deposition simulation

Starting from the obtained protein structure we add one single palladium atom at each histidine at the experimentally observed position to the free nitrogen atom of the ring unit (see fig. 6.2b). We have to introduce these covalent bonds „by hand", because

covalent binding can not be predicted by the applied force field based models, however, the occurring histidine-metal coupling was well characterized experimentally [170, 171].

For the metal cluster deposition we employed a recently developed protocol for simulation of nanoscale-structure formation on long time scales [113]. Our simulations comprise two parts: In the first part, we „grow" the nanoparticle, one atom at a time in molecular-mechanics simulations. We observe the nucleation of several palladium nanocrystals emanating from the unprotonated side-chain His N atoms (fig. 6.3, left), which coalesce into a single multidomain Pd-nanoparticle that spans the entire pore (fig. 6.3, right). We deposited up to 800 Pd^{2+} ions, one ion at a time, using a kinetic Monte-Carlo Method. In each simulation the Pd^{2+} ion is placed at a random position outside the protein and evolved for 30000 steps in the electrostatic potential generated from the protein (AMBER charges) and the partially formed Pd-cluster using also a short-range Gupta-potential [115] for Pd. The protein is taken into account as external Lennard-Jones potential. When the Pd^{2+} ion attaches to an existing cluster it is reduced. The obtained palladium nanoparticle has a compact nearly spherical shape with a diameter of 3.5 nm.
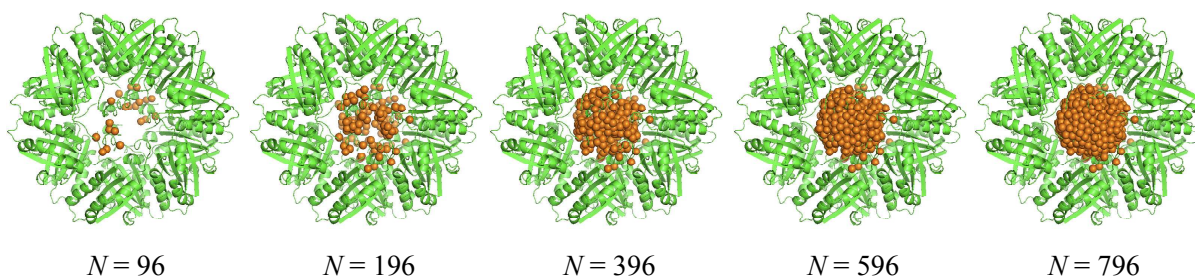

Figure 6.3: *Snapshots of palladium (yellow atoms) nanoparticle deposition using an extended protein as template. The 96 atoms shown in the left-most frame serve as adsorption nuclei for the particle growth process. After deposition of about 800 palladium atoms a ball-shaped metal cluster has formed in the center of the protein ring.*

6.4 Influence of the palladium cluster

Using the generated nanoparticle/protein complex, we can analyze the fluctuations of the protein with and without nanoparticle in molecular-dynamics simulations using the Assisted Model Building and Energy Refinement (AMBER) [150] forcefild. We find that the protein alone equilibrates into a conformational ensemble with approximately 2.5 Å RMSD (root mean square deviation) from the starting structure, and the presence of the metal nanoparticle constrains the conformational ensemble to within 1.1 Å RMSD of the starting conformation.
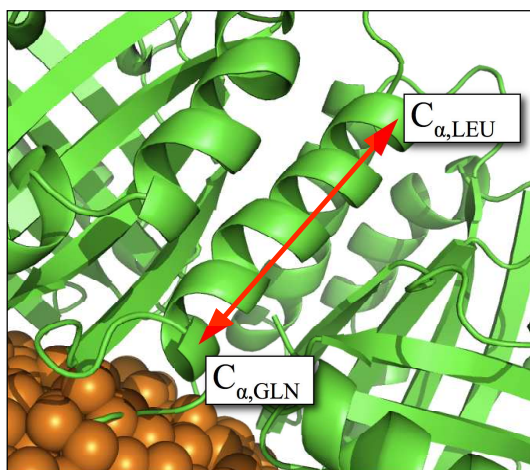
Figure 6.4: *Arbitrarily chosen α-helix segment of the SP1 protein to study the thermally induced fluctuations of the atomic position (in terms of the rmsd) of $C_{\alpha,GLN}$ and the distance between $C_{\alpha,GLN}$ and $C_{\alpha,LEU}$ at both ends of the chain in the two cases with and without the nanoparticle.*
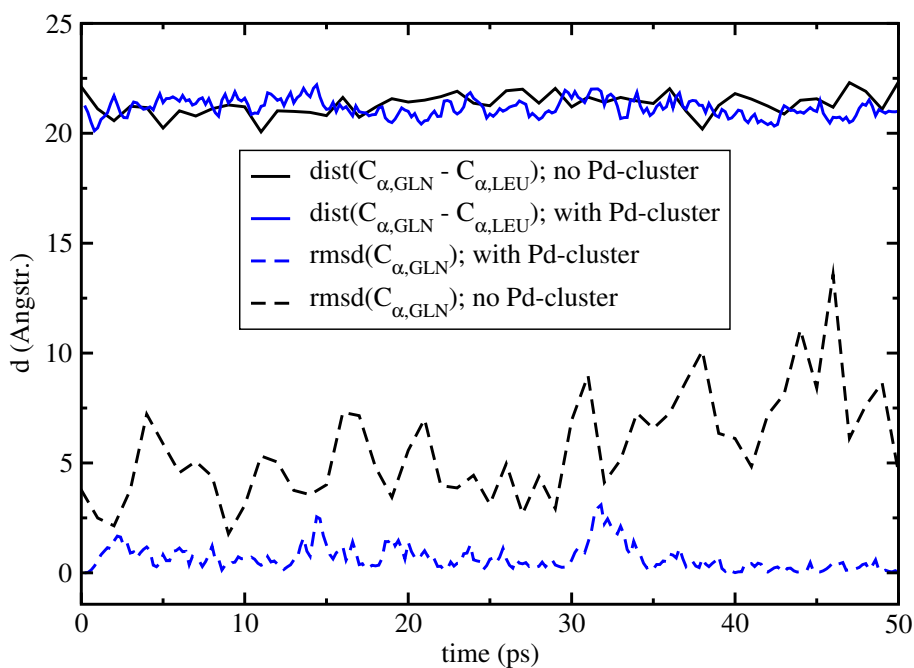
Figure 6.5: *Fluctuation of a single $C_{\alpha,GLN}$ atom (in Gln-23, bottom curves) in a helical region and of the end-to-end distance of helix $C_{\alpha,GLN23}$-$C_{\alpha,LEU37}$ (top curves) in the MD trajectories with (blue) and without (black) the nanoparticle. The nanoparticles-induced reduction in the fluctuations explains the observed increase in the CD signal without a change in the fraction of helical content in the protein.*

Figure 6.4 shows the examined helical length (i.e., distance of $C_{\alpha,Gln}$-$C_{\beta,Leu}$) we have calculated during evolving the system in time at 300 K once with and once without the metal nanoparticle. In agreement with the experimental observations, the overall

secondary-structure and tertiary arrangement is less influenced by the presence of the nanoparticles. However, we find the structural fluctuations of the protein in complex with the nanoparticles are reduced by approximately 28% (fig. 6.5), when compared to the fluctuations of the protein alone. The observed reduction of fluctuations in the complex, akin to a reduced temperature, is commensurate with the observed increase in CD signal. The change in the CD signal can thus be understood as a result of reduced fluctuations in the protein due to the constraints imposed by the presence of the nanoparticle, and not by an actual increase of helical content in the secondary structure.

6.5 Summary

Using combined molecular dynamics plus Monte-Carlo simulations we could demonstrate in agreement with experimental results that the SP1 protein is an template for the synthesis of mono-disperse metal particles of various natures, and the generated particles provide a mortar to construct novel geometrical architectures of hybrid nanoparticle-protein complexes.

We have analyzed the protein structure before and after the palladium ion deposition by evaluating geometrical parameters during the time evolution of the hybrid system in solution under normal ambient conditions. With this information we could interpret the measured CD-spectra and concluded that the protein structure remained intact after particle deposition and, thus, may be further functionalized by genetic engineering with affinity reagents for site-specific targeting.

The high relevance of such kind of systems was also shown in recent experiments, w.t. SP1 accumulates in tumors and shows no significant immune response after repeated injection, indicating that it may indeed be used to target active nanoparticles to solid tumors for both imaging and therapy. Such biofunctional, protein-nanoparticle hybrids will thus be interesting for diverse future applications, such as in biosensing, targeted reagent delivery, site-specific tumor imaging, therapy, and biomedical diagnosis. Multi-scale simulations permit an appealing tool to cover the full range of the various time- and length-scales playing a role for hybrid nanoparticle-protein systems to predict their complex behavior and optimize them for applications.

7 Conclusions

Electronic transport through nano-scale structures has been intensively studied during the last decade. The fabrication of nano-junctions by scanning tunneling microscopy, break-junctions or electrochemical deposition enabled measurements leading to new insights into the physics of electronic transport in quantum systems and to the development of new promising devices for nano-electronics. In molecular electronics measurements one major challenge is the control of the molecular geometry arranged between two or three microscopic electrodes. The difficulty of contacting a molecule increases dramatically with decreasing the size of the scatterer to a few atoms. In the case of large hybrid nano-particles functionalization for printable electronics is obtained only for systems containing ten-thousands of atoms. Theoretical investigations on idealized structures gave understanding of fundamental principles, but since the control of the molecular geometry is experimentally to difficult conformational variability plays an important role. To understand the physics behind their functionality these systems have to be treated on the classical atomistic as well as on the quantum mechanics level permitting the investigation of electronic transport in more realistic systems including disorder and conformational ensembles.

In the present thesis we have studied the interplay of conformational and electronic transport properties in metallic and organic nano-structures. Characterization of the influence of thermal, electrostatic or fabrication-induced structural rearrangement on the conductance characteristics gives new insights into the functionality of nano-scale systems, such as quantum point contacts, nano-wires and nano-particles. With the developed theoretical approach nano-electronical building blocks, e.g., switchable molecules, can be identified and optimized for new promising technological applications.

In order to simulate realistic conformations of nano-structures arising from (electrochemical) fabrication techniques we have developed and implemented a deposition model, which is based on classical interactions, and can be used in simulations of metallic systems, as well as extended organic molecules. In contrast to molecular dynamics simulations our stochastic approach is able simulate growth processes occurring on very long time scales (seconds) which is prohibitively costly for deterministic methods like MD. To study the coherent transport properties of large systems we have implemented a recursive Green's function formalism that employs tight-binding like model Hamiltonians. The linear scaling behavior of the computational effort with the device length permits the treatment of large scattering systems taking extended electrode fragments into account. The developed and validated *methods* were employed in the following *key applications*:

Static disorder in metallic junctions:

First we have studied the ballistic transport properties of ideally crystalline silver nano-junctions using our implementation of the RGF method. In the absence of defects and disorder the conductance is an integer multiple of the conductance quantum G_0 for small minimal cross sections of the nano-contact, which most likely results from the electronic *s*-configuration of the metal. Generalizing the conformations to more realistic structures comparable to experimental situations we investigated the influence of imperfect contact geometries on the conductance by studying many different possible realizations of silver nano-junctions: Starting from a symmetric silver electrode contact we found that tilting the junction electrodes up to 60 degrees reduces the conductance by 20%, while twinning the electrodes leaves the conductance nearly unchanged. Furthermore we found that introducing a large amount of surface vacancies leads to weak variations of the conductance of silver contacts. In the next step we have investigated the transport properties of non-fcc structured silver junctions, silver nano-clusters ranging from 5-260 atoms. Here we found conductance values that confirmed the results of the transport calculations of idealized fcc contact geometries, where we already found a strong dependence of the total conductance on the diameter of the minimal cross section. We noticed that analyzing their transmission function in a three-terminal measurement can be used to estimate the size of the nano-particle, because fluctuations strength of the transmission function is directly proportional to the clusters diameter.

Atomic Transistor:

Secondly, we have investigated mechanical, electrostatic and electronic properties of an „atomic transistor" nano-junction in collaboration with an experimental group. In this experiment a silver nano-junction is electrochemically deposited and „trained" to reproducibly switch between integer values of quantum conductance. In particular, the question of the underlying switching mechanism was not conclusively answered at the start of this investigations. We therefore developed a multi-scale approach combining continuum, atomistic and quantum mechanical methods because of the many different time and length scales playing a role in this experiment. Applying this approach we found that the bistable reconfiguration of the electrode tips is the underlying mechanism of the formation of nano-junctions with predefined levels of quantum conductance. It turns out that these levels are determined by specific, material dependent bistable junction conformations, similar to magic numbers for metal clusters [126]. For silver, the observed quantum conductance levels appear to coincide with integer multiples of the conductance quantum. With our model we could confirm the experimental observation, that at halting the deposition process at a non-integer multiple of G_0, subsequent switching cycles either converge to an integer conductance at a nearby level or destroy the junction. Furthermore the experimentalists found that by snapping into bistable conformations, junctions are mechanically and thermally stable at room temperature for long sequences of switching cycles. We can explain this effect with the „electrode-training-effect" occurring in our model at repeated switching of the electrode conformation, which increases the bistability of the tip reconstruction with every switch-

ing cycle. We have also analyzed the influence of the dielectric double layer in atomic transistor conformations generated by the electrolyte and find, that this electrochemical environment leads to an additional stabilization of the switching process. Another effect we could explain is the observed switching between levels of finite conductance: The occurrence of metastable contact conformations at integer quantum conductance gives rise to plateaus in the conductance curve at a complete rupture of the contact. These plateaus are selected during inter-level switching. Furthermore, using our model calculations we can relate the weak conductance fluctuations at non-integer conductance values observed in the experiment to thermally induced single atom hopping between two neighboring stable energy-minima.

Conformational disorder in organic wires:

In the third part of this thesis we have applied the recursive Green's function technique to study organic nano-wires and obtained reasonable agreement with results of higher level theories for the total transmission function as well as for length-dependence of the conductance. Since we divide the extended molecule region into principal layers with nearest neighbor coupling (or mathematically spoken, we truncate the Hamilton matrix) this result is not obvious. Furthermore we have investigated the impact of thermally induced large-scale geometric change on the conductance. We combined classical molecular dynamics calculations at room temperature with a quantum model Hamiltonian approach to calculate the conductance of the nano-wire. During the simulation we find temporal conductance fluctuations of more than an order of magnitude, leading to high-conductivity conformations that are sterically unfavorable at zero temperature. The average conductance of these conformations explains the experimentally observed value very well, because disorder effects on the conductance of molecular wires play an important role in almost all experimental realizations.

The extensive experimental effort directed towards charge transport in organic nano-wires, and the versatile amount of open questions in that area, have motivated our studies of the relation between structural, electronic and transport properties of oligo-phenyleneimine wires. Using density functional theory we found that, in contrast to the oligo-phenylene wires, the two types of energy barriers of the dihedral angle rotations are lower than 16 meV, thus we can conclude that room temperature is already sufficient to induce full rotations of the molecular ring units. Furthermore we could deduce from our calculations that the charge carrying frontier orbitals are not extend over the entire wire - the electronic delocalization is limited to 3-4 repeating ring units, which explains the experimentally observed disruption of the coherent transport in longer wires. In addition we find for the length dependence of the conductance the characteristic exponential decay with a decay parameter $\beta = 3.29$ nm^{-1}, which agrees well with the experimental findings and confirms, that the molecular geometry obtained from density functional theory, in particular dihedral angles, is close to the true structure.

Growth of palladium nano-particles in protein templates:

The last part of this work describes our investigations of hybrid protein-palladium nano-particles which may have promising applications in novel nano-technology based flash-memory devices as well as in cancer therapy. After the experimental success of the palladium nanoparticle synthesis using functionalized protein templates several questions arose. From the perspective of applications it is important to know whether the nanoparticle grows into a porous structure induced by the presence of the protein or forms on the outside of the protein and can grow into a compact cluster. In addition, it was unclear how the presence of the palladium cluster affects the structure of the protein SP1, which is essential for future applications of such a hybrid system. Using combined molecular dynamics plus Monte-Carlo simulations we have analyzed the protein structure before and after the palladium ion deposition. Simulating the protein's structure in explicit water molecules (in total about 100.000 atoms), with molecular dynamics we obtain a ring-shaped macro-molecule with an outer diameter of 10 nm with helical substructures. Our nanoparticle growth simulation of the palladium suggest that the nanoparticle grows as a a compact polycrystalline metal cluster coupling via histidine residues to the protein. On this basis additional simulations permitted the interpretation of the measured CD-spectra: We could conclude that the protein structure remained intact after particle deposition and, thus, may be further functionalized by genetic engineering with affinity reagents for site-specific targeting.

The present work showed, that conformational properties significantly affect coherent quantum conductance. To explain transport measurements and optimize functionalized nano-structures it is indispensable to consider sufficiently large extended molecule regions in realistic arrangement. In this work we discussed the influence of disorder effects, which definitely occur in realistic systems and can, in certain applications, dominate the conductivity. For this purpose the multi-scale approach pursued here provides a powerful method to consider the physics of various time and length scales at a reasonable amount of computational costs, which will permit treatment of many further applications in the growing field of nanoscience.

Bibliography

[1] J. D. Jonathan and D. Wales, Global Minima for Transition Metal Clusters Described by Sutton-Chen Potentials, New J. Chem. **22**, 733 (1998).

[2] G. Moore, Cramming more components sonto integrated circuits, Magazine Electronics **38**, 8 (1965).

[3] P. Ball, A switch in time, Nature **445**, 362 (2007).

[4] J. R. Heath and M. A. Ratner, Molecular Electronics, Physics Today **25**, 43 (2003).

[5] *Defects and faults in quantum cellular automata at nano scale* (IEEE Computer Society, Washington, DC, USA, 2004).

[6] C. P. Collier, E. W. Wong, M. Belohradsky, F. M. Raymo, J. F. Stoddart, P. J. Kuekes *et al.*, Electronically Configurable Molecular-Based Logic Gates, Science **289**, 1172 (2000).

[7] A. Bachold, P. Hadley, T. Nakanishi and C. Dekker, DNA-Templated Carbon Nanotube Field-Effect Transistor, Science **294**, 1317 (2001).

[8] J. R. Heath, Molecular Electronics, Annu. Rev. Mater. Res. **39**, 1 (2009).

[9] A. Nitzan and M. A. Ratner, Electron Transport in Molecular Wire Junctions, Science **300**, 1384 (2003).

[10] K. S. Thygesen and K. W. Jacobsen, Four-atom period in the conduction of monatomic al wires, Phys. Rev. Lett. **91**, 146801 (2003).

[11] M. Strange, I. S. Kristensen, K. S. Thygesen and K. W. Jacobsen, Benchmark density functional theory calculations for nanoscale conductance, J. Chem. Phys. **128**, 114714 (2008).

[12] S. Datta, *Electronic Transport in Mesoscopic Systems* (Unversity of Cambridge, England, 1997).

[13] P. Damle, A. W. Ghosh and S. Datta, First-principles analysis of molecular conduction using quantum chemistry software, Chem. Phys. **281**, 171 (2002).

[14] M. Born and R. Oppenheimer, Zur Quantentheorie der Molekeln, Ann. d. Physik **84**, 457 (1927).

[15] M. Born, Theoretical investiagations on the relation between crystal dynamics and x-ray scattering, Rep. Progr. Physics **9**, 294 (1943).

[16] B. J. Alder and T. E. Wainwright, Phase Transition for a Hard Sphere System, J. Chem. Phys. **27**, 1208 (1957).

[17] B. J. Alder and T. E. Wainwright, Studies in molecular dynamics. I. General method., J. Chem. Phys. **31**, 459 (1959).

[18] A. Rahman, Correlations in the Motion of Atoms in Liquid Argon, Phys. Rev. A **136**, 405 (1964).

[19] J. A. McCammon, B. R. Gelin and M. Karplus, Molecular Dynamics Study of the Bovine Pancreatic Trypsin Inhibitor, Nature **267**, 585 (1977).

[20] M. P. Allen and D. J. Tildesley, *Computer Simulation in Chemical Physics* (Klumer Academic Publishers, Dortrecht, 1993).

[21] M. Karttunen and A. Lukkarien, *Novel Methods of Soft Matter Simulations* (Springer, Berlin, 2004).

[22] R. Car and M. Parrinello, Unified Approach for Molecular Dynamics and Density-Functional Theory, Phys. Rev. Lett. **55**, 2471 (1985).

[23] S. Blügel, G. Gompper, E. Koch, H. Müller-Krumbhaar, R. Spatschek and R. G. Winkler, *Computational Condensed Matter Physics* (Forschungszentrum Jülich, 2006).

[24] H. Risken, *The Fokker-Planck Equation* (Springer, Berlin, 1989).

[25] H. C. Andersen, Molecular Dynamics Simulations at Constant Pressure and/or Temperature, J. Chem. Phys. **72**, 2384 (1980).

[26] S. Nosé, A unified formulation of the constant-temperature molecular dynamics methods, J. Chem. Phys. **81**, 511 (1984).

[27] S. Nosé, A molecular dynamics method for simulations in the canonical ensemble, Mol. Phys. **52**, 255 (1984).

[28] W. G. Hoover, Canonical dynamics: Equilibrium phase-space distributions, Phys. Rev. A **31**, 1695 (1985).

[29] S. Nosé, An Improved Symplectic Integrator for Nosé-Poincaré Thermostat, J. Phys. Soc. **70**, 75 (2001).

[30] M. Griebel, S. Knapek, G. Zumbusch and A. Caglar, *Numerische Simulation in der Moleküldynamik* (Springer, Berlin, 2004).

[31] N. Metropolis, A. Rosenbluth, M. Rosenbluth, H. Teller and E. Teller, Equation of state calculations by fast computing machines, J. Chem. Phys. **21**, 1087 (1953).

[32] K. Binder, *Monte Carlo Methods in Statistical Physics* (Springer, Berlin, 1979).

[33] M. P. Allen and D. J. Tildesley, *Computer simulations of liquids* (Clarendon, Oxford, 1987).

[34] K. Binder and D. W. Heermann, *Monte Carlo simultion in statistical physics* (Springer, Berlin, 1992).

[35] D. Frenkel and B. Smith, *Understanding Molecular Simulation* (Academic Press San Diego, 1996).

[36] D. P. Landau and K. Binder, *A guide to Monte Carlo simulations in statistical physics* (Cambridge University Press, 2000).

[37] A. P. J. Jansen, An Introduction to Monte Carlo Simulations of Surface Reactions, arXiv:cond-mat/0303028v1 (2008).

[38] E. Martinez, J. Marian, M. H. Kalos and J. M. Perlado, Synchronous parallel kinetic Monte Carlo for continuum diffusion-reaction systems, Journal of Computational Physics **227** (2008).

[39] P. Leyton, J. S. Gomez-Jeria, S. Sanchez-Cortes, C. Domingo and M. Campos-Vallette, Carbon Nanotube Bundles as Molecular Assemblies for the Detection of Polycyclic Aromatic Hydrocarbons: Surface-Enhanced Resonance Raman Spectroscopy and Theoretical Studies, J. Phys. Chem. B **110**, 6470 (2006).

[40] V. Rodrigues, J. Bettini, A. R. Rocha, L. G. C. Rego and D. Ugarte, Quantum conductance in silver nanowires: Correlation between atomic structure and transport properties, Phys. Rev. B **65**, 153402 (2002).

[41] L. G. C. Rego, A. R. Rocha, V. Rodrigues and D. Ugarte, Role of structural evolution in the quantum conductance behavior of gold nanowires during stretching, Phys. Rev. B **67**, 045412 (2003).

[42] R. Hoffmann, An Extended Hückel Theory. I. Hydrocarbons, J. Chem. Phys. **39**, 1397 (1963).

[43] M. Wolfsberg and L. J. Helmholz, The Spectra and Electronic Structure of the Tetrahedral Ions MnO_4^-, CrO_4^-, and ClO_4^-, J. Chem. Phys. **20**, 837 (1952).

[44] J. P. Lowe, *Quantum Chemistry* (Academic Press: New York, 1978).

[45] I. I. Guseinov and B. A. Mamedov, On the calculation of arbitrary multielectron molecular integrals over Slater-type orbitals using recurrence relations for overlap integrals. II. Two-center expansion method, Int. J. Quantum Chem. **81**, 117 (2001).

[46] S. Boys, Electronic wavefunctions. I. A general method of calculation for stationary states of any molecular system., Proc. Roy. Soc. A **200**, 542 (1950).

[47] W. Kutzelnigg, *Einführung in die Theoretische Chemie, Band 2* (VCH, Weinheim, 1994).

[48] D. C. Young, *Computational Chemistry* (Wiley-Interscience, New York, 2001).

[49] M. S. Jhon, U. Cho, L. B. Kier and H. Eyring, Molecular Orbital Studies of Ethylenediamine Conformations, PNAS **69**, 121 (1972).

[50] E. Lindholm and J. Li, Energies of Cr Orbitals from Extended Huckel Calculations in Combination wlth HAM, J. Phys. Chem. **92**, 1731 (1988).

[51] F. Pauly, J. K. Viljas, J. C. Cuevas and G. Schön, Density-functional study of tilt-angle and temperature-dependent conductance in biphenyl dithiol single-molecule junctions, Phys. Rev. B **77**, 155312 (2008).

[52] W. Thiel, Perspectives on Semiempirical Molecular Orbital Theory, Adv. Chem. Phys. **93**, 703 (1996).

[53] J. Pople and D. Beveridge, *Approximate molecular orbital theory* (McGraw-Hill New York, 1970).

[54] J. A. Pople and G. A. Segal, Approximate Self-Consistent Molecular Orbital Theory. II. Calculations with Complete Neglect of Differential Overlap, J. Chem. Phys. **43**, S136 (1965).

[55] L. H. Thomas, Calculation of atomic fields, Proc. Cambridge Philos. Soc. **23**, 542 (1927).

[56] E. Fermi, Un methodo statistico par la determinazione di alcune proprietá, Atti Accad, Naz. Lincei, Cl. Sci. Fis. Mat. Nat. Rend. **6**, 602 (1927).

[57] P. Hohenberg and W. Kohn, Inhomogeneous Electron Gas, Phys. Rev. B **136**, B864 (1964).

[58] M. Levy, Universal variational functionals of electron densities, first-order density matrices, and natural spin-orbitals and solution of the v-representability problem, Proc. Natl. Acad. Sci. U. S. A. **76**, 6062 (1979).

[59] W. Kohn and L. J. Sham, Self-Consistent Equations Including Exchange and Correlation Effects, Phys. Rev. **140**, A1133 (1965).

[60] S. H. Vosko, L. Wilk and M. Nusair, Accurate spin-dependent electron liquid correlation energies for local spin density calculations: a critical analysis, Can. J. Phys. **58**, 1200 (1980).

[61] J. P. Perdew and A. Zunger, Self-interaction correction to density-functional approximations for many-electron systems, Phys. Rev. B **23**, 5048 (1981).

[62] J. P. Perdew, J. A. Chevary, S. H. Vosko, K. A. Jackson, M. R. Pederson, D. J. Singh *et al.*, Atoms, molecules, solids and surfaces: Applications of the generalized gradient approximation for exchange and correlation, Phys. Rev. B **46**, 6671 (1992).

[63] J. P. Perdew, J. A. Chevary, S. H. Vosko, K. A. Jackson, M. R. Pederson, D. J. Singh *et al.*, Erratum: Atoms, molecules, solids, and surfaces: Applications of the generalized gradient approximation for exchange and correlation, Phys. Rev. B **48**, 4978 (1993).

[64] J. P. Perdew, K. Burke and M. Ernzerhof, Generalized gradient approximation made simple, Phys. Rev. Lett. **77**, 3865 (1996).

[65] A. D. Becke, A new mixing of Hartree-Fock and local density-functional theories, J. Chem. Phys. **98**, 1372 (1993).

[66] J. Harris and R. Jones, Correlation energy and van der Waals interaction of coupled metal films, J. Phys. F **4**, 1170 (1974).

[67] D. C. Langreth and J. P. Perdew, The Exchange Correlation Energy of a Metallic Surface, Solid State Commun. **17**, 1425 (1975).

[68] O. Gunnarsson and B. I. Lundqvist, Exchange and correlation in atoms, molecules, and solids by the spin-density-functional formalism, Phys. Rev. B **10**, 4274 (1976).

[69] P. H. Dederichs, S. Bügel, R. Zeller and H. Akai, Ground States of Constrained Systems: Application to Cerium Impurities, Phys. Rev. Lett. **53**, 2512 (1984).

[70] A. Oswald, R. Zeller and P. H. Dederichs, nteraction of local moments in Cu, J. Magn. Magn. Matter **54**, 1247 (1986).

[71] J. Heurich, J. C. Cuevas, W. Wenzel and G. Schön, Electrical Transport through Single-Molecule Junctions: From Molecular Orbitals to Conduction Channels, Phys. Rev. Lett. **88**, 256803 (2002).

[72] J. C. Cuevas, A. L. Yeyati, A. Matrin-Rodero, G. R. Bollinger, C. Untiedt and N. Agrait, Evolution of Conducting Channels in Metallic Atomic Contacts under Elastic Deformation, Phys. Rev. Lett. **81**, 2990 (1998).

[73] B. J. v. Wees, H. v. Houten, C. W. J. Beanakker, j. G. Williamson, L. P. Kouwenhoven, D. v. d. Marel *et al.*, Quantized conductance of point contacts in a two-dimensional electron gas, Phys. Rev. Lett. **60**, 848 (1988).

[74] D. A. Wharam, M. Pepper, H. Ahmed, J. E. Frost, G. D. Hasko, D. C. Peacock *et al.*, One-dimensional transport and the quantisation of the ballistic resistance, J. Phys. C **21**, L887 (1988).

[75] C. Cohen-Tannoudji, *Quantenmechanik Bd.2* (Walter de Gruyter, Berlin, 1999).

[76] D. S. Fisher and P. A. Lee, Relation between conductivity and transmission matrix, Phys. Rev. B **23**, 6851 (1981).

[77] G. Czycholl, *Theoretische Festkörperphysik* (Vieweg Verlag, 2000).

[78] A. Kletsov, Y. Dahnovsky and J. V. Ortiz, Surface Green's function calculations: A nonrecursive scheme with an infinite number of principal layers, The Journal of Chemical Physics **126**, 134105 (2007).

[79] A. Kletsov and Y. Dahnovsky, Surface Green functions in molecular transport junctions: Generalization to interacting electrons in the leads, Physical Review B (Condensed Matter and Materials Physics) **76**, 035304 (2007).

[80] P. M. Morse and H. Feshbach, *Methods of Theoretical Physics* (McGraw-Hill, New York, 1953).

[81] J. A. Vergés, Computational implenentation of the Kubo formula for the static conductance: application to two-dimensional quantum dots, Comp. Phys. Commun. **118**, 71 (1999).

[82] F. Pauly, M. Dreher, J. K. Viljas, M. Häfner, J. C. Cuevas and P. Nielaba, Theoretical analysis of the conductance histograms and structural properties of Ag, Pt, and Ni nanocontacts, Phys. Rev. B **74**, 235106 (2006).

[83] F. D. Novaes, A. J. R. da Silva, E. Z. da Silva and A. Fazzio, Oxygen Clamps in Gold Nanowires, Phys. Rev. Lett. **96**, 016104 (2006).

[84] X. Guang-Can, Novel Organically Templated 2-D Silver(I)-Iodide Coordination Architecture: Syntheses and Characterization, J. Cluster Science **17**, 457 (2006).

[85] X. Qian, J. Li, X. Lin and S. Yip, Time-dependent density functional theory with ultrasoft pseudopotentials: Real-time electron propagation across a molecular junction, Phys. Rev. B **73**, 035408 (2006).

[86] N. Agrait, A. L. Yeyati and J. M. van Ruitenbeek, Quantum proprties of atomic-sized conductors, Phys. Rep. **377**, 81 (2003).

[87] J. M. Krans, J. M. van Ruitenbeek, V. V. Fisun, I. K. Yanson and L. . J. de Jongh, The signature of conductance quantization in metallic point contacts, Nature **375**, 767 (1995).

[88] E. Scheer, N. Agrait, J. C. Cuevas, A. L. Yeyati, B. Ludoph, A. Martín-Rodero *et al.*, The signature of chemical valence in the electrical conduction through a single-atom contact, Nature **394**, 154 (1998).

[89] C. Z. Li and N. J. Tao, Quantum Transport in Metallic Nanowires Fabricated by Electrochemical Deposition/Dissolution, Appl. Phys. Lett **72**, 894 (1998).

[90] F. Morpurgo, C. M. Marcus and D. B. Robinson, Controlled fabrication of metallic electrodes with atomic separation, Appl. Phys. Lett. **74**, 2084 (1999).

[91] Z. Li, H. X. He and N. J. Tao, Quantized tunneling current in the metallic nanogaps formed by electrodeposition and etching, Appl. Phys. Lett. **77**, 3995 (2000).

[92] F.-Q. Xie, L. Nittler, C. Obermair and T. Schimmel, Gate-Controlled Atomic Quantum Switch, Phys. Rev. Lett. **93**, 128303 (2004).

[93] F.-Q. Xie, C. Obermair and T. Schimmel, Switching an Electrical Current with Atoms: the Reproducible Operation of a Multi-Atom Relay, Solid State Commun. **132**, 437 (2004).

[94] P. Konrad, C.Bacca, E. Scheer, P.Brenner, A. Mayer-Gindner and H. v. Löhneysen, Stable single-atom contacts of zinc whiskers, Appl. Phys. Lett **86**, 213115 (2005).

[95] M. Brandbyge, K. W. Jacobsen and J. K. Norskov, Scattering and conductance quantization in three-dimensional metal nanocontacts, Phys. Rev. B **55**, 2637 (1997).

[96] C. Yannouleas, E. N. Bogachek and U. Landman, Energetics, forces, and quantized conductance in jellium-modeled metallic nanowires, Phys. Rev. B **57**, 4872 (1998).

[97] L. Gmelin, *Gmelin's Handbook of Inorganic Chemistry* (Chemie, Weinheim, 1973).

[98] F. Pauly, *Phase-coherent electron transport through metallic atomic-sized contacts and organic molecules*, Dissertation, Universität Karlsruhe (TH) (2007).

[99] F.-Q. Xie, R. Maul, S. Brendelberger, C. Obermair, E. B. Starikov, W. Wenzel *et al.*, Preselectable integer quantum conductance of electrochemically fabricated silver point contacts, App. Phys. Lett. **93**, 043103 (2008).

[100] F.-Q. Xie, R. Maul, A. Augenstein, C. Obermair, E. Starikov, G. Schön *et al.*, Independently switchable atomic quantum transistors by reversible contact reconstruction, Nano Lett. **8**, 4493 (2008).

[101] X. Shao, X. Yang and W. Cai, Geometry optimization and structural distribution of silver clusters from Ag170 to Ag310, Chem. Phys. Lett. **460**, 315 (2008).

[102] F. Baletto and R. Ferrando, Structural properties of nanoclusters: Energetic, thermodynamic, and kinetic effects, Rev. Mod. Phys. **77**, 371 (2005).

[103] N. Agrait, J. G. Rodrigo and S. Vieira, Conductance steps and quantization in atomic-size contacts, Phys. Rev. **47**, 12345 (1993).

[104] D. P. E. Smith, Quantum Point Contact Switche, Science **269**, 371 (1995).

[105] K. Terabe, T. Hasegawa, T. Nakayama and M. Aono, Quantized conductance atomic switch, Nature **433**, 47 (2005).

[106] A. Sokolov, C. Zhang, E. Y. Tsymbal, J. Redepenning and B. Doudin, Quantized magneto-resistance in atomic-size contacts, Nature Nanotechnology **2**, 171 (2007).

[107] W. H. C.Z. Li, A. Bogozi and N. J. Tao, Fabrication of Stable Metallic Nanowires with Quantized Conductance, Nanotechnology **10**, 221 (1999).

[108] A. I. Mares and J. M. van Ruitenbeek, Observation of shell effects in nanowires for the noble metals Cu, Ag, and Au, Phys. Rev. B **72**, 205402 (2005).

[109] M. Dreher, F. Pauly, J. Heurich, J. C. Cuevas, E. Scheer and P. Nielaba, Structure and conductance histogram of atomic-sized Au contacts, Phys. Rev. B **72**, 075435 (2005).

[110] E. Tosatti, S. Prestipino, S. Kostlmeier, A. D. Corso and F. D. D. Tolla, String Tension and Stability of Magic Tip-Suspended Nanowires, Science **291**, 288 (2001).

[111] I. K. Yanson, Y. G. Naidyuk, D. L. Bashlakov, V. V. Fisun, O. P. Balkashin, V. Korenivski *et al.*, Spectroscopy of Phonons and Spin Torques in Magnetic Point Contacts, Phys. Rev. Lett. **95**, 186602 (2005).

[112] A. I. Yanson, I. K. Yanson and J. M. van Ruitenbeek, Crossover from Electronic to Atomic Shell Structure in Alkali Metal Nanowires, Phys. Rev. Lett. **87**, 216805 (2001).

[113] J. J. Kwiatkowski, J. Nelson, H. Li, J. L. Bredas, W. Wenzel and C. Lennartz, Simulating charge transport in tris(8-hydroxyquinoline) aluminium (Alq3), Phys Chem. Chem. Phys. **10**, 1852 (2008).

[114] A. Tveito and R. Winther, *Einführung in partielle Diffentialgleichungen. Ein numerischer Zugang* (Springer, Berlin, 2005).

[115] X. Shao, X. Liu and W. Cai, Structural optimization of silver clusters up to 80 atoms with Gupta and Sutton-Chen potential, J. Chem. Theory Comput. **1**, 762 (2005).

[116] J. Weissmueller, R. N. Viswanath, D. Kramer, P. Zimmer, R. Wurschum and H. Gleiter, Charge-Induced Reversible Strain in a Metal, Science **300**, 312 (2003).

[117] F. Weigend, F. Evers and J. Weissmueller, Structural relaxation in charged metal surfaces and cluster ions. (2006), Small **2**, 1497 (2006).

[118] J. E. Inglesfield, Reconstructions and relaxations on metal surfaces, Prog. Surf. Sci. **20**, 105 (1985).

[119] Y. Xue, S. Datta and M. Ratner, First-principles based matrix Green's function approach to molecular electronic devices: General formalism, Chem. Phys. **281**, 151 (2002).

[120] H. van Zalinge, A. Bates, D. J. Schiffrin, E. B. Starikov, W. Wenzel and R. J. Nichols., In-situ variable temperature measurements of the single molecule conductance of double stranded DNA, Angew. Chemie **45**, 5499 (2006).

[121] R. Maul and W. Wenzel, Influence of structural disorder and large-scale geometric fluctuations on the coherent transport of metallic junctions and molecular wires, Phys. Rev. B **80**, 045424 (2009).

[122] E. B. Starikov, S. Tanaka, N. Kurita, Y. Sengoku, T. Natsume and W. Wenzel, Investigation of a Kubo-formula-based approach to estimate DNA conductance in an atomistic model., Eur. Phys. J. E **18**, 437 (2005).

[123] N. T. Wilson and R. L. Johnston, A theoretical study of atom ordering in copper-gold nanoalloy clusters, J. Mater. Chem. **12**, 2913 (2002).

[124] A. Ohiso, Y. Sugimoto, M. Abe and S. Morita, Tip-induced Local Reconstruction on the Pb/Ge(111) Surface Using Frequency Modulation Atomic Force Microscopy, Jpn. J. Appl. Phys. **46**, 5582 (2007).

[125] M. Ternes, C. P. Lutz, C. F. Hirjibehedin, F. J. Giessibl and A. J. Heinrich, The Force Needed to Move an Atom on a Surface, Science **316**, 1066 (2008).

[126] M. N. Huda, M. K. Niranjan, B. R. Sahu and L. Kleinman, Effect of spin-orbit coupling on small platinum nanoclusters, Phys. Rev. A **73**, 053201 (2006).

[127] C. Obermair, *Nanostrukturierung mittels Rasterkraftmikroskopie und Elektrochemie*, Dissertation, Universität Karlsruhe (TH) (2005).

[128] M. S. Kilic and M. Z. Bazant, Steric effects in the dynamics of electrolytes at large applied voltages. I. Double-layer charging, Phys. Rev. E **75**, 021502 (2007).

[129] P. G. Collins, M. S. Arnold and P. Avouris, Engineering Carbon Nanotubes and Nanotube Circuits Using Electrical Breakdown, Science **27**, 706 (2001).

[130] A. Bachtold, P. Hadley, T. Nakanishi and C. Dekker, Logic Circuits with Carbon Nanotube Transistors, Science **294**, 1317 (2001).

[131] D. J. Wold, R. Haag, M. A. Rampi and C. D. Frisbie, Distance Dependence of Electron Tunneling through Self-Assembled Monolayers Measured by Conducting Probe Atomic Force Microscopy: Unsaturated versus Saturated Molecular Junctions, J. Phys. Chem. B **106**, 2813 (2002).

[132] S. H. Choi, B. Kim and D. Frisbie, Electrical resistance of long conjugated molecular wires, Science **320**, 1482 (2008).

[133] W. Hu, J. Jiang, H. Nakashima, Y. Luo, Y. Kashimura, K.-Q. Chen *et al.*, Electron Transport in Self-Assembled Polymer Molecular Junctions, Phys. Rev. Lett. **96**, 027801 (2006).

[134] S. Kubatkin, A. Danilov, M. Hjort, J. Cornil, J. Bredas, N. Stuhr-Hansen *et al.*, Single Electron Transport Through a Single Conjugated Molecule Visiting Several Redox States, Nature **425**, 698 (2003).

[135] Y. Selzer, M. A. Cabassi and D. L. A. T. S. Mayer, Temperature effects on molecular conduction, J. Am. Chem. Soc. **126**, 4052 (2004).

[136] S. Y., L. Cai, M. A. Cabassi, Y. Yao, J. M. Tour, T. S. Mayer *et al.*, The Effect of Local Environment on Molecular Conduction: Isolated Molecule versus Self-Assembled Monolayer, Nano Lett. **5**, 61 (2005).

[137] F. Evers, F. Weigend and M. Koentopp, Conductance of molecular wires and transport calculations based on density-functional theory, Phys. Rev. B **69**, 235411 (2004).

[138] H. Kondo, H. Kino, J. Nara, T. Ozaki and T. Ohno, Contact-structure dependence of transport properties of a single organic molecule between Au electrodes, Phys. Rev. B **73**, 235323 (2006).

[139] J. Tomfohr and O. F. Sankey, Theoretical analysis of electron transport through organic molecules., J. Chem. Phys **120**, 1542 (2004).

[140] E. G. Emberly and G. Kirczenow, The Smallest Molecular Switch, Phys. Rev. Lett. **91**, 188301 (2003).

[141] M. A. Reed, C. Zhou, C. J. Muller, T. P. Burgin and J. M. Tour, Conductance of a Molecular Junction., Science **278**, 252 (1997).

[142] K. Varga and S. T. Pantelides, Quantum Transport in Molecules and Nanotube Devices, Phys. Rev. Lett. **98**, 076804 (2007).

[143] M. Di Ventra, S. T. Pantelides and N. D. Lang, First-Principles Calculation of Transport Properties of a Molecular Device, Phys. Rev. Lett. **84**, 979 (2000).

[144] R. Ahlrichs, M. Bär, M. Häser, H. Horn and C. Kölme, Electronic structure calculations on workstation computers: The program system turbomole, Chem. Phys. Lett. **162**, 165 (1989).

[145] S. Wohlthat, F. Pauly, J. K. Viljas, J. C. Cuevas and G. Schön, Ab initio study of charge transport through single oxygen molecules in atomic aluminum contacts, Phys. Rev. B **76**, 075413 (2007).

[146] J. K. Viljas, F. Pauly and J. C. Cuevas, Modeling elastic and photoassisted transport in organic molecular wires: Length dependence and current-voltage characteristics, Phys. Rev. B **77**, 155119 (2008).

[147] S. Wakamatsu, S. Fujii, U. Akiba and M. Fujihara, Length dependence of tunneling current through single phenylene oligomers measured by scanning tunneling microscopy at low temperature, Jpn. J. Appl. Phys. **45**, 2736 (2006).

[148] L. Venkataraman, J. E. Klare, M. S. Hybertsen and M. L. Steigerwald, Dependence of single-molecule junction conductance on molecular conformation, Nature **442**, 904 (2006).

[149] F. Pauly, J. K. Viljas and J. C. Cuevas, Length-dependent conductance and thermopower in single-molecule junctions of dithiolated oligophenylene derivatives: A density functional study, Phys. Rev. B **78**, 035315 (2008).

[150] D. A. Case, T. E. Cheatham, T. Darden, H. Gohlke, R. Luo, K. M. Merz *et al.*, The Amber Biomolecular Simulation Programs, J. Comput. Chem. **26**, 1668 (2005).

[151] Hellmann, *Einführung in die Quantenchemie* (Deuticke, Leipzig, 1937).

[152] R. P. Feynman, Forces in Molecules, Physical Review **56**, 340 (1939).

[153] J. M. Tour, I. Jones, L., D. L. Pearson, J. S. Lamba, T. P. Burgin, G. W. Whitesides *et al.*, Self-Assembled Monolayers and Multilayers of Conjugated Thiols, a,w-Dithiols, and Thioacetyl-Containing Adsorbates. Understanding Attachments Between Potential Molecular Wires and Gold Surfaces, J. Am. Chem. Soc. **117**, 9529 (1995).

[154] M. Barnett, Z. Keshavarz, A. Beer and D. Atwell, Influence of grain size on the compressive deformation of wrought Mg_3Al_1Zn, Acta Materialia **52**, 5093 (2004).

[155] S. Behrens, Synthesis of Inorganic Nanomaterials Mediated by Protein-Assemblies, J. Mater. Chem. **18**, 3788 (2008).

[156] T. Ueno, M. Suzuki, T. Goto, T. Matsumoto, K. Nagayama and Y. Watanabe, Size Selective Olefin Hydrogenation by a Pd Nanocluster Provided in the Apo-Ferritin Cage, Angew. Chem. Int. Ed. **43**, 2527 (2004).

[157] S. Mark, M. Berkvist, X. Yang, L. Teixeira and P. Bhatnagar, Bionanofabrication of Metallic and Semiconductor Nanoparticle Arrays Using S-Layer Protein Lattices with Different Lateral Spacings and Geometries, Langmuir **22**, 3763 (2006).

[158] S. Behrens, W. Habicht, K. Wagner and E. Unger, Assembly of nanoparticle ring structures based on protein templates, Adv. Mater. **18**, 284 (2006).

[159] S. Behrens, J. Wu, W. Habicht and E. Unger, Silver nanoparticle and nanowire formation by microtubule templates, Chem. Mater. **16**, 3085 (2004).

[160] S. Behrens, J. Wu, W. Habicht and E. Unger, Nanoparticle Ring Structures based on Protein Assemblies, Surf. Interface Anal. **38**, 1014 (2006).

[161] R. Bekeredjian, S. Behrens, J. Ruef, E. Dinjus, E. Unger, M. Baum *et al.*, Ultrasound in Biology and Medicine, Ultrasound in Med. and Biol. **28**, 691 (2002).

[162] M. Klem, D. Willits, D. Solis, A. Belcher, M. Young and T. Douglas, Bio-inspired Synthesis of Protein-Encapsulated CoPt Nanoparticles, Adv. Funct. Mater. **15**, 1489 (2005).

[163] R. McMillan, J. Howard, N. Zaluzec, H. Kagawa, R. Mogul, Y. F. Li *et al.*, A Self-Assembling Protein Template for Constrained. Synthesis and Patterning of Nanoparticle Arrays, J. Am. Chem. Soc. **127**, 2800 (2005).

[164] Z. Varpness, J. Peters, M. Young and T. Douglas, Biomimetic synthesis of a H_2 catalyst using a protein cage architecture, Nano Lett. **5**, 2306 (2005).

[165] S. Tang, C. Mao, Y. Liu, D. Kelly and S. Banerjee, Vertical Flash memory devices with Protein-assembled Nanocrystal floating gate and A1$_2$O$_3$ control oxide, IEEE Trans. Electron Devices **54**, 433 (2007).

[166] W. X. Wang, D. Pelah, T. Alergand, O. Shoseyov and A. Altman, Characterization of SP1, a Stress-Responsive, Boiling-Soluble, Homo-Oligomeric Protein from Aspen, Plant Physiol. **130**, 865 (2002).

[167] W. Wang, O. Dgany, O. Dym, A. Altman, O. Shoseyov and O. Almog, Crystallization and preliminary X-ray crystallographic analysis of SP1, a novel chaperone-like protein, Acta Crystallogr. Sect. D **59**, 512 (2003).

[168] O. Dgany, A. Gonzalez, O. Sofer, W. Wang, G. Zolotnitsky, A. Wolf *et al.*, The structural basis of the thermostability of SP1, a novel plant (Populus tremula) boiling stable protein, J. Biol. Chem. **279**, 51516 (2004).

[169] I. Medalsy, O. Dgany, M. Sowwan, H. Cohen, A. Yukashevska, S. G. Wolf *et al.*, SP1 Protein Based Nanostructures and Arrays, Nano Lett. **8**, 473 (2008).

[170] S. Behrens, K. Rahn, W. Habicht, K. J. Boehm, H. Roesner, E. Dinjus *et al.*, Nanoscale particle arrays induced by highly ordered protein assemblies, Adv. Mater. **14**, 1621 (2002).

[171] L. C. Ciacchi, M. Mertig, R. Seidel, W. Pompe and A. D. Vito, Nucleation of Platinum Clusters on Biopolymers: a First Principles Study of the Molecular Mechanisms, Nanotechnology **14**, 840 (2003).

Acknowledgements

List of publications

1. **R. Maul**, *Ab-initio-Untersuchungen der Aminosären Glycin, Alanin und Cystein*, diploma thesis, Institut für Festkörpertheorie und -optik, Friedrich-Schiller-Universität Jena (2006).

2. **R. Maul**, F. Ortmann, M. Preuss, K. Hannewald, and F. Bechstedt, *DFT Studies Using Supercells and Projector-Augmented Waves for Structure, Energetics, and Dynamics of Glycine, Alanine, and Cysteine*, J. Phys. Chem. A **111**, 4370 (2007)

3. **R. Maul**, M. Preuss, F. Ortmann, K. Hannewald, and F. Bechstedt, *Electronic Excitations of Glycine, Alanine, and Cysteine Conformers from First-Principles Calculations*, J. Comput. Chem. **28**, 1817 (2007)

4. F.-Q. Xie, **R. Maul**, S. Brendelberger, Ch. Obermair, E.B. Starikov, W. Wenzel, G. Schön, and Th. Schimmel, *Pre-selectable integer quantum conductance of electrochemically fabricated silver point contacts*, Appl. Phys. Lett. **93**, 043103 (2008)

5. F.-Q. Xie, **R. Maul**, A. Augenstein, Ch. Obermair, E.B. Starikov, W. Wenzel, G. Schön, and Th. Schimmel, *Independently switchable atomic transistors with predefined quantum conductance by reversible contact reconstruction*, Nano Lett. **8**, 4493 (2008)

6. Ch. Obermair, F.-Q. Xie, **R. Maul**, W. Wenzel, G. Schön, and Th. Schimmel, *Single-Atom Transistors: Switching an Electrical Current with Individual Atoms*, Springer-Verlag Berlin Heidelberg (2009)

7. S. Behrens, A. Heyman, **R. Maul**, S. Essig, S. Steigerwald, A. Quintilla, W. Wenzel, J. Bürck, O. Dgany and O. Shoseyov, *Constrained Synthesis and Organization of Catalytically Active Metal Nanoparticles by Self-Assembled Protein Templates*, Adv. Mater **21**, 3515 (2009) (*Cover paper*)

8. **R. Maul** and W. Wenzel, *Influence of structural disorder and large-scale geometric fluctuations on the coherent transport of metallic junctions and molecular wires*, Phys. Rev. B **80**, 045424 (2009)

9. F.-Q. Xie, **R. Maul**, Ch. Obermair, W. Wenzel, G. Schön, and Th. Schimmel, *Multilevel Atomic-Scale Transistors Based on Metallic Quantum Point Contacts*, Adv. Mater **22** in press (2010)

10. **R. Maul**, F.-Q. Xie, Ch. Obermair, I. Bâldea, H. Köppel, G. Schön, Th. Schimmel, and W. Wenzel, *Direct in-situ observation of single atom processes in reconstruction of metallic point contacts*, submitted to Phys. Rev. Lett. (2010)

11. I. Bâldea, **R. Maul**, W. Wenzel, and H. Köppel, *Applying the extended molecule approach to correlated electron transport: important insight from model calculations*, submitted to Phys. Chem. Chem. Phys. (2010)

12. C. Howell, **R. Maul**, C. Bartha, W. Wenzel, and P. Kölsch, *Interactions of hydrophobic and hydrophilic self-assembled monolayers with water as probed by sum-frequency-generation spectroscopy*, submitted to Chem. Phys. Lett.(2010)

Conference contributions and invited talks

1. R. Maul, F. Ortmann, M. Preuss, K. Hannewald, and F. Bechstedt, DFT Studies for Structure, Energetics, and Dynamics of Glycine, Alanine, and Cysteine, DPG Frühjarstagung, Regensburg 2007

2. R. Maul, F. Ortmann, M. Preuss, K. Hannewald, and F. Bechstedt, Structure, Energetics, and Dynamics of Glycine, Alanine, and Cysteine from *first principles*, ECME Conference, Metz 2007

3. R. Maul, and W. Wenzel, DEPOSIT – Multi-scale modeling package for OLED devices, NanoSolutions, Frankfurt 2007

4. R. Maul, J. Starikov, G. Schön, and W. Wenzel, Atomistic Structure and Transport Simulations of an Atomic Quantum Switch, RTN Meeting, Bremen 2008

5. R. Maul, G. Schön, W. Wenzel, Atomistic Structure and Transport Simulations of an Atomic Quantum Switch, Moriond Conference, La Thuille 2008

6. R. Maul, F.-Q. Xie, Ch. Obermair, W. Wenzel, G. Schön, and Th. Schimmel, Switchable Atomic Transistors with Predefined Quantum Conductance by Reversible Contact Reconstruction, PRIME Conference, Honolulu 2008

7. R. Maul, G. Schön, and W. Wenzel, Atomistic Structure and Transport Simulations of an Atomic Quantum Switch, ElecMol Conference, Grenoble 2008

8. R. Maul, G. Schön, and W. Wenzel, Transport in Metallic and Organic Nano-Wires, invited seminar talk, Institut ür Festkörpertheorie und -optik, Jena 2009

9. R. Maul and W. Wenzel, Molecular Electronics Simulations of Transport Through Single Molecules and Organic Films, Minotor Meeting, Mons 2009

10. R. Maul, G. Schön, and W. Wenzel, Structure and Transport Simulations in Atomic Transistors and Disordered Nano-Junctions, CFN summer school, Bad Herrenalb 2009

11. R. Maul and W. Wenzel, Modelling of electronic processes at interfaces in organic-based electronic devices, Minotor Meeting, Ludwigshafen 2009

12. R. Maul, G. Schön, and W. Wenzel, Multi-Scale Simulation of Conformation and Eletronic Transport in Nano-structures, invited seminar talk, Steinbruch Center for Computing, Karlsruhe 2010